Fundamental Aspects on the Formation, Structure and Functionalisation of oxo-functionalised Graphene and thereout derived Graphene

Inaugural-Dissertation

to obtain the academic degree

Doctor rerum naturalium (Dr. rer. nat.)

Submitted to the Department of Biology, Chemistry and Pharmacy

of Freie Universität Berlin

by

Christian Eberhard Halbig

born in Schweinfurt

10/2018

The here presented work was carried out between 09/2014 and 10/2018 at ZMP (*Zentralinstitut für Neue Materialien und Prozesstechnik*, 90762 Fürth, Germany) and *Freie Unversität Berlin* (14195 Berlin, Germany) under the supervision of Prof. Dr. Siegfried Eigler.

1.) Referee: Prof. Dr. Siegfried Eigler (FU Berlin)

2.) Referee: Prof. Dr. Andriy Mokhir (FAU Erlangen-Nürnberg)

Disputation at: 13. November 2018

„Erfahrung ist ein strenger Lehrmeister, denn er prüft bevor er lehrt.“

Unbekannt

Meiner Familie, Freunden und Kollegen,

die mir stets den richten Weg gewiesen haben.

Inhaltsverzeichnis

1. Zusammenfassung

Diese kumulative Dissertationsschrift behandelt Themen aus vier grundlegenden Bereichen: a) Darstellung und Eigenschaften von oxo-G; b) Steuerung der Partikelgröße; c) biologische Kompatibilität von oxo-G; d) kontrollierte Funktionalisierung von oxo-G und Graphen. Die hier präsentierte Forschungsarbeit wurde in Kooperation mit den Arbeitsgruppen von Prof. Dr. B. Meyer, Prof. Dr. W. Peukert, Prof. Dr. A. Mokhir, Prof. Dr. M. R. Heinrich und Prof. Dr. A. Hirsch von der Friedrich-Alexander-Universität Erlangen-Nürnberg durchgeführt. Diese Arbeit beinhaltet eine Synopsis der behandelten Themengebiete sowie die dazugehörigen Publikationen als Anhang in Kapitel 6 und 7. Im Sinne der Einfachheit werden hier die Bezeichnungen *oxo-funktionalisiertes Graphen* (oxo-G) und der historische Name *Graphenoxid* (GO) in dieser Arbeit synonym verwendet.

a. Darstellung und Eigenschaften von oxo-G

Bis zu diesem Zeitpunkt sind die zugrundlegenden Prozesse der Bildung von Graphit-Interkalationsverbindungen (GIV) und konsequenterweise die Herstellung von fast intaktem Graphen aus unterschiedlichen Graphiten nicht vollständig untersucht worden. Um dies im Detail zu untersuchen wandten wir ein durch uns etabliertes Verfahren zur milden Oxidation und Interkalation mittels Ammoniumpersulfat auf kristallinen und turbostratischen Graphit an (*Nat. Commun.* **2018,** Kap. 6.1a).[1] Die erhaltenen Materialien haben besondere Merkmale, die eine genaue Analyse jedes Reaktionsschrittes zulassen und letztendlich zu nasschemisch hergestelltem Graphen mit einem fast intakten Kohlenstoffgitter führen können. Durch *in-situ* Raman-Spektroskopie und *ab-initio* Molekulardynamik-Simulationen (*ai*MD) konnten wir einen großen Einfluss der Schichtfolge des verwendeten Graphits auf den ablaufenden Oxidations- und Interkalationsprozess ermitteln. Weiterhin konnte gezeigt werden, dass sowohl Schichtfolge als auch Oxidationszustand den Green-Kubo Reibungskoeffizienten von der interagierenden Schwefelsäure beeinfluss wird. Weitere Simulationen zur Stabilität von oxo-funktionellen Gruppen in Graphitsulfat unterstützen unsere Theorie eines Oxidationsmechanismus, der unabhängig von der Interkalation des Persulfats ist.

Weiterhin nutzen wir unter anderem die eben beschriebene Methode, um das in der Literatur der letzten Jahre häufig zur Erklärung von experimentellen Ergebnissen herangezogene *Zwei-Komponenten-Strukturmodell* nach Rourke *et al.*, welches in der Literatur oft als Modell zur Interpretation von Messergebnissen herangezogen wird, zu überprüfen.[2] Hier werden den sogenannten *Oxidative Debris* (ODs) einen großen Einfluss auf die optischen und elektronischen Eigenschaften von oxo-G zugeschrieben. Allerdings basiert dieses Modell auf unzureichenden Experimenten und deren Ergebnisse können leicht alternativ interpretiert werden.[3] In unseren Experimenten extrahierten wir OD nach der Methode von Rourke *et al*. beschriebenen Methode und setzen diese wieder mit unterschiedlichen oxo-G Derivaten zu artifiziellen Zwei-Komponenten-Systemen zusammen (*J. Am. Chem. Soc.* **2016,** Kap. 6.1b).[4] Ein essentieller fortschritt war hierfür die Synthese von Derivaten über unterschiedliche Oxidationsprotokolle unter kontrollierten Bedingungen, die letztendlich zu unterschiedlichen Mengen bzw. keinen OD führt. Die photophysikalischen Eigenschaften der einzelnen sowie zusammengeführten Komponenten wurden mit Hilfe von Fluoreszenz-Lebenszeitmessungen sowie absorptions- und

emissionsspektroskopischen Methoden untersucht. Die so erhaltenen Ergebnisse zeigten, dass die optischen Eigenschaften von oxo-G nicht von OD dominiert werden, sondern durch die Struktur des verwendeten oxo-Gs selbst bedingt sind und es sich bei oxo-G mehr um ein *Ein-Komponentensystem* handelt, bei dem OD kein essentieller Bestandteil von oxo-G ist und eine untergeordnete Rolle spielen.

b. Steuerung der Partikelgröße

Mit dem Ziel der reproduzierbaren Herstellung von oxo-G mit definierten Partikelgrößen und somit optimierten Eigenschaften für biologische und technische Anwendung wurde von uns der Einfluss von Ultraschall und Kugelmühle auf die Partikelgröße in oxo-G Dispersionen im Detail untersucht (*Carbon* **2016, 2017,** Kap. 6.2).[5] Durch einen optimierten Versuchsaufbau, welcher eine Fragmentierung bei niedrigen Temperaturen erlaubt (< 10 °C), konnte eine chemische Veränderung des Ausgangsmaterials während des Prozessierens durchgehend umgangen werden. Wegen des nun gewährleisteten konstanten hydrodynamischen Durchmessers war eine präzise Analyse der Partikelgrößen mittels Analytischer Ultrazentrifugation über die Sedimentationsgeschwindigkeiten nun möglich. Die ermittelten Bruchraten, induziert durch Ultraschall und Kugelmühle, skalieren linear mit der eingetragenen Energie und folgen dem Potenz-Gesetzt. Ein weiterer Vergleich der Bruchraten verschiedener gezielt hergestellter oxo-G Derivate zeigte, dass die Dichte und Art der funktionellen Gruppen großen Einfluss haben. Durch unsere so gewonnenen Erkenntnisse konnte der vormals von Gonçalves *et al.* vorgeschlagenen *confined hot-spot atomic reduction and fragmentation* als Überlagerung von Bruch und temperaturinduzierter Zersetzung von oxo-G identifiziert werden.

c. Biokompatibilität von oxo-G

Oxo-G kann durch seine ausgeprägte Fähigkeit der reversiblen Bindung von Molekülen an seine Oberfläche als molekulares Transportsystem in biologischen System agieren, wobei die medizinische Anwendung durch seine Zytotoxizität und Mutagenität limitiert ist. Aus diesem Grund untersuchten wir nach unserer Methode hergestelltes oxo-G sowie nachbehandelte Derivate auf ihre Toxizität Anhand ihrer Bildung von reaktiven Sauerstoffspezies in Zellen mittels Durchflusszytometrie in Kombination mit 2,7-Dichlorfluorescindiacetat (*Angew. Chem. Int. E.* **2016**, Kap. 6.3a).[6] Mit Hilfe von $^1O_2$-sensiblen Fluoreszenzsonden konnte das Vorhandensein von Endoperoxiden auf der Oberfläche von frisch hergestelltem oxo-G als ein Hauptgrund für die Zelltoxizität identifiziert werden. Diese neu gefundene funktionelle Gruppe ist instabil gebunden und kann durch Säure- sowie Basenbehandlung entfernt werden, wohingegen das Einleiten von elementaren Sauerstoff zu deren Regeneration führt.

In einer zweiten Studie wurden die ablaufenden Alterungsprozesse während der Lagerung bei unterschiedlichen Temperaturen sowie der Einfluss der chemischen Nachbehandlung von frisch synthetisierten oxo-G über einen Zeitraum von bis zu 4 Wochen genauer untersucht (*Chem. Eur. J.* **2016**, Kap. 6.3b).[7] Entscheidend war hierfür die Verwendung von oxo-G mit fast intaktem Kohlenstoff-Gitter und definierten Funktionalitäten, dessen synthesebedingte Eigenschaften durchgehend reproduzierbar waren. Durch die Verwendung von diversen Fluoreszenzsonden mit Oligonukleotid-Anker konnte gezeigt werden, dass in zeitlicher Abhängigkeit

Umlagerungen von funktionellen Gruppen auf oxo-G stattfinden und sich aus einem anfänglich homogen funktionalisiertem oxo-G ein Material mit ausgedehnten graphenartigen sowie hochfunktionalisierten Domänen bildet. Dieser Umlagerungsprozess ist unter anderem dafür verantwortlich, dass sich sowohl die Eigenschaften als Molekültransporter in Zellen im Laufe der Zeit ändern als auch die Toxizität durch den Verlust von instabil gebundenen Endoperoxiden verringert.

d. Kontrollierte Funktionalisierung von oxo-G und Graphen

Durch kontrollierte Oxidationsbedingungen und wässriger Aufarbeitung unterhalb von 10 °C können Organosulphate als funktionelle Gruppe von oxo-G erhalten bleiben. Diese funktionelle Gruppe kann durch Natriumazid in einer Festphasenreaktion substituiert werden. Das so erhaltene Produkt wurde sowohl thermisch als auch chemisch mit Natriumborhydrid und Salzsäure in unterschiedlichen Konzentrationen behandelt, um gezielt oxo-funktionelle Gruppen zu entfernen und reines Graphenazid zu erhalten (*Molecules* **2015**, Kap. 6.4a).[8] Wir fanden einerseits heraus, dass eine selektive Abspaltung von oxo-funktionellen Gruppen mittels Natriumborhydrid oder durch thermische Behandlung bei 140 °C nicht möglich war. Allerdings führte die Behandlung mit 0.5 bis 2.0 M Salzsäure zu einer partiellen Abspaltung von physisorbierten Wasser und oxo-funktionellen Gruppen, während ein Großteil der Azid-Gruppen erhalten blieb. Diese Untersuchungen bilden einen ersten Schritt hin zur Darstellung von Graphen mit ausschließlich Aziden als funktionelle Gruppe.

In zwei weiteren Studien untersuchten wir Möglichkeiten der Funktionalisierung von Graphen, welches wir unter anderem durch quantitative Reduktion von oxo-G mit Iodwasserstoff und Trifluoressigsäure erhalten haben. In den vergangenen Jahren wurde durch andere gezeigt, dass reduktive Funktionalisierungstechniken an Graphit und CVD Graphen zur Hexylierung des π-Systems führen kann. Allerdings ist durch die Wahl des gewählten Ausgangsmaterials die Ausbeute an funktionalisiertem, monolagigem Graphen stark limitiert. Deswegen verwendeten wir als alternatives Ausgangsmaterial suspendiertes, monolagiges Graphen aus oxo-G, da es eine definierte Struktur besitzt sowie einfach und in großen Mengen herzustellen ist. (*Chem. Eur. J.* **2018**, Kap. 6.4b).[9] In einer Vergleichsstudie mit unterschiedlichen funktionalisierten Graphen-Derivaten konnten wir zeigen, dass statistische Raman Spektroskopie nach der reduktiven Funktionalisierung von unserem nasschemisch hergestellten Graphen trotz seine geringen Defektdichte wegen des sehr geringen Funktionalisierungsgrades nicht sensitiv genug ist, um eine erfolgreiche Hexylierung zu bestätigen. Nichtsdestotrotz konnte durch eine thermogravimetrische Analyse mit zusätzlichem Gaschromatographen und Massenspektrometer eine erfolgreiche Funktionalisierung durch das Detektieren obligatorischer Massenfragmente festgestellt werden. Zusätzlich konnten wir zeigen, dass die Ausbeute an monolagigem, funktionalisiertem Material signifikant gesteigert wurde.

In der zweiten Studie untersuchten wir die Funktionalisierung von CVD-Graphen sowie verschiedenen nasschemisch hergestellten Graphen-Derivaten auf Oberflächen sowie in Dispersion durch verschieden substituierte Arylazocarbonsäure-*tert*-butylester (eingereicht in *Angw. Chem.* **09/2018**, Kap. 6.4c). Im Gegensatz zu unseren Erwartungen fanden wir heraus, dass das π-System der verschiedenen Materialien unterschiedlich stark funktionalisiert wurde. Durch das gezielte Eintragen von weiteren Gitterfehlstellen in das Kohlenstoffgerüst konnten wir ermitteln, dass diese die Reaktivität von Graphen gegenüber Arylazocarbonsäure-*tert*-butylestern erhöhen. Aufbauend auf unseren experimentellen Ergebnissen der statistischen Raman Analyse wurde ein Model für eine durch Defekte aktivierte Funktionalisierung von Graphen entwickelt.

2. Summary

This cumulative dissertation is divided in three main topics: a) Formation and properties of oxo-G; b) particle size control; c) bio-compatibility of oxo-G, d) controlled functionalisation of oxo-G and graphene. The research was conducted in collaboration with other workgroups, namely the group of Prof. Dr B. Meyer and Prof. Dr. W. Peukert, Prof. A. Mokhir, Prof. Dr. M. Heinrich and Prof. Dr. A. Hirsch, all from Friedrich-Alexander University of Erlangen-Nuremberg. This thesis includes more detailed results and experimental information in the form of attached publications in section 7 and 8. For the sake of simplicity, the terms *oxo-functionalised Graphene* (oxo-G) and *graphene oxide* (GO) will be uses as synonyms.

a. Formation and Properties of oxo-Graphene

So far, the fundamental processes occurring during the formation of graphite intercalation compounds (GIC) and consequently the formation of almost intact graphene out of different types of graphite had been not well investigated. To investigate this aspect in detail, we applied our unique method of mild and controlled oxidation and intercalation by ammonium persulphate into crystalline and turbostratic graphite (*Nat. Commun.* **2018**, Ch. 6.1a).[10] Hereby yielded products bear specific properties, which allow a precise analysis of each reaction step. Finally, wet chemically exfoliated graphene with the lowest density of lattice defects described in literature can be obtained. Using *in-situ* Raman spectroscopy and *ab-initio* molecular dynamics simulations (*ai*MD) we found an influence of the stacking order onto the efficiency of intercalation and oxidation of the used types of graphite. Furthermore, we revealed that oxidation and stacking order influences the Green-Kubo-friction coefficient of intercalating sulphuric acid molecules between the single layers of graphite. Additional simulations of the stability of covalently bound oxo-species in graphite sulphate support an oxidation mechanism independent from intercalation of the oxidant.

Moreover, we used the above mentioned method of controlled oxidation and intercalation to challenge the *two-component structural model* according to Rourke *et al.,* which was often used to explain experimental results using oxo-G. This structural model makes strongly bound *oxidative debris* (OD) responsible for oxo-G's optical and electronic properties, but the state of evidence for this model is ambiguous and bases on insufficient experiments and interpretation.[2-3] To check the reliability of this model we extracted OD following the protocol by Rourke *et al.* and created artificial two-component system with different types of oxo-G and characterised all precursors and products by fluorescence-lifetime measurements, absorption and emission spectroscopy (*J. Am. Chem. Soc.* **2016**, Ch. 6.1b).[4] Crucial for our experimental setup was the controlled preparation of several oxo-G derivatives *via* different protocols, which results in materials with and without OD. By the use of fluorescence lifetime measurements as well as absorption and emission spectroscopy we demonstrated, that the optical properties of any oxo-G derivative are not dominated by OD but origin from their internal structure. Furthermore, there is a strong evidence that oxo-G can rather be seen as a single component than a two-component material.

b. Particle Size Reduction

With focus on the highly reproducible preparation of oxo-G with defined particles sizes and thus optimised properties for biological and technical application we investigated the influence of ultrasound and ball milling onto the size distribution of oxo-G in detail (*Carbon* **2016, 2017**, Ch. 6.2).[5] We designed an optimised experimental setup, which allows us to process oxo-G at low temperatures (< 10 °C) and avoid any changes in the chemical composition of the initial material and hence to keep the hydrodynamic sheet thickness constant throughout. Consequently, highly precise analytical ultracentrifugation could be used to determine particles size distribution by the analysis of the sedimentation velocity. The comminution rate scales linear with the introduced energy and follows a power-law. A comparison of different oxo-G derivatives with specific properties revealed a significant influence of the quantity and quality of functional groups onto the comminution rate. Thus, the once published proposal of a *confined hot-spot atomic reduction and fragmentation mechanism* by Gonçalves *et al.* was identified as a superposition of fragmentation and temperature induced decomposition.

c. Biocompatibility of oxo-G

The ability of oxo-G to reversibly bind small molecules makes it suitable as a molecular carrier system, whereas its application is limited by its cytotoxicity and mutagenicity. For this reason, we synthesised several oxo-G derivatives and tested them for their toxicity through their generation of active oxygen species in cells using flow cytometry in combination with 2,7-dichlorofluoreceine diacetate (*Angew. Chem. Int. E.* **2016**, Ch. 6.3a).[6] With $^1O_2$-sensible fluorescence probes we have been able to identify endoperoxides bound to the lattice of oxo-G being mainly responsible for the cell toxicity of oxo-G. Furthermore, these endoperoxides can be removed by acid or base treatment as well las long-time storage (*aging*) but can also be restored by passing oxygen through the aqueous dispersion of oxo-G.

In a second study we investigated the process of aging of three different oxo-G samples stored for four weeks at different conditions as well as chemical post-treatment (*Chem. Eur. J.* **2016**, Ch. 6.3b).[7] It was crucial for our experiments to use oxo-G with an intact carbon lattice and defined composition of moieties with a high reproducibility. We used highly sensible fluorescence probes bearing an oligonucleotide based anchoring unit to investigate time-depending structural changes of oxo-G. Our experiments gave evidence that aging effects are responsible for rearrangement reactions of moieties to form highly functionalised and graphene like domains out of an initially homogenously functionalised oxo-G surface, whereas the absolute chemical composition remains untouched. Furthermore, this effect is suspected to be one reason for the loss of endoperoxides over time and changing properties as a molecular carrier system.

d. Controlled Functionalisation of oxo-G and Graphene

Organosulphates bound to oxo-G can be preserved as a functional motif by applying controlled oxidative conditions and aqueous workup below temperatures of 10 °C. These functional group can now be substituted by sodium azide in a solid state reaction to yield oxo-G-N_3. Subsequently, this product was thermally and chemically treated with sodium borohydride and hydrochloric acid in different concentrations with the aim to obtain pure pristine graphene azide (*Molecules* **2015**, Ch. 6.4a**)**.[8] However, a selective cleavage of oxo-functional groups by annealing (140 °C) or treatment with strong reducing agents was not possible, but treatment of oxo-G-N_3 with hydrochloric acid at a concentration of 0.5-2.0 M lead to partial removal of strongly bound water and some oxo-functional groups. This research should be seen as a first step towards the synthesis of graphene sheets functionalised with exclusively azide moieties.

In two further studies we investigated techniques to functionalize graphene obtained from oxo-G by quantitative reduction using hydroiodic and trifluoroacetic acid. Recently it was shown, that reductive chemistry on bulk graphite or CVD graphene can yield functionalised graphene with hexyl groups. However, the selection of the initially chosen source material limits the yield of functionalised single layer graphene sheets. Thus, we used suspended single layer graphene derived from oxo-G as it bears a defined structure and is available in large quantities (*Chem. Eur. J.* **2018**, Ch. 6.4b).[9] In a comparative study we were able to show that statistical Raman spectroscopy is insensitive and cannot visualize a successful functionalisation next to the initial vacancy defects in reduced oxo-G. Anyway, by the use of thermogravimetric analysis coupled to a gas chromatograph and mass spectrometer we could identify mandatory mass fragments proving a successful functionalisation. Further microscopic analysis of the products confirmed an improved yield of a functionalised single layer material.

In the second study we examined the functionalisation of CVD graphene and other wet-chemically prepared graphene derivatives by arylazocarboxylic *tert*-butyl esters on surfaces and in bulk (submitted to *Angew. Chem.* **09/2018**, Ch. 6.4c). Contrary to our expectation, the determined degree of functionalisation was different for all used graphene derivatives. By applying techniques to introduce additional lattice defects into our initially prepared under controlled conditions we could refer the observed variation in the reactivity of graphene towards arylazocarboxylic *tert*-butyl esters to lattice defects. Basing on our experimental data we proposed a novel model for defect site activated functionalisation of graphene.

3. Introduction

3.1. Prologue

In the last decades, chemistry offside from classical synthesis of molecules lead to many new materials suitable for medical, biological and technical applications. Nanoparticles, too large to be considered as a molecule, but too small to declare them as a piece of material, led to a more and more softened definition chemistry. Due to their size, these materials combine physical and chemical features of two different worlds: The world, where classical mechanics cease, and quantum mechanical effects take effect. Consequently, a new field of offside of traditional chemistry was entered and crosslinks classical fields in chemistry, biology, physics, surface and material related sciences.[7, 11] In 2010, the Nobel Prize in Physics was given to Andre Geim and Konstantin Novoselov for their fundamental research on two-dimensional, single-layer graphene sheets exhibiting its outstanding physical properties, which was first published in 2004.[12] Other layered materials like layered double hydroxides,[13] molybdenum disulphide,[14] black phosphorus,[15] arsenene, antimonene, bismutene,[16] and the so far not mentioned carbon allotropes, namely carbon nanotubes,[17] fullerenes[18] and their manifold derivatives[19] offer also interesting physical and chemical properties. In subsequent years, there was a boom on research focusing on tuning the physical and chemical properties of graphene and its derivatives as this material is stable under ambient conditions and available in large quantities. Thus, there is a high interest in their biological and technical application. The versatility of this material can be realised by the fact that it can be used to print flexible and semi-transparent circuits, as an efficient hole-transporting material in perovskite base solar cells, a molecular drug carrier system or even to desalinate water, just to name a few.[11d, 11e, 20]However beautiful and interesting the advances in this field of science may be, nanomaterials are still a topic of current ethical discourse since the disadvantages affecting humanity and nature have not yet been adequately investigated.[21]

3.2. Properties of Carbon

Three stable isotopes of carbon can be found in nature: ${}^{12}_{6}C$ (98.9%), ${}^{13}_{6}C$ (1.1%) and small traces of ${}^{14}_{6}C$ as the only natural radioactive isotope.[22] Other isotopes cannot be found in nature but artificially synthesised in laboratories (**table 1**).[23] ${}^{13}_{6}C$ is the only natural isotope with an odd number of nuclei and thus a magnetic and angular moment, which makes it suitable for nuclear magnetic resonance spectroscopy (carbon-13 NMR).[24] ${}^{14}_{6}C$ is radioactive with a half-life time of 5730 years and is used in the carbon-14 dating method to estimate the age of former organic materials. It mainly arises naturally in the upper layers of the troposphere and stratosphere out of ${}^{14}_{7}N$ by the absorption of thermal neutron and subsequent decay following the formula ${}^{14}_{7}N(n,p){}^{14}_{6}C$. Thereout emerging ${}^{14}_{6}C$ decays spontaneous to ${}^{14}_{7}N$ by the emission of an electron (${}^{0}_{-1}e$). Since the uptake of ${}^{14}_{6}C$ in living lifeforms is in a flow equilibrium, the ${}^{14}_{6}C/{}^{12}_{6}C$ ratio changes after death and the age can be determined (radio carbon method).[24]

The electronic configuration of $1s^2 2s^2 2p^2$ is given by the presence of 6 protons in the atomic nucleus.[22] With this configuration one carbon atom can theoretically take up or give up 4 electrons to obtain noble gas configuration. The concept of hybridisation was published by Linus Pauling in 1931 and helped to understand the formation of

the different binding motifs carbon can undergo by the combination of one *s*- with up to three *p*-orbitals with their initial different energies.[22] The obtained sp^3, sp^2+p , $sp+2p$ orbitals can not only form four equal σ-bonds (*e. g.* CH_4), but also double (*e.g.* $H_2C=CH_2$) or two triple bonds (*e.g.* HC≡CH) with other atoms by formation of additional π-bonds out of remaining unhybridised *p*-orbitals. The corresponding ideal binding angles are 109.5° (sp^3, tetrahedral), 120° (sp^2, trigonal-planar) and 180° (*sp,* linear).[22a, 24] As the smallest representative of group 14 elements, it is obvious that carbon has the highest electronegativity within his homologues with a value of 2.6 in the Pauling scale.[24]

Isotope	Isotope ratio	Exact mass	Half life	Radio activity	Decay Product
^{10}C	Synthetic	10.0168532	19.30 s	β^+	^{10}B
^{11}C	Synthetic	11.0114336	20.36 min	β^+	^{11}B
^{12}C	98.9	12.000000		stable	
^{13}C	1.1	13.003354		stable	
^{14}C	$< 10^{-9}$ %	14.003242	5730 a	β^-	^{14}N
^{15}C	Synthetic	15.0105993	2.449 s	β^-	^{15}N

Table 1 Summary of the physical properties of selected carbon isotopes. The values were taken from NUBASE published by the International Atomic Energy Agency (IAEA).[23]

3.3. Carbon Allotropes

In nature, high molecular carbon can be found in different forms and are known to the humans since ancient times. The most famous of those allotropes may be **diamond** (from old gr.: *ἀδάμας = adámas*, lat.: diamas = untamed). It consists out of sp^3 hybridised carbon atoms in a tetrahedral crystal structure.[22] The high average binding energy of four C-C bonds *á* 345 kJ/mol makes it the hardest known material next to silicon carbide and boron nitride with their diamond like tetrahedral structure.[22a, 24-25] Although C-H, C-F and C-O bonds are significantly stronger[1], hydrogen and halogen bonds terminate elongated structures as they are monovalent.[22a] Furthermore, a diamond offers the highest known thermal conductivity (type-IIa; up to 10,000 W/m*K at T=77 K) with one of the lowest thermal extension coefficients of 1.1×10^{-6}/K (synthetic diamond, type-Ib).[22b, 26] It begins to decompose in the presence of oxygen at temperatures higher than 700 °C and begins to graphitize at 1700 °C under inter gas conditions.[27] Impurities in the diamond structure provide colour to the regularly colourless and highly translucent material from yellow (nitrogen), blue (boron), violet to green or black (polycrystalline diamond).[22b] These aspects make this material highly suitable for optical devices or highly sturdy tools.

Graphite (from old geek: *γράφειν* = graphein) is - in stark contrast to diamond - a very soft mineral with a laminar crystal structure and a hardness of 0.5-1.0 on the Mohs scale **(figure 1A-C**).[28] In general, this material built up by many stacked and one atom thick **graphene** layers where every sp^2 hybridised carbon atom is connected in a hexagonal lattice structure to each other with a bond length of 142.1 pm and the angle between each bond is 120°.[29] Each graphene layer in a graphite crystal is bound to the adjacent layer by London disperse forces and π-π-interaction in an approximate distance of 335 pm.[30] The hexagonal unit cell in AB-stacked graphite (2H) with

[1] Binding energies: C-O bond: 358 kJ/mol; C-H bond: 416 kJ/mol; C-F bond:489 kJ/mol.

α = 2.46 Å and c = 6.71 Å contains 4 carbon atoms (**figure 1E**), whereas 6 atoms are needed to describe the rhombohedral unit cell with α = 2.46 Å in ABC-stacked graphite (3R, **figure 1F**) or 2 atoms to describe single layered graphene respectively (**figure 1D**).[22b, 31] In natural graphite sources, rhombohedral and hexagonal phases are present in mixed ratios.[31c] AA-stacked graphite does not occur naturally, but can be prepared by *e.g.* intercalation of graphite with lithium or grown on diamond.[32] In contrast, turbostratic graphite has no stacking order. Highly mobile delocalised π-electrons of eachgraphene layer cause the black to metallic colour of graphite and an in-plane conductivity of about 2.6×10^4/Ωcm, however a 10^4 times smaller conductivity orthogonal to the layered structure is found.[22] The measured thermal conductivity of bulk graphite is about 2,000 W/m*K and thus approximately 5 times higher than pristine copper, whereas a single and intact layer of graphene can reach an outstanding high thermal conductivity up to 5,000 W/m*K.[26a, 33] Anyway, impurity atoms, vacancies or other structural defects such as five and seven membered ring defects in the hexagonal graphene lattice can influence the described electric, thermal and mechanical properties.[33c, 33d]

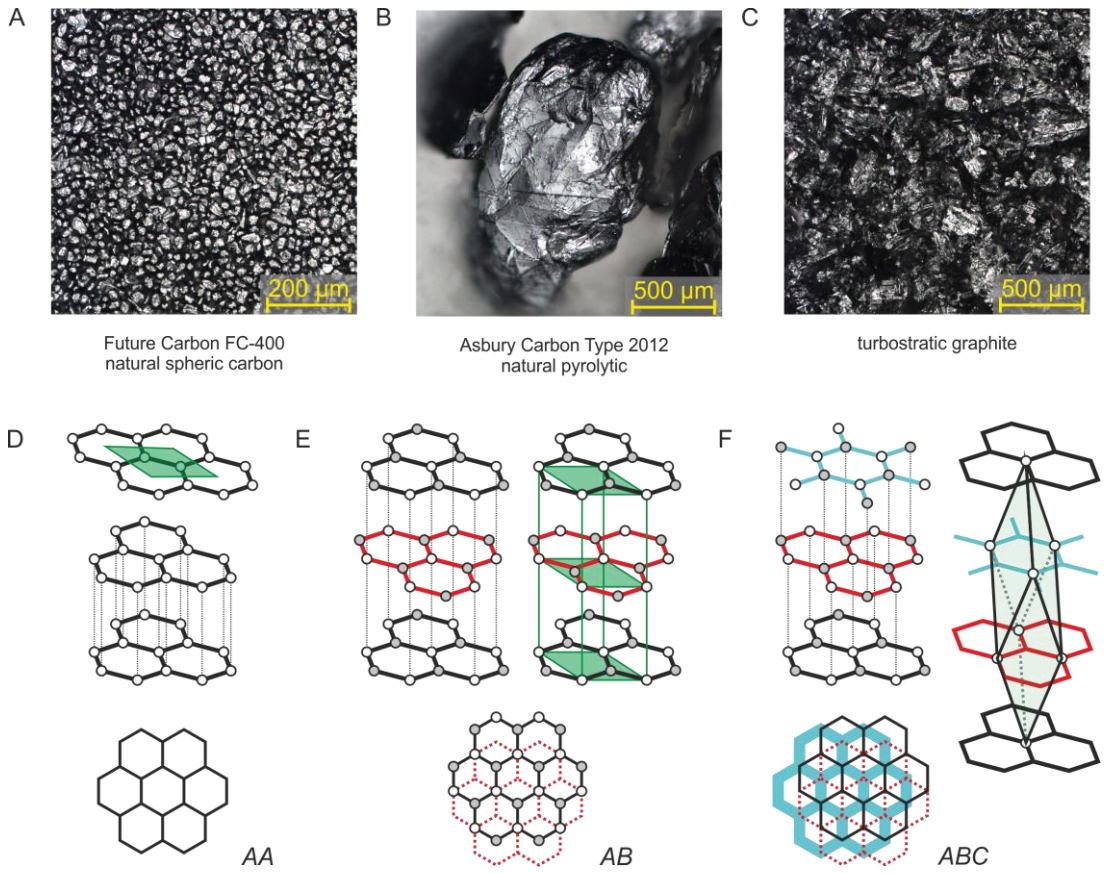

Figure 1 A) Natural spherical graphite; B) natural pyrolytic graphite and C) turbostratic graphite. D-F) Two and three-dimensional schematic illustration of different stacking orders in graphite. The unit cell is highlighted in green. D) AA stacking; E) AB stacking with its hexagonal unit cell. C) ABC stacking with a rhombohedral unit cell.

Graphite can be classified in various subtypes: natural, synthetic, intercalated, expanded, amorphous and turbostratic graphite. These differ in their morphology, grain size, density, purity, surface area, pH in water, density of defects (θ_D) and according to the origin of graphite.[22b, 31c] Sri Lankan graphite and Ceylon graphite are natural pyrolytic graphite types and have occasionally the highest degree of crystalline order and a purity of up to 99.5%.[31c] Expanded graphite was treated with acid in the presence of a catalyst and further rapidly thermally treated to partially separate each graphene layer by the resulting gas pressure of the intercalating agent.[31c] Synthetic graphite can be obtained by different high-temperature processes where either methane and hydrogen react on metal surfaces (CVD process) or organic bulk material, calcinated petroleum coke or coal tar pitch is mixed, molten and graphitised under high pressure and temperatures between 2,500 °C and 3,000 °C.[22b, 31c] Diamond can be transformed to graphite at temperatures higher than 1,700 °C in the absence of oxygen.[27a] If graphite becomes irradiated by neutrons, as it may happen for example in nuclear power plants, carbon atoms may become displaced to already existing vacancies or come to rest in non-ideal lattice positions outside of symmetrical lines of the lattice (Frenkel defect).[34] This way stored energy in the crystal structure is called Wigner energy and was one reason to cause the Windscale fire in 1957, a nuclear accident in Great Britain.[35]

One isolated and carbon layer of graphite is called a **graphene** sheet. A monolayer is almost completely transparent in the visible regime (97.7 %).[36] The long-range order of graphene sheets can be disturbed by missing atoms (*vacancy defects, D_V*), exchange of carbon atoms by other elements, adatoms and non-hexagonal ring structures like five and seven-membered or *i.a.* Stone-Thrower-Wales defects, and edges of individual layers at grain boundaries (**figure 2**).[31c, 33d, 37] These can also artificially be generated by electron beam irradiation of exfoliated graphene.[38] The edges are terminated in an armchair (AC), zigzag (ZZ) or reconstructed zigzag (recZZ) profile (**figure 2A**).[39] Koskinen *et al.* calculated the edge energy of AC, ZZ and recZZ to be 2.09, 3.22, and 2.36 eV/atom. The rearrangement from ZZ to recZZ stabilizes the system by about 0.84 eV/atom, however, the formation of a five and seven membered ring out of two hexagons by the rotation of a double bond at edges

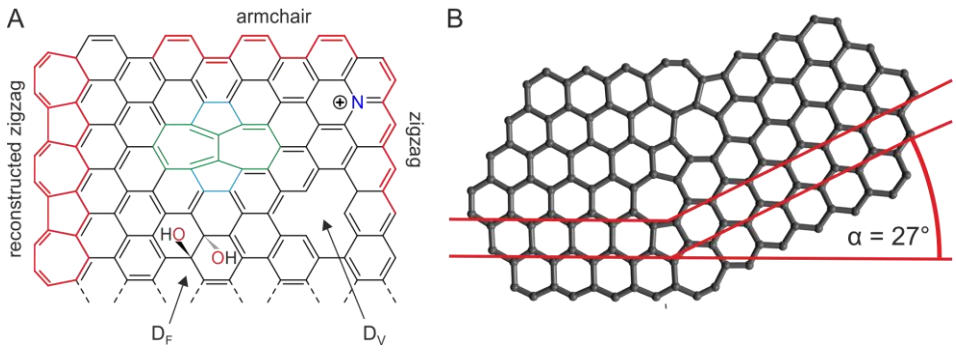

Figure 2 A) Graphene lattice illustrating different types of defects in and on the graphene lattice: Vacancy defect (D_V, lower-right side); functional defects or sp^3 defects (D_F, lower left side); heteroatom (upper right side); Stone-Thrower-Wales defect (upper left side). Zigzag and armchair and reconstructed zigzag conformation of the edges are highlighted in red. B) Grain boundary as it may occur in larger films of graphene produced by CVD process. Figure 2B was reproduced from the literature.[37]

need to overcome an energy barrier of about ~ 1.1 eV. For comparison, the energy barrier is increased to about ~ 10 eV inside a bulk graphene layer to form a Stone-Thrower-Wales defect. The ratio of AC to ZZ to recZZ is temperature depended as it was found by TEM experiments with suspended graphene between 25°C and 800 °C. At room temperature large holes in graphene generated by electron beam irradiation under ultra-high vacuum conditions contain AC (~ 50 %), ZZ (~ 40 %] and minor amounts of rec. ZZ (~ 10 %) configuration.[39b]

Carbon nanotubes (CNT) can be understood as tubular graphene derivatives.[17, 22b] Various methods have been developed to synthesize CNTs. CNTs can be prepared by manifold techniques like arc discharge, electrolysis, pyrolysis, chemical vapour deposition (CVD process), laser ablation, flame synthesis, high pressure carbon monoxide process (HiPco).[17, 40] Depending on the method, CNTs are available as single-wall (SW-CNTs) or multi-walled nanotubes (MW-CNTs) in a single or mixture of chiralities and various diameters, all influencing their physical end chemical properties.[17, 41] Depending on the route of synthesis, CNTs often contain metal impurities as they are often used as catalysts.[42] Like graphene, CNTs are exclusively built from sp^2 hybridised carbon atoms in a hexagon structure and have hence aromatic character. Due to the fact their geometry is bending the favoured trigonal-planar structure to a more tetrahedral structure, the chemical reactivity is increased in comparison to planar graphene. Moreover, it is reported that the treatment of CNTs by strong oxidants leads to unzipping of CNTs and thus, **graphene nanoribbons** are obtained.[43] The thermal conductivity of 1,500-7000 W/m*K is comparable to diamond and graphene.[26a]

4. The Route to Graphene

Single graphene layers can be obtained by different mechanical or chemical separation techniques out of graphite (top-down) or *via* chemical vapour deposition out of small organic molecules (bottom-up).[44] The most famous method to produce graphene is the mechanical exfoliation of graphite by the use of adhesive tape as it was introduced by the Noble price winners Geim and Novoselov in 2004.[45] The advantage of this method is the ease of the method and single sheets of practically defect-free graphene can be obtained. However, the yield of single layer graphene obtained by this way is limited to few flakes on surfaces. More efficient routes to obtain graphene on substrate are vacuum pyrolysis of SiC(0001) and chemical vapour deposition with H_2/CH_4 on transition metals like Ni, Co, Ir, Ru, Re, Pd, Pt and Cu at temperatures higher than 1000 °C, which leads to the controlled formation of large single and few-layered graphene sheets.[44a, 46] Best results for the growth of graphene with a low amount of lattice mismatches by CVD process was obtained using Co(0001), Cu(111), Ni(111) and Ge(110) substrates.[44a] A special advantage of using Ge(110) substrate is that the synthesised graphene layer can be dry-transferred due to the weak interaction between the graphene and underlying hydrogen-terminated germanium surface in contrast to the others metal substrates, which have to be removed by etching in liquid media first before transfer to other substrates.[47] Larger quantities of single and few layer graphene can be obtained by simple solvent driven exfoliation methods using external stress like *e.g.* ultrasound[44b, 48], ball milling[49] or jet cavitation.[50] Anyway, strong London dispersion forces (van-der-Waals forces) between each layer limit the efficiency of exfoliation by those methods. Wet chemical exfoliation of graphite using strongly oxidizing or reducing agents overcomes these limits of yield due to the functionalisation of the π-system by polar

moieties, as outlined more in detail below.[51] In the following sections, the wet chemical route to graphene *via* intercalation, functionalisation, exfoliation and reduction will be outlined in detail.

4.1. Graphite Intercalation Compounds (GICs)

Graphite crystals can be intercalated by manifold agents like Li, K, Cs, Br_2, Cl_2, $FeCl_3$, and SO_3 to form several types of stage-1 GICs, just to name a few.[22b, 52] Interestingly, Na is the only alkali metal that cannot be well intercalated at moderate conditions as the formation energy for NaC_6 and NaC_8 is positive in contrast to the other homologues.[53] The mechanism behind reductive graphite intercalation with alkali metals (**donor type**) is a single electron transfer from the reducing agent to the antibonding π* molecule orbital and subsequent cation intercalation to neutralize charges.[54] Thus, the interlayer distance between the graphene layers increases from 335 pm to 540 pm (K), 561 pm (Rb) or 575 pm (Cs).[22b] In stage-1 KC_8, for example, one potassium cation is centred in the middle of every fourth hexagon of a graphene layer. As two cations never occupy the same hexagon of a layer twice, the stacking order can be described as AαAβAγAδ. Initial AB stacking order is maintained for stages n>2 between intercalate layers.[52b]

Strongly oxidizing agents like $(NH)_4S_2O_8$, $NaNO_3$ or $KMnO_4$ in concentrated sulphuric acid or mixtures of it with other acids can deprive electrons from each graphene layer in a graphite crystal and force concurrent H_2SO_4/HSO_4^- intercalation to neutralize thus introduced positive charges (**acceptor type**).[1, 55] In this way, blue crystals with the formula of $C_{24}^+ HSO_4^- \times 2\ H_2SO_4$ can be obtained with an interlayer distance of 798 pm (**figure 3A, B**), as analysed in detail by Rüdorff and Hofmann decades before.[1, 52b, 56] Many other routes to oxidize graphite were developed since graphite oxide or graphitic acid was first discovered, but most likely the mixture of $KMnO_4/NaNO_3/H_2SO_4$ (Hummers' and Offeman's method) is the most often used mixture to oxidize and intercalate graphite as it can penetrate almost every layer of a graphite stack. An overview of the most important oxidation protocols can be found in **table 2 (page 22).**

The number of (doped) graphene sheets in-between two layers of the intercalant gives the staging index number *m* (**figure 3C**). In a completely intercalated graphite crystal where each doped graphene layer is separated by a layer of intercalant, the staging index number $m = 1$. In the case of an incomplete intercalation, not every position between two graphene layers is occupied by intercalant and therefore $m > 1$ (**figure 3C**).[57] The effectiveness of intercalation is not only influenced by the redox potential and size of the used oxidation or reduction agent and the used co-intercalating agent, but also from the chosen type of graphite as they differ in their stacking order and crystallite size. [1, 53, 58] Hooley could demonstrate, that smaller sized graphite has an increased uptake of the intercalate.[58c] Furthermore, Moissan observed in 1895 that the use of concentrated acids improves the transformation of graphite to graphite oxide which may be reasoned in an improved intercalation and oxidation of the graphite crystals.[59] Moriwake *et al.* investigated the formation of alkali metal-GICs by density functional theory calculations and could refer a lower formation energy of intercalating alkali metals to larger ion radii. He found out that lithium is extraordinary from this trend as Li-C bonds contain a non-negligible covalent component facilitating its intercalation.[53] Recently we investigated the formation of graphite sulphate and experimentally

conduced a mechanism of GIC formation, in which the oxidation agent oxidizes the graphite at edges without accessing the interlayer space (**figure 3D**).

After proper GICs were formed, these highly reactive compounds can be directly exfoliated to mono and few layered graphenide sheets as it was shown for alkali metal GICs or directly used for further chemical functionalisation.[51b] The addition of water to acceptor type GICs leads to graphite with oxo-functional groups,[51c, 55a, 61] whereas the addition of alkyl iodides, aryl iodonium and aryl diazonium salts to donor type GICs leads to graphite with alkyl or aryl moieties attached to the individual graphene layers.[62] The introduction of hydrogen moieties to obtain graphane like materials can be achieved by the addition of a proton source, for example acids, to a donor type GIC.[63]

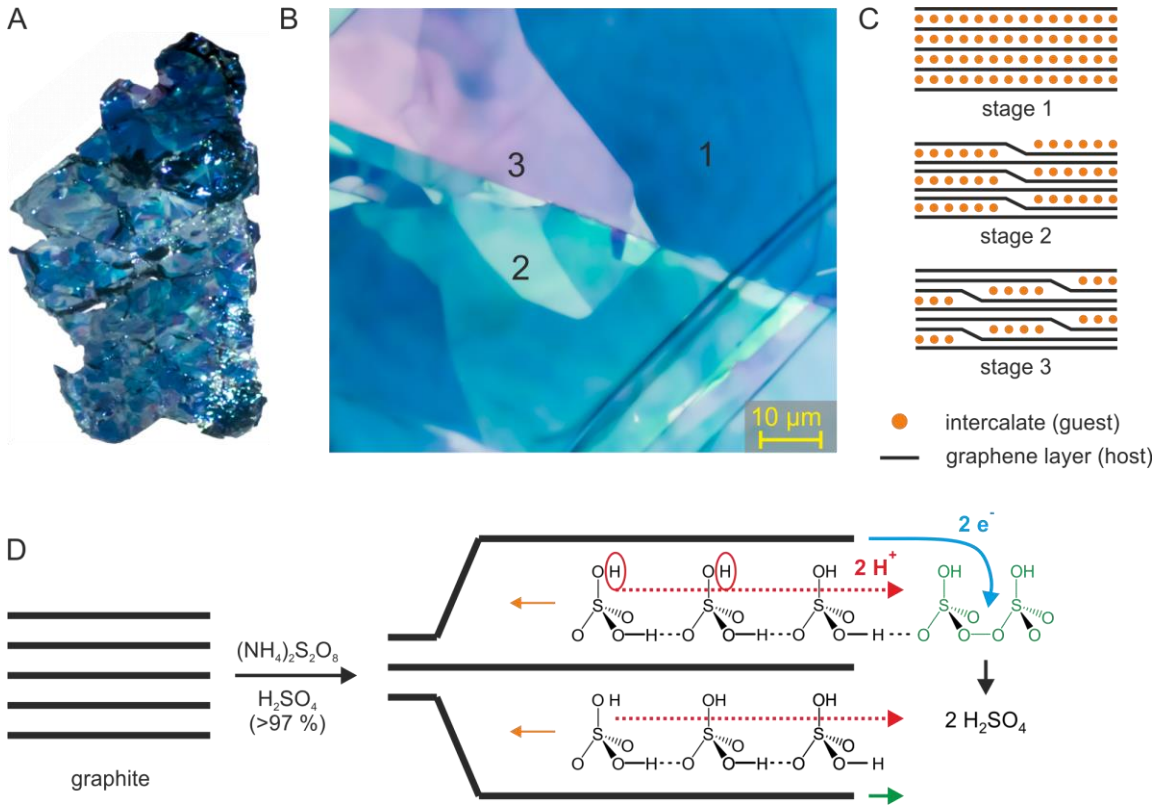

Figure 3 A) Intercalated natural graphite flake oxidised with $(NH_4)_2S_2O_8$ in sulphuric acid (98%). B) Light micrograph of the surface of the left shown flake. Dark-blue areas (1) can be related to stage-1 intercalation, whereas it is partially hindered in bright blue, greenish (2) to purple areas (3). C) Daumas-Harold model of different stages of intercalation.[60] D) Schematic illustration of the oxidation mechanism by persulphate (green). The interlayer distance increases due to positive charges in each graphene layer by oxidation (blue arrow). Resulted charges are neutralised by intercalation of sulphuric acid (orange arrow) and accompanied generation to form hydrogen sulphate as counter ions (red arrow). Figure 2A and B were reproduced from the literature.[1]

4.2. Graphite Oxide (GrO)

Traditional and established methods like Brodie's[64], Staudemaier's[59a] or Hummers' and Offemann's[51a] (**table 2**) method describe the whole process of the formation of a acceptor type GIC with the subsequent attachment of oxo-functional groups on top and bottom of a graphene layer in a graphite crystal to obtain graphite oxide (GrO), which consists out of stacked and oxygenated graphene layers. All of the here mentioned protocols have in common that graphite is stirred with a large excess of an oxidizing agent in pure sulphuric acid or mixtures of it with nitric acid (Brodie: HNO_3) to obtain an acceptor type GIC, which can be further poured into water to yield graphite oxide (**figure 4**).[64] Other oxidants like $K_2Cr_2O_7$/$K_2Cr_2O_7$ (Brodie[64] and Charpy[65]), $KMnO_4$ (Staudenmaier[59a], [2], Charpy[65], Luzi,[66] Hummers and Offeman)[51a] and $K_2S_2O_8$/$(NH_4)_2S_2O_8$ (Eigler, Dimiev) have been tested in the last decade to substitute the dangerous $KClO_3$ (Brodie[64], Staudenmaier[59a]).[67] Certainly, the most popular oxidation method up to date is the Hummers' and Offeman's method in many different variations as it converts almost all initial graphite to the corresponding GIC.[55b, 58a, 58b]

After adding water to a so formed GIC, positive charges in each graphene layer become neutralised and defects in the planar sp^3 carbon lattice are introduced. These defects can be both vacancy defects (D_V) and holes due to degradation of the graphene lattice structure by CO/CO_2 formation due to harsh oxidative conditions or functional defects (D_F) by the introduction of mainly hydroxyl, epoxide, sulphuric acid ester moieties and

Method	**Brodie**[64] *(1859)*	**Staudenmaier**[59a] *(1898)*	**Hummers & Offeman**[51a] *(1957)*	**Tour**[58b] *(2010)*	**Eigler**[51c] *(2013)*
oxidation conditions	HNO_3 3-5 eq. $KClO_3$ 3-4 days Up to 60 °C	2:1 H_2SO_4/HNO_3 30 eq. $KClO_3$ 0.3 eq. $KMnO_4$ 1 hour 20 °C	H_2SO_4 0.5 eq. $NaNO_3$ 2.5-3 eq. $KMnO_4$ 1.0 hour 25-45 °C	9:1 H_2SO_4/H_3PO_4 6.0 eq. $KMnO_4$ 12 hours 50° C	H_2SO_4 2.0-3.0 eq. $KMnO_4$ 16 hours < 10°C
water addition	Poured into water/ice	Poured into water/ice	Poured into water/ice	Poured into water/ice	Slow titration with diluted H_2SO_4 and water; < 10°C
further notes	Initial graphite was purified by boiling with Acid and KOH. Freeze-dried product will be re-oxidised for 4-6 times.	Expanded Graphite Washing with dil. HNO_3, Alcohol and Ether	Temperature may be partially up to 70-90 °C	Final product was washed with water, HCl and Ethanol. Coagulation performed with Ether.	Temperatures higher than 10 °C were avoided throughout the reaction.

Table 2 Overview of selected methods to prepare graphite oxide thereout graphene oxide.

[2] Staudenmaier originally used aqueous $KMnO_4$ solution to check the oxidation state of graphite. In recent literature Staudenmaier's method is often cited and performed without potassium permanganate.

endoperoxides in minor traces and on top and bottom of each stacked graphene layer. Additionally, carboxyl and carbonyl groups can only be found at edges or holes inside the graphene lattice structure as they require C-C bond breakage to be formed.[6, 51d, 61a, 68] Hence the traditional trivial name *graphite oxide* or *graphene oxide* is misleading as it suggests the existence of exclusive epoxide groups[3] as it was assumed earlier by Landau and Peierls.[69] Recently, Chen *et al.* demonstrated an influence of the concentration of water in the reaction mixture, which lead to different graphene oxides with varying ratios of hydroxyl and epoxide groups.[70] Furthermore, permanent vacancy defects are formed by over-oxidation and exposure to elevated temperatures during GrO formation.[51d, 71] Both lead to disproportionation of the hexagonal carbon framework by the formation vacancy defects and CO/CO_2.

4.3. Graphene Oxide (GO) / oxo-Functionalised Graphene (oxo-G)

With neutralisation of GrO after either filtration or centrifugation, the stacked and oxidised material readily delaminates in water to single layered oxo-functionalised graphene flakes (oxo-G) with or without the aid of external stress like ultrasound or ball milling (**figure 4**).[51d, 55a] A faster route than the both above mentioned ones, which are time consuming techniques, was shown by Feicht *et al.*, who used a simple two-phase extraction method with 1-dodecylamine as a phase transfer agent for oxo-G to extract this polar compound directly to a hydrophobic diethyl ether phase without further purification.[72] A typical single flake of oxo-G consists out of a basal hexagonal lattice structure with a diameter up to 50 µm or even higher, and is decorated with various oxo-

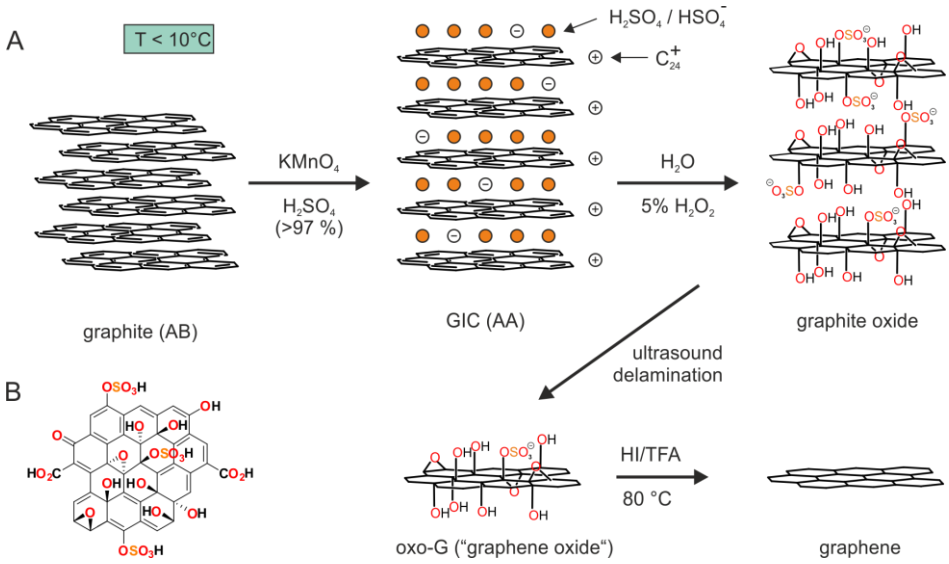

Figure 4 A) Illustration of the formation of graphite oxide (GrO) and thereout derived single layer oxo-G ("graphene oxide") by ultrasound treatment. First, graphite becomes oxidised and intercalated by potassium permanganate, sulphuric acid and hydrogen sulphate. Thereafter, the obtained GIC becomes functionalised by water. Neutralisation of the reaction mixture and exfoliation leads to single layer oxo-G. B) Structure of oxo-G basing on the model of Lerf and Klinowski. For the sake of clarity, vacancy defects are not illustrated.

[3] *Cf.* ethylene oxide

functional groups in different ratios depending on the chosen synthesis protocol. According to the most up-to-date Lerf-Klinowski model there are hydroxyl and epoxide groups bound to the upper and lower side of the carbon framework as well as in-plane hydroxyl, carbonyl and carboxyl groups at the edges or vacancy defects (**figure 4B**).[19c, 51d, 61a, 73] Later research revealed the existence of metastable sulphuric acid esters and instable endoperoxides in minor traces.[6-7, 68a] The latter ones are found to be responsible for the cell toxicity of oxo-G and can be removed by either base treatment or long-time storage.[6] The typical density of functional defects (θ_{FD}) can range between 44% to 71% for classical protocols using strong oxidation agents according to tradition methods.[73] Furthermore, there was evidence by experiments and theoretical calculations that functional groups on freshly prepared oxo-G are not localised on a specific carbon atom, but can rearrange on the carbon lattice during long-time storage or catalysed by protons. Thus, homogeneously distributed moieties on as-prepared oxo-G tend to form larger highly functionalised sp^2 domains and aromatic domains over time and acid treatment to increase its chemical and kinetic stability.[7, 74] The ordered hexagonal lattice structure of a single flake may be further ruptured by non-hexagonal ring motifs similar to Stone-Thrower-Wales defects or heteroatoms and is terminated at the edges in a zig-zag, reconstructed zigzag or armchair profile (**figure 2, 6**).[39a, 71b, 75] The presence of so-called oxidative debris (OD) as an additional component of oxo-G is a topic of current discussion. These OD are smallest and highly oxygenated fragments of over-oxidised graphene sheets formed during oxo-G preparation according to Hummers and Offeman. They are claimed to strongly bind to the surface of oxo-G and can be removed during workup with basic conditions. However, there is no clear evidence, that they are a compulsory component.[2-4]

In the view of its chemical composition and structure freshly prepared oxo-G dispersions are sensitive towards light, elevated temperatures, reducing agents and basic environment.[7, 44d, 71b, 76] Dimiev *et al.* investigated the influence of alkaline conditions on oxo-G in detail and introduced the dynamic structure model of oxo-G elucidating vacancy defect formation **(figure 5B**).[77] It was demonstrated that oxo-G flakes can disintegrate to smaller fragments after base-treament.[3] Light and heat can also facilitate decomposition of oxo-G to a more defective material by the loss of carbon in the form of CO/CO_2 due to disproportionation reactions occurring in the functionalised carbon lattice.[7, 76b, 76c] Recently, it was demonstrated that oxo-G can be biodegraded by several types of peroxidases. Up to now, best results of degradation was observed for individualised oxo-G sheets in suspension using human myeloperoxidases, naturally occurring in neutrophils (a class of white blood cells), in the presence of hydrogen peroxide.[78] The addition of multivalent cations can lead to a fast aggregation.[79]

Figure 5A shows some basic reactions of oxo-G nanoparticles with other agents. Sulphate groups can be substituted and epoxides can be opened by azide anions leading to oxo-G with covalently bound N_3-groups in a solid-state reaction or hydrolysed by diluted basic or acidic solutions.[8, 80] Those sulphate moieties can be restored up to a certain threshold by exposure to sulphuric acid at low temperatures (**figure 8**). The exposition to concentrated hydrogen chloride or other reducing agents lead to a loss of on-plane oxo-functional groups and azide moieties with different efficiencies.[8, 81] Furthermore, alkyl amines can be used for non-covalent functionalisation to tune graphene's properties *via* electrostatic interaction of the cationic amine and negatively charged organosulphates.[11d] Up to now, the selective on-plane functionalisation or in-plane functionalisation at extensive vacancy defects or edges is the goal of current research.[82]

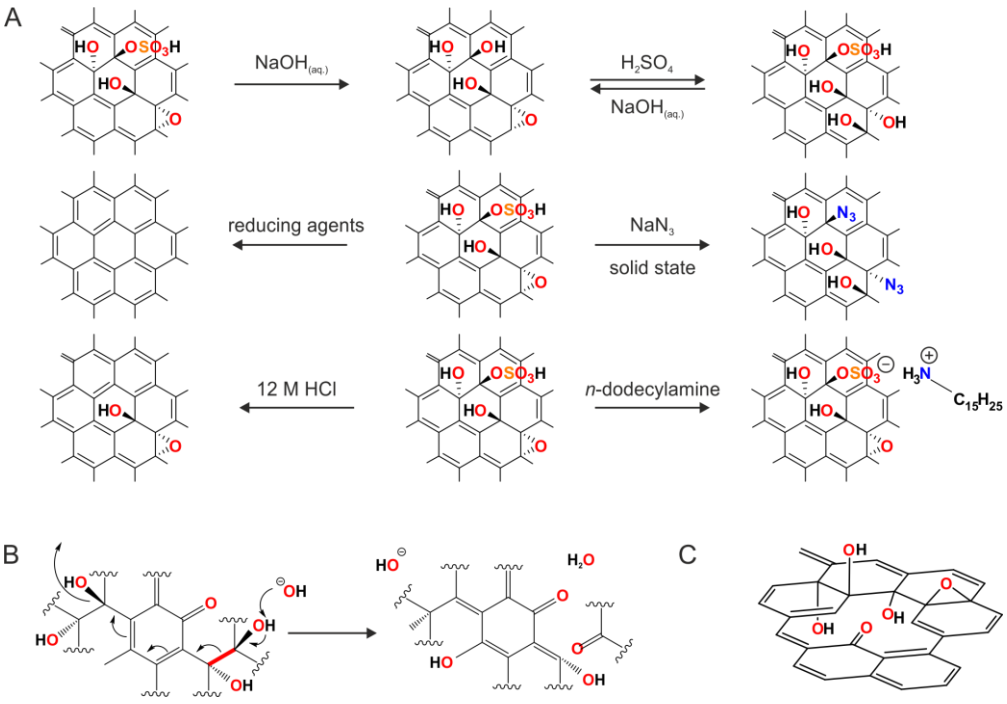

Figure 5 A) Fundamental reactions on oxo-functionalised graphene. Organosulphates can be reversibly cleaved by treatment with aqueous NaOH or sulphuric acid respectively. Reducing agents lead to graphene with varying efficiencies. Azide moieties can be introduced by simple stirring of an aqueous oxo-G dispersion with NaN_3 and subsequent lyophilisation. B) Dynamic structure model according to Dimiev *et al.*: The reaction illustrates the C-C bond cleavage due to basic conditions.[77] C) A vacancy defect in the lattice of oxo-G.

4.4. Chemically Exfoliated Graphene

Chemically exfoliated graphene can be obtained *via* different routes. Ultrasonication of potassium intercalated graphite in THF or DMSO was found to yield almost intact graphene flakes.[51b] However, a more efficient way to produce large amounts of graphene is the reduction of oxo-G on surfaces or in bulk by either chemical treatment, temperature annealing, electron beam or electrochemical reduction.[75, 81, 83] On surfaces, reduction of oxo-G by hot vapour of hydrogen iodine and trifluoro acetic acid offers the best performance and results in completely reduced graphene sheets.[81, 84] Other reducing agents like hydrazine, borohydride and metal hydrides, ascorbic acid glutathione and many other substances can lead to graphene with similar or higher amounts of residual lattice defects as there may be still moieties bound onto the carbon lattice or additional vacancy defects are formed .[81, 85] After complete reduction vacancy defects remain in the carbon lattice as they are permanent defect sites as it can be seen in high-resolution transmission electron microscopy images (HR-TEM, **figure 6**).[10, 51b, 75] However, those defects can be partially healed by thermal processing in the presence of a carbon source.[86] The presence of anionic surfactants like e. g. sodium cholate (SCH), sodium dodecyl sulphate (SDS) or sodium dodecylbenzenesulphonate (SDBS) or cationic surfactants like e. g. tetrabutylammonium or cetyltrimethylammonium salts avoid aggregation of individual graphene sheets during liquid phase reduction.[9, 87] Temperature annealing is often used to cleave functional groups from the carbon lattice, but a negative side effect is the coincident introduction of vacancy defects by CO/CO_2 formation by disproportionation of the oxygenated graphene sheets.[81] Recently, it was shown that not every oxo-moiety on oxo-G forms a vacancy defect.[71b]

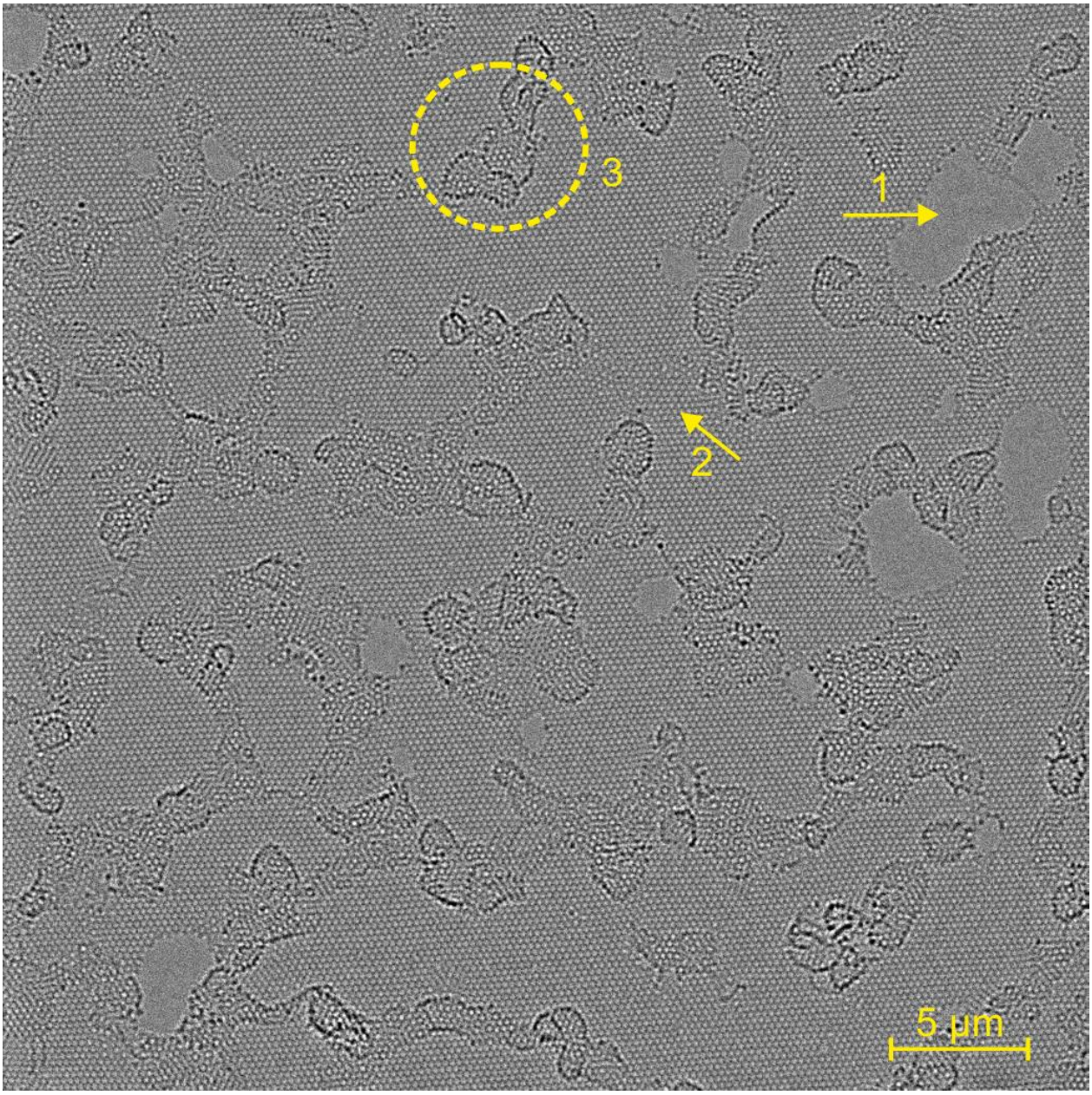

Figure 6 HR-TEM image of the carbon lattice of oxo-G. The functional groups were completely removed by electron beam irradiation. Larger holes in the carbon lattice (yellow arrow, 1) and areas with disturbed symmetry by point defects and non-six membered rings (yellow arrow, 2) are distributed all over the carbon lattice. Amorphous carbon impurities are spread in clusters all over the carbon lattice (3).

5. Analytical Methods and Techniques

5.1. Thermogravimetric Analysis Coupled to Mass Spectrometry (TGA-MS)

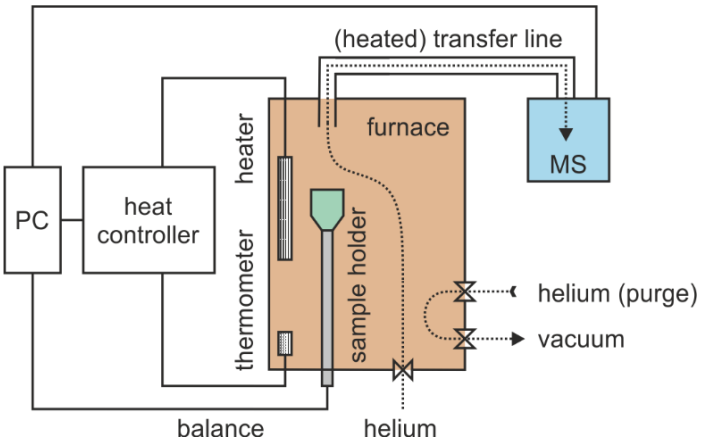

Figure 7 Schematic overview of a TGA-MS device. The evacuable furnace (brown box) including a sample holder with a crucible (green) and thereto connected mass spectrometer (blue box) by a heated transfer line is shown. Gas flows are illustrated by dotted arrows. The temperature in the furnace is monitored by a heat controller, and the recorded data are transferred to a personal computer (PC).

Thermogravimetric analysis (TGA) coupled to mass spectrometry (MS) gives insight into the degree of functionalisation (θ_{FD}) and composition of moieties bound to graphene. A sample is precisely weighed in a crucible on a sample holder and slowly heated to temperatures of 1000 °C or more in an inert gas atmosphere, usually nitrogen or helium. Due to the absence of oxygen combustion of the materials to be measured is avoided. While the sample is heating up, functional groups cleave at distinct temperatures. The mass of the sample is continuously recorded while cleaved fragments are transported by an inert gas flow to an ionisation chamber before they are analysed by a mass spectrometer (**figure 7**). The detection of specific fragments at specific sample temperatures gives information about their nature and binding strength and thus helps to discern between covalent and non-covalent functionalisation. An additional gas chromatography column (GC) prior to the MS can be used to separate fragments with similar *m/z* values but different retention factors.

Figure 8 shows some typical TGA curves of different graphene derivatives and TGA-MS of oxo-G synthesised according to Eigler. The first mass loss up to a temperature of ~ 120°C can be attributed to physisorbed water molecules (*m/z* 17/18). In the next step (120-180 °C), epoxide and hydroxide moieties are cleaved by disproportionation of the oxygenated graphene lattice leading to CO and CO_2 formation (*m/z* 28/44). In the last step between 200-300°C, decomposition of heavy sulphuric acid ester moieties leads to a very high mass loss and the formation of CO, CO_2 and SO_2 (*m/z* 28/44/64). This shoulder disappears after hydrolysis of sulphuric acid esters by washing the material with basic or acidic solutions (**figure 5, 8B**). These temperature values can be upshifted after applying post-treatment (e.g. temperature, acidic/basic milieu, partial reduction) due to the loss or rearrangement of less-stable moiety conformations. Isotopic labelling of moieties can help to distinguish cleaved fragments with similar *m/z* values but different composition. In **figure 8D** TGA-MS traces of as-prepared oxo-G and base washed oxo-G after treatment with sodium azide to introduce N_3-groups are shown.[80] However,

as the cleavage product of bound azide groups to oxo-G is N_2 (*m/z* 28) and since it has the same mass-to-charge ratio as CO (*m/z* 28), it cannot be distinguished. The use of isotopically labelled $Na^{15}N\text{-}^{14}N_2$ leads to a decomposition product with *m/z* 29, and thus a successful functionalisation is confirmed.

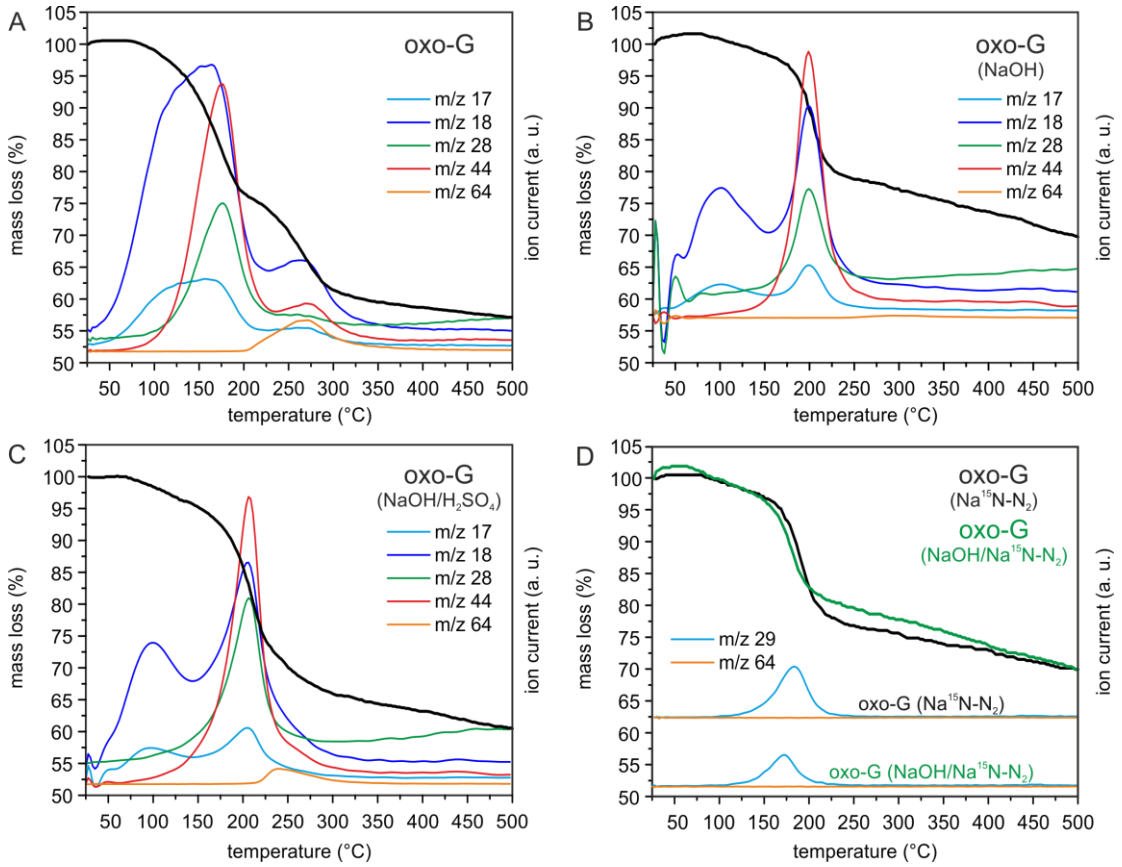

Figure 8 TGA-MS of oxo-G produced with 2 equivalents of $KMnO_4$ at low temperatures.[5b] Corresponding *m/z* traces are noted in the inset. B) TGA curve of base washed oxo-G without covalent bound sulphuric acid esters (*m/z* = 64) at about 250 °C. C) Base-washed oxo-G after mixing with cold sulphuric acid overnight: A minor amount of sulphuric acid esters could be reattached. D) oxo-G (black) and base-washed oxo-G (green) after stirring with aqueous $Na^{15}N\text{-}N_2$, freeze-drying and washing with pure water. Both, sulphuric acid esters as well as epoxides were substituted or underwent ring-opening respectively, to form azide moieties.

5.2. Statistical Raman Spectroscopy (SRS)

The inelastic Raman scattering process is an absorption-emission process of photons and has come to be one of the most important tools for characterizing carbon allotropes. Since Raman scattering is not a resonant phenomenon like fluorescence, the scattering process takes place *via* virtual states (like e.g. Rayleigh scattering). If a photon interacts with matter, there is a small probability that the photon will scatter with a red- or blue-shifted energy changing rotational and vibrational states of molecules or vibrational states in crystals. Therefore, emission of photons with lower (Stokes scattering) or higher energies (Anti-Stokes scattering) than the excitation wavelength can be detected (**figure 9A**). Graphene has no bandgap and thus it is in first approximation resonant in a wide range of wavelengths.[31a, 88] Raman spectroscopy can be used to measure degree of disorder,[68b, 88-89] number and stacking order of graphene layers,[90] doping,[91] strain and stress,[92] oxidation,[93] chemical functionalisation[93b, 94] and nature of edges[95] of graphite, graphene and related materials. For single layered graphene, three main peaks are of major interest: The D mode at ~ 1350 cm^{-1}, the G mode at ~ 1582 cm^{-1}, and the 2D mode at ~ 2700 cm^{-1} (using a 514 nm/2.41 eV laser for excitation).[31a, 96] The G mode is the only mode originating in a first-order Raman scattering process. It is associated with a doubly degenerated phonon mode of one in-plane transversal optic and a longitudinal optic phonon with E_{2g} symmetry at the Brillouin centre. Both, the D and 2D mode result from a second-order processes near the K point. The D mode is due to a

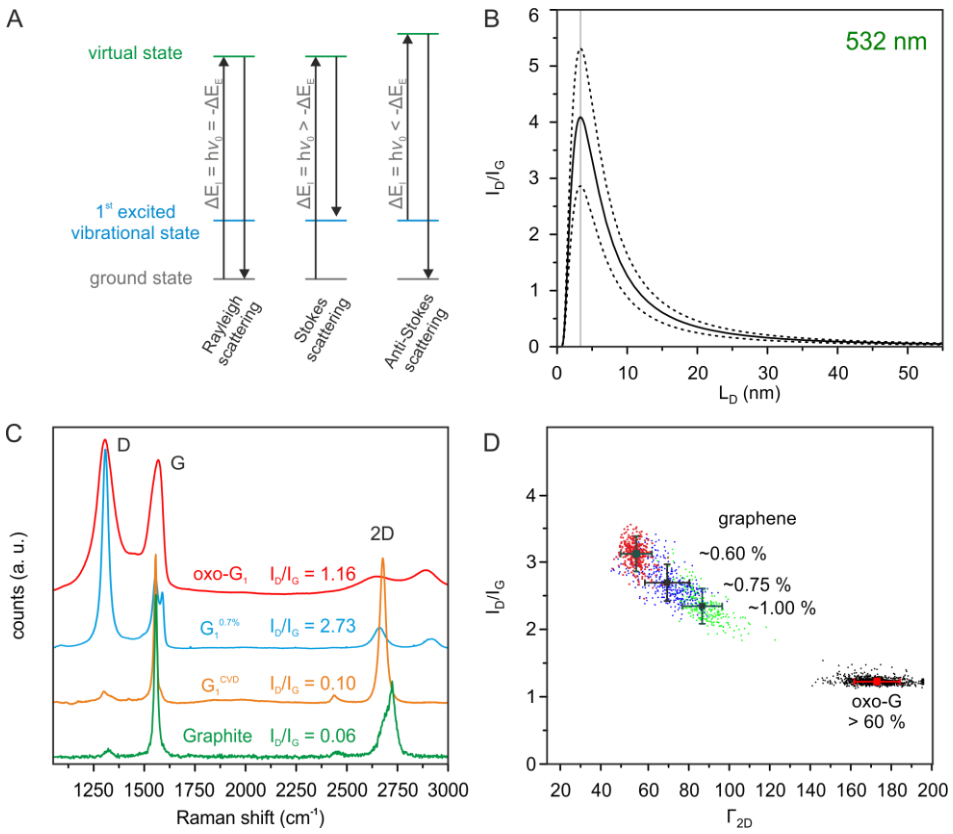

Figure 9 A) Raman process. B) Relation between I_D/I_G according to Cançado and Lucchese *et al.* The vertical line separates the high-defect regime (left) and low-defect regime (right).[88] C) Raman Spectra of oxo-G (red), graphene with 0.7 % of vacancy defects (blue), CVD graphene (orange) and graphite (green). D) Statistical Raman spectroscopy applied on graphene with different densities of defects in relation to carbon atoms and highly functionalised oxo-G. Figure 9B and C were reproduced from the literature.[9, 89]

breathing mode of six membered rings in graphene and a defect, and one in-plane transversal optical phonon is required. However, the 2D mode requires two in-plane transversal optical phonons without any defect for activation.[31a, 96]

Evaluation of the area (*A*), Intensity (*I*), Position (x_c), and full-width-at-half-maximum (*Γ* or FWHM) of all modes can be used to determine changes in the quality of graphene-based materials.[68b, 89, 97] In most simpler cases, the D (~ 1350 cm^{-1}), G (~ 1580 cm^{-1}) and 2D (~ 2700 cm^{-1}) modes can be compared in order to extract the density of defects in graphene-based samples (**figure 9C**).[88] Generally, the D mode is absent in defect-free graphene and arises with the introduction of either vacancy or functional defects. At an average distance between the defects (L_D) of ~ 3.3 nm, the wavelength-dependent I_D/I_G ratio reaches a maximum, which is about 4 at an excitation with a 532 nm laser. It is higher for larger wavelengths and *vice versa*. With a further increase of the density of defects (decreasing L_D) the I_D/I_G ratio decreases again to ~ 1.0 (**figure 9B**). To overcome misinterpretation of two different graphene-based samples with similar I_D/I_G ratios but different densities of defects (θ_D), we must distinguish between the *low-defect regime* ($L_D \geq 3.3$ nm) and the *high-defect regime* ($L_D \leq 3.3$ nm). This is possible by evaluating *Γ* of these three Raman modes, as they begin to broaden with increasing density of defects.[88] The values of Γ_G, Γ_D and Γ_{2D} stay almost constant for low θ_D and begin to increase for $L_D \leq 5$ nm.[88] For very low amounts of defects, the Tuinstra-Koenig relation (**1**) can be used to correlate the I_D/I_G ratio of a Raman spectrum of graphite and graphene to an average crystallite size L_a.[98] Tuinstra and Koenig noticed, that the I_D/I_G ratio varies inversely with the crystallite size, but anyway, it is only precise for very low amounts of defects in the lattice structure.[31a]

(**1**)

$$\frac{I_D}{I_G} = \frac{C(\lambda)}{L_a}$$

A more precise formula to correlate the I_D/I_G ratio to the distance between two defects L_D in the high and low-defect regime was published by Lucchese and co-workers (**2**):[88]

$$\frac{I_D}{I_G} = C_A \frac{(r_A^2 - r_S^2)}{(r_A^2 - 2r_S^2)} [e^{\frac{-\pi r_S^2}{L_D^2}} - e^{-\frac{\pi (r_A^2 - r_S^2)}{L_D^2}}] \quad (\mathbf{2})$$

The corresponding plot of formula (**2**) as a function of L_D is shown in **figure 9B**. C_A is a parameter depending on the excitation wavelength, and describing a maximum possible I_D/I_G ratio. The radii r_S and r_A describe the area of structurally disordered graphene due to defect (S) and the surrounding activated graphene lattice, which contributes to the D mode, respectively.[89] This formula is useful to analyse materials with less than 1% defects per unit area since it becomes less accurate at higher defect concentrations. It is not possible to discriminate graphene-based samples with 4% or 66% of defects *via* the I_D/I_G ratio since it is approximately the same. Recently, Vecera *et al.* could analyse materials located in this high-defect regime by the analysis of the absolute intensity of the G mode, because the D and G mode become more intense with increasing density of defects.[93b] To elucidate the density of vacancies (θ_V) next to oxo-functional groups, oxo-G has to be reduced completely to graphene without any residual moieties by any arbitrary method. In literature it was demonstrated that the hot vapours of hydrogen iodide and trifluoroacetic acid are very efficient to reduce oxo-G deposited on Si/300 nm

SiO_2 wafer.[81] As wet chemically produced oxo-G or graphene flakes in a dispersion reaction do not have equal densities of defects, statistical Raman spectroscopy (SRS) has to be applied on large maps to measure the average densities and standard deviation of a synthesised batch in a precise way (**figure 9D**).

5.3. Infrared Spectroscopy (FT-IR)

Fourier-Transformed Infrared Spectroscopy (FT-IR) can be used to analyse the presence of functional groups on oxo-G or other functionalised graphene derivatives. According to Mecke, absorption of photons with a certain energy leads to vibrational excitation of valence bonds, namely stretching and deformation.[99] In a polyatomic system, this process results in symmetric and antisymmetric stretching, scissoring, rocking, wagging and twisting motions. In molecular motifs, where one atom is bound to less than 4 substituents, some of these motions are forbidden, because those modes need atoms in a special geometrical relation to each other. Thus, they can be simply interpreted a rotation motions.[100] As the absorbed energy is dependent on the type and arrangement of atoms, isotope markers can be used to precisely identify absorption bands due to their differences in absorption.

For the analysis of graphene, its functionalised derivatives or related composites in the view of functional groups bound to the basal lattice structure, a dispersion or a powder of these materials can be deposited and dried on *e.g.* ZnSe windows, ground with KBr and compressed into pellets for transmission spectroscopy, or simply measured in dry state by attenuated total reflection (ATR). Oxo-G is a material mainly possessing hydroxyl, epoxide, carbonyl, carboxyl and organosulphate moieties and double bonds as further functional groups next to strongly physisorbed water molecules.[61a, 68a] Therefore, those resulting vibrational modes can be found in an FT-IR spectrum (**table 3, figure 10**). The broad absorption between 3200 cm^{-1} and 3800 cm^{-1} can be attributed to the presence of water and the stretching of O-H bonds in alcohols and water. A band at ~ 1720 cm^{-1} emerges from the stretching of carbonyl groups. Two often-overlapping bands at ~ 1620 cm^{-1} and ~ 1580 cm^{-1} arise from bending vibrations of physisorbed water molecules and aromatic or conjugated C=C vibrations. The band of hydroxyl groups on oxo-G can be found at ~ 1360 cm^{-1}.[68a, 101] Those hydroxyl groups can be esterified by sulphuric acid and thus, the peaks due to their vibrations can be found at 1225 cm^{-1} and 1183 cm^{-1}.[68a] After thermal treatment under inert gas conditions, signals for aliphatic C-H bonds can be found at ~ 2900 cm^{-1}.[101] Substitution of organosulphates and ring-opening of epoxides on oxo-G by the solid state reaction with sodium azide introduces azide moieties with signals at 2123 cm^{-1} and 2112 cm^{-1} respectively, for isotopic labelled azide (^{15}N-N_2).[8, 80]

Group	C-OH	>O	H_2O	>C=O	$-N_3$	C-H	$-OSO_3^-$	C=C
Absorption (cm^{-1})	~ 1400 ~ 1360	~ 1252	~ 1620 ~ 3200-3800	~ 1720	~ 2123 ~ 2112 (^{15}N-N_2)	~ 2900	~ 1225 ~ 1183	~ 1574

Table 3 Overview of the important vibrational modes in oxo-G, reduced oxo-G and related materials.

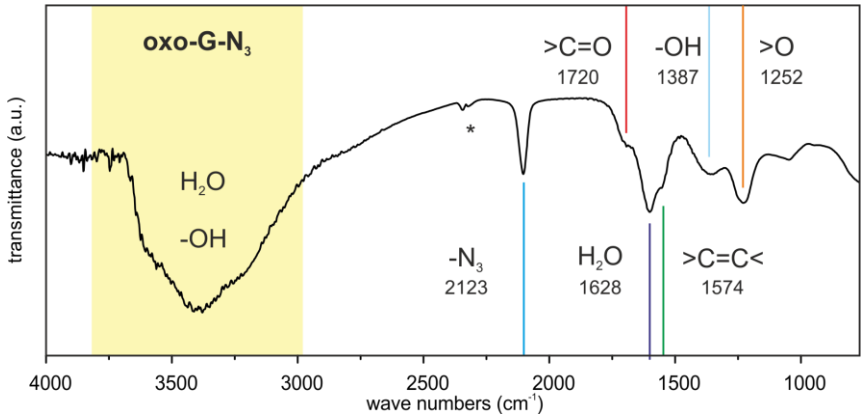

Figure 10 A) FT-IR spectrum of functionalised oxo-G with covalently azide moieties (oxo-G-N_3) after treatment with sodium azide. Vibrational modes assigned to functional groups and the position is given as numbers without units below (*cf.* **table 3**).

5.4. Extinction Spectroscopy (UV-vis)

Extinction spectroscopy is a versatile tool to easily determine concentration of oxo-G (Lambert-Beer law) or to estimate the amount of functional groups attached to the graphene lattice. In general, two main features appear (**figure 11A**): a maximum at ~ 234 nm corresponding to π→π*transitions of aromatic domains and a shoulder at ~ 300 nm corresponding to n→π* transitions of oxygen containing moieties like carbonyl or OH groups.[102] The position of the maximum is a good indicator to estimate the degree of functionalisation (θ_{FD}). The maximum gradually increases to values up to ~ 270 nm by progressing reduction. Furthermore, the shoulder at about ~ 300 nm begins to vanish, and total absorbance at higher wavenumbers begins to increase due to the loss of functional groups. [5b, 102-103] **Figure 11A** shows absorbance spectra of oxo-G derivatives with a declining degree of functionalisation. The initial oxo-G dispersion (0) contains about 65 ± 4% sp^3 carbon atoms, whereas a totally reduced oxo-G by sodium borohydride solution in the presence of sodium cholate (G/SCH) bears almost zero functional groups.[9, 73] Treatment with sodium hydroxide solution overnight (base), partial reduction with sodium borohydride (R) and the combination of both (base/R) lead to a partial loss of functional groups and thus, the spectral features lie in-between.[5b, 102] For comparison, the corresponding TGA-curves are shown in **figure 11B**. The strong decline of G/SCH at temperatures higher than 400 °C can be interpreted as the decomposition of added sodium cholate.[9]

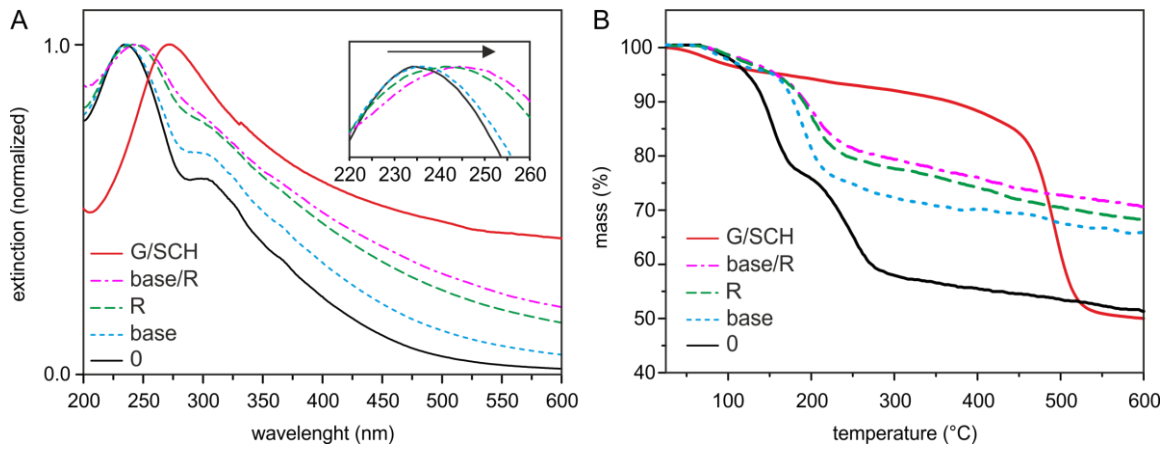

Figure 11 A) UV-vis spectrum of as synthesised oxo-G (0) with its main features corresponding to π→π* and n→π* transitions in comparison to three partially (base, R, base/R) and one fully-reduced oxo-G, whereas the latter one was stabilised by sodium cholate (G/SCH). A bathochromic shift in the maximum as well as the increase in the absorbance at higher wavelengths can be seen. B) The corresponding TGA traces of the recorded samples. Figure 11A and B were reproduced from the literature.[5b]

5.5. CHNS Elemental Analysis (EA)

In graphene oxide chemistry CHNS elemental analysis can be used to elucidate the presence and amount of covalent and non-covalent functional groups. Therefore, a small portion of the sample is precisely weighted, wrapped in a tin foil and combusted at temperatures up to 1150 °C for a few seconds in a helium-oxygen atmosphere to form CO_2, H_2O, N_2, NO, NO_2, SO_2 and SO_3 in quantitative amounts. Vanadium pentoxide can facilitate combustion, but is often not necessary to be added for graphene based samples. In a post following reduction chamber filled with copper, nitrogen oxides and sulphur trioxide can be reduced quantitatively at 850 °C to elemental nitrogen and sulphur dioxide. The resulting products are then separated by gas chromatography with several adsorption columns working at different temperatures and quantified. Typically, oxo-G produced after our established protocol contains about 45% carbon, 47% of oxygen, 5% sulphur and 2-3% hydrogen.[5b]

Certainly, the greatest advance of this technique is the need for less than 1 mg of oxo-G for a single measurement to estimate the carbon content and degree of functionalisation. Nevertheless, enclosed solvent molecules can falsify results of EA easily. Furthermore, it has to be taken into account that even after week-long lyophilisation 8-15 wt.% of strongly physisorbed water molecules remain adsorbed to the surface of oxo-G. The reason is the presence of acidic organosulphates and carboxylic acids, where hydronium ions act as counter ions, and high density of hydroxyl groups able to build H-bonds with water.[104] The This aspect is influenced by the degree of functionalisation and composition of moieties bound to oxo-G as they are responsible for the ability to bind water.[73] Thus, alignment of a once-established method of oxo-G preparation by solid state NMR should be considered if possible.

5.6. Atomic Force Microscopy (AFM)

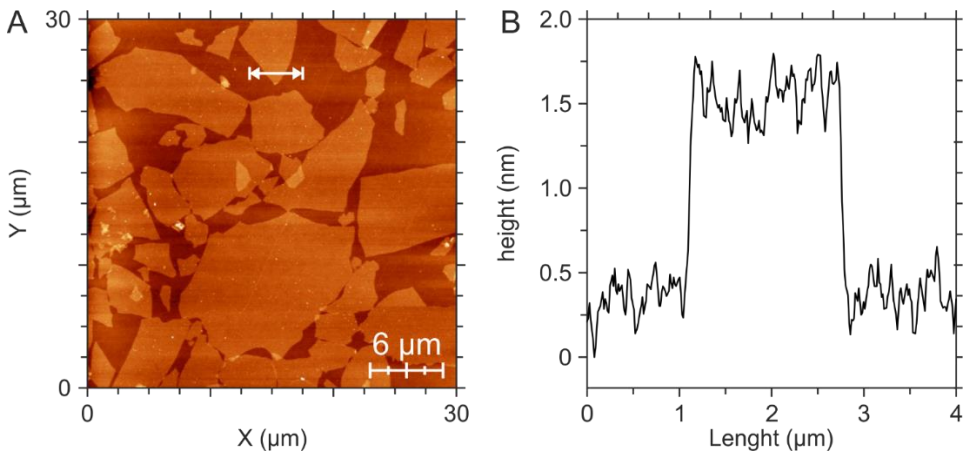

Figure 12 A) 30x30 µm sized AFM image of a Si/300 nm SiO_2 wafer coated with oxo-G by the Langmuir-Blodgett technique. The surface pressure before extrication was 1.5 mN/m and intermittent mode was chosen for recording the image. B) Height profile of an oxo-G flake of the left image. The position of the profile in the AFM image is indicated by a white line in the upper part. The height was determined to be about 1.2 nm.

Atomic force microscopy is versatile tool to probe surfaces and gain information about the topology of a surface. With advanced techniques, even mechanical and electronic properties of those surfaces can be probed. Therefore, a tip mounted on cantilever scans an area in X/Y direction, while changes in the deflection of a laser beam from the back of the cantilever gives information about the tip-surface interaction (**figure 12**). For standard imaging, several basic drive modes in different variations can be used to probe the surface: Contact mode, non-contact mode, and intermittent mode (tapping mode). As the name contact and non-contact mode imply, the cantilever scans and probes the surface with or without physically contacting the surface. In contact mode, the cantilever can be driven either in constant height mode, where the alternating deflection of the cantilever is used to measure the topology, or constant force mode, where a voltage used to regulate the height of the cantilever is measured. However, this way of probing surfaces can mechanically damage the sample and the cantilever gets damaged over time. In non-contact mode, the cantilever oscillates at or near its resonant frequency during the scan. Long-range forces influence the resonant frequency and a feedback loop system will regulate the tip-to-sample distance in order to maintain its prior tuned oscillation. However, a disadvantage of this measuring mode is, that is it quite sensitive to moisture on the surface and thus, it is used mostly under high-vacuum conditions. Especially in the case of wet chemically prepared oxo-G or graphene being probed under ambient conditions, an intermittent mode should be chosen to overcome problems by impurities leading to a variety of problems such as adsorbed dirt on the cantilever tip or scratched samples. Similar to the non-contact mode, it belongs to the dynamic modes as the cantilever is also oscillating. Here, the working distance is between contact mode and non-contact mode and acting van der Waals forces, dipole-dipole interactions and electrostatic forces cause changes in the oscillation frequency, and a feedback loop is used to keep the oscillation frequency constant.

5.7. Analytical Ultracentrifugation (AUC)

The fundaments of modern analytical ultracentrifugation lie in the research of Theodore Svedberg in 1920, in which he analysed the sedimentation behaviour of proteins. Based on his results, the technique of analytical ultracentrifugation is nowadays used to probe the sedimentation velocity of macromolecules and particles by applying round centrifugation force (RCF) on a liquid sample while the concentration of the macromolecules at one specific point (differential) or over the whole length of the cell (integral) is spectroscopically recorded in real time. The sedimentation velocity of particles in a liquid system is influenced by many factors. Mainly responsible are the applied centrifugal force, properties of the liquid media, and a particle's mass, density and shape.[105] Especially the latter aspect is of interest, as it influences the buoyant force, diffusion and drag coefficient in a liquid system.[105a] In general, the sedimentation coefficient , *s*, of a particle is used to describe the sedimentation behaviour in a liquid system independent from the applied RCF. It is given in *svedberg* (S or Sv; unit: 10^{-13} seconds) and is a non-linear and not additive factor.[105a]

Sedimentation velocity experiments can be used to easily determine the lateral size of oxo-G nanoparticles. Therefore, the sample to be is centrifuged in beakers bearing transparent windows and changes in the concentration are measured in real-time by an UV-vis spectrometer (**figure 13).** The relative error for the determination of the mean sheet diameter was determined to be 0.25 % by this technique and is thus highly precise.[105a, 106] Consequently, time-consuming and error-prone size analysis by microscopy can be avoided.[105a]

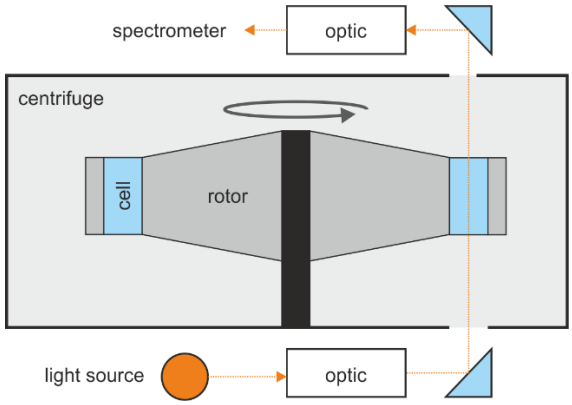

Figure 13 Schematic construction of an analytical ultracentrifuge. A spinning rotor equipped with transparent cells can be seen in the centre. Sedimentation behaviour of any material is monitored by an absorbance spectrometer detecting changes in the absorbance at a fixed position.

5.8. Coating by Langmuir-Blodgett Technique (LB)

In the view of downsizing devices, the controlled production of conductive mono- and multimolecular films is of high interest.[107] To prepare those, the Langmuir-Blodgett technique may be the easiest and most precise way. For this case, the surface to be coated is completely immersed into a rectangular trough filled with a liquid before the coating material (amphiphile or nanoparticle) is dropped on top of the liquid's surface. The amphiphilic coating agent can undergo interaction with the liquid and air at the water-air interface and thus reduces the surface energy of the system. Barriers at the rim of the trough can reduce the surface area by compression (**figure 12**). During this process, the distance between molecules or nanoparticles decreases continually and they begin to form a more and more closed film floating on the liquid. While isothermal compression proceeds, the structure of the monomolecular passes a series of two-dimensional states (gas, liquid, liquid crystal and solid).[108] Consequently, the surface tension of water changes and is recorded by a tensiometer equipped with a Wilhelmy plate (**figure 14B**). The surface properties can be tuned and materials are deposited on the immersed surface by slowly removing the substrate from the liquid. Almost closed arrays of oxo-G nanoparticles can be obtained by extrication of the surface at a surface pressure of 3-6 mN/m (*cf.* **figure 12**).

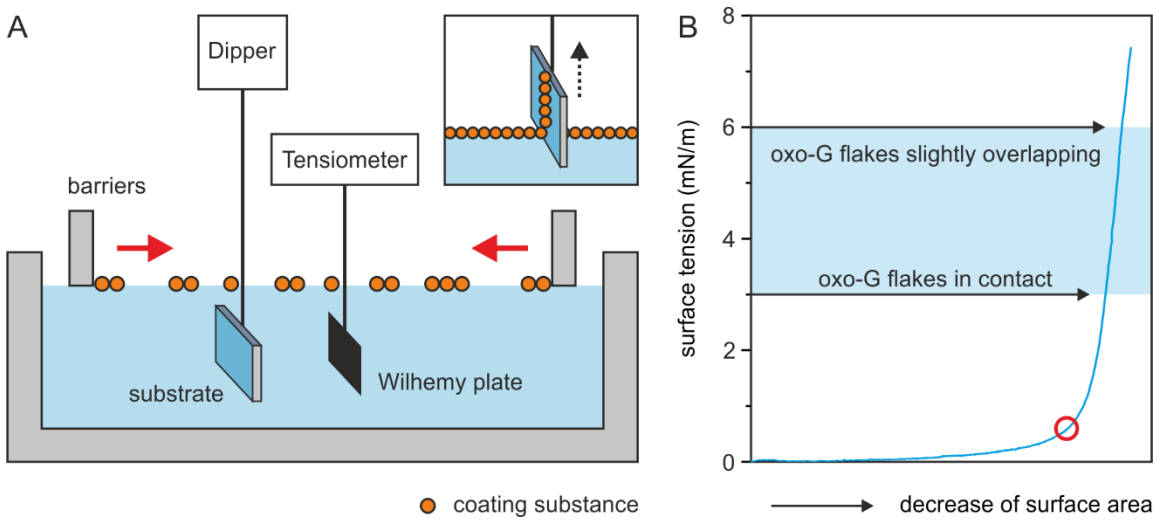

Figure 14 A) Schematic illustration of a Langmuir-Blodgett-device. Barrier movement is indicated by red arrows. The inset shows the deposition process after compression proceeded in a simplified way. B) Graph of the surface tension *vs.* surface area. The oxo-G particles approach to each other due to the barrier compression until the tipping point (red dot). In the range of 3 to 6 mN/m (blue area), the best results can be obtained. At a surface pressure of 3 mN/m, the surface to be coated (e.g. Si/SiO_2 wafer) is extricated and an almost closed film of oxo-G is obtained (*cf.* **figure 12**).

6. Synopsis of Results

Please note that for the sake of clarity that the term oxo-G is used instead of GO throughout this section. Thus, abbreviations for all used materials may differ from the original publication to fit to the style of this thesis.

6.1. Formation and Properties of oxo-Functionalised Graphene

a. Effect of Friction on Oxidative Graphite Intercalation and High-Quality Graphene Formation

S. Seiler, C. E. Halbig, F. Grote, P. Rietsch, F. Börnert, U. Kaiser, B. Meyer, S. Eigler; *Effect of friction on oxidative graphite intercalation and high-quality graphene formation*. Nat. Commun. **2018**, *9* (1), 836 **7.1**

Commonly-used protocols to oxidize graphite, like the famous Hummers´ and Offeman's method, use harsh oxidation conditions and yield oxo-functionalised graphene sheets in high yields. Nevertheless, these methods strongly harm the hexagonal lattice structure.[51c, 61b, 68b] In 2015, a novel method to synthesize low-functionalised oxo-G with an almost intact lattice structure *via* the formation of graphite sulphate, a graphite intercalation compound with the approximate formula $C_{24}^{+}HSO_4^{-}$ x 2 H_2SO_4, was published by Eigler *et al.*[55a]

However, the formation of stage-1 graphite sulphate and the subsequent isolation of oxo-G after aqueous workup is still not entirely understood, as there have been other workgroups reporting deintercalation instead of functionalisation with oxo-functional groups.[67, 109] To elucidate the mechanism behind this process, we investigated the oxidation and intercalation behaviour of three different types of graphite in detail. We used two highly crystalline natural graphite types (NG_1, NG_2) and one turbostratic graphite without any significant stacking order (TG) as determined by Raman spectroscopy and X-ray powder diffractometry (XRPD). Using *in-situ* Raman spectroscopy we found that turbostratic graphite was negligibly-oxidised by a mixture of $(NH_4)_2S_2O_8$ and H_2SO_4, while both NGs become heterogeneously oxidised along grain boundaries. Dark-blue regions forming stage-1 graphite sulphate could be identified as well as regions with greenish to purple colour, where complete intercalation was hindered. Thus, it was only possible to isolate oxo-G from both NGs, but not for TG after exposure to water, subsequent purification and delamination by ultrasonication. The quality of the obtained oxo-G and derived single layer graphene was analysed by UV-vis, atomic force microscopy (AFM) and statistical Raman spectroscopy (SRS). In a prior study we determined the degree of functionalisation of oxo-G, which was prepared by this method, to be about 4% as determined by thermogravimetric analysis in combination with a mass spectrometer (TGA-MS). The particle sizes of oxo-G were up to 10 µm and the determined density of vacancy defects in the related graphene flakes after quantitative reduction was about 0.025% (I_D/I_G = 1.2 ± 0.2, Γ_{2D} = 36 ± 3 cm^{-1}). High-resolution transmission electron microscope (HR-TEM) images confirmed the high quality of the lattice structure with minor amounts of point defects, and the distance between two defect sites was determined to be about 11 nm.

As the used graphite sources differ in their stacking order, grain and crystallite size, representative *ab-initio* molecular dynamic (*ai*MD) simulations were used to analyse the influence of their structure in the view of oxidisation and intercalation. One can assume that reduced cohesion between each graphene layer in TG facilitates intercalation and consequently the oxidation process between each layer of graphite. However, *ai*MD simulations performed for sulphuric acid-intercalated graphite with AA and AB stacking, either in neutral or oxidised state with a formal charge of C_{30}^{+}, indicate the opposite because the Green-Kubo friction coefficient is significantly reduced by oxidation or the change of the stacking order from AA to AB. This is corroborated by the observed lateral probability distribution of all oxygen atoms along the trajectory on the underlying graphene lattice. In AA-stacked graphite, the strongly electronegative oxygen atoms of sulphuric acid reside above and below the centre of each hexagon to minimize interaction with the electron-rich π-system. Consequently, the interaction between the exposed positively polarised hydrogen atoms of the sulphuric acid with the electron-rich π-system of both graphene layers is mainly responsible for the friction between the sulphuric acid and the graphene layers. Consequently, a displacement of the sulphuric acid molecules must overcome an energy barrier and is thus reduced by oxidation of the carbon layers. In contrast, the distribution of oxygen is less localised in AB stacked graphite than in AA-stacked graphite. In AB-stacked graphite there is always one carbon atom above and below the centre of a carbon hexagon due to the translation of the lattice. Thus, the observed probability distribution of oxygen can be identified as the combination of two corresponding shifted graphene/sulphuric acid layers and results in a strong decrease of the friction coefficient. In summary, both oxidation and ideal AB stacking contribute to a reduced free energy barrier for the movement of sulphuric acid molecules parallel to the graphite sheets.

Furthermore, we investigated the stability of hydroxyl and epoxide groups next to a formal oxidation state of C_{30}^{+} within the sulphuric acid-intercalated graphite stacks. To achieve functionalisation of the carbon lattice with *e.g.* hydroxyl groups, oxygen can either be transferred directly onto the carbon lattice by the oxidizing agent or alternatively by a separate oxidation and subsequent reaction of a positive C_{30}^{+} cell with water molecules. Our performed *ai*MD simulations revealed that hydroxyl groups on the graphene lattice are unstable below a formal oxidation state of C_{30}^{+}. Together with the knowledge, that the degree of functionalisation with hydroxyl groups was determined to be about 4% (1 moiety on 25 carbon atoms), it is unlikely that the rather bulky oxidizing agent needs to enter the interlayer space for oxidisation. Instead, we assume that the electron transfer from conductive graphene sheets in a graphite stack to the oxidation agent can take place at the edges. Thus accumulated positive charges in each single graphene layer are balanced by Grotthuß diffusion of protons through the hydrogen bond network of the intercalated sulphuric acid molecules.

b. Graphene Oxide – A one or two component Material

A. Naumov, F. Grote, M. Overgaard, A. Roth, C. E. Halbig, K. Nørgaard, D. M. Guldi, S. Eigler; *Graphene oxide: A one- versus two-component material.* J. Am. Chem. Soc. **2016**, *138*, 11445-11448 **8.1**

A widely used but deceptive *two-component structural model* of oxo-G proclaiming weakly oxidised graphene sheets decorated by highly oxygenated macromolecules (oxidative debris, OD) was challenged. These OD are formed during oxidation of graphite under harsh conditions and are strongly adsorbed onto oxo-G, but can be removed by basic workup to yield the "real" graphene oxide with a lower degree of oxygenation than the initial material. It was claimed that the chemical properties of oxo-G do not change during base-wash, and changes in the optical properties were consequently assigned to the removal of OD. However, since freshly prepared oxo-G is indeed sensible towards basic conditions and elevated temperatures, we checked the proposed model with different oxo-G derivatives obtained by mild ($G_1OH_{4\%}$, derived from graphite sulphate), medium (oxo-G^E; Eigler's method) and harsh (oxo-G^H; Hummers' method) oxidation and studied the optical properties of all oxo-G derivatives and OD in detail.[68a, 76a, 110] Our fundamental idea was that mild oxidation conditions should result in the formation of fewer amounts of OD in comparison to harsher methods. Consequently, oxo-G synthesised according to Hummers and Offeman should bear most OD. For all of these materials, we applied the protocol to separate OD from oxo-G according to Rourke *et al.* and combined them again to artificial two-component systems with our prepared oxo-G derivatives. The optical properties for all individual and combined compounds were analysed by absorbance, emission spectroscopy, and femtosecond lifetime measurements.

Absorption spectra (UV-vis) of base-treated samples of oxo-G^H and oxo-G^E exhibit similar features to the spectra of partially reduced oxo-G, independent of the initial amount of OD. Furthermore, the fluorescence of untreated oxo-G^E and oxo-G^H is high, but decreases irreversibly for base treatment up to three hours at 70 °C. Thus, changes in absorption and emission spectra cannot be ascribed solely to the removal of OD by base wash, but also to the decomposition of oxo-G. Finally, we combined oxo-G^E with the OD, which were extracted from the oxidation mixture during oxo-G preparation (^{OX}OD) and as after base wash (^{base}OD). Both types of OD bear almost similar spectral characteristics. Similar to the literature, we detected fragments of low molecular weight mainly between *m/z* 100 and *m/z* 250 for ^{OX}OD. However, the combination oxo-G^E with either one of the isolated OD did not resemble the initial material before base treatment. We found further evidence supporting our hypothesis by analysis of fluorescence lifetime measurements of $G_1OH_{4\%}$, oxo-G^H, ^{OX}OD and ^{H}OD. The corresponding lifetimes for oxo-G^H and $G_1OH_{4\%}$ are calculated as 0.45 ns and 0.48 ns respectively. In stark contrast, both OD exhibit much higher lifetimes and are determined to be 3.6 ns for ^{base}OD and 0.76 ns for ^{OX}OD. A biexponential fit of the lifetime of ^{OX}OD (0.76 ns), revealed lifetimes of 0.45 ns and 1.9 ns. This indicates the presence of minor amounts of oxo-G in the isolated OD, although they could not be detected in the absorption or emission spectra. Our presented data of the optical properties of all oxo-G derivatives and isolated OD indicate that each type of oxo-G should be seen as a single component rather than a two-component.

6.2. Particle Size Control by Liquid Phase Processing

C. E. Halbig, T. J. Nacken, J. Walter, C. Damm, S. Eigler, W. Peukert; *Quantitative investigation of the fragmentation process and defect density evolution of oxo-functionalized graphene due to ultrasonication and milling.* Carbon **2016**, 96 (14), 897-903 **7.2**

T. J. Nacken, C. E. Halbig, S. Wawra, C. Damm, S. Romeis, J. Walter, M. J. Tehrani, Y. Ishii, S. Eigler, W. Peukert; *Structural factors controlling size reduction of graphene oxide in liquid processing.* Carbon **2017**, 125, 360-369 **7.3**

The synthesis of nanoparticles in specific size ranges can be useful to optimize the desired product for technical and biological application.[20b, 20d, 20e] Using wet chemical approaches, oxo-G nanoparticles with particle sizes up to tens of micrometres can be produced in large quantities.[111] The comminution of those particles can be easily achieved by external stressing with jet cavitation, ultrasound, ball milling and shear mixing.[5a, 44c, 50] In an earlier study from Gonçalves *et al.* about particle size reduction by ultrasonication, a confined *hot spot atomic reduction and fragmentation mechanism* was proposed, as the degree of functionalisation decreases during processing.[112] However, oxo-G was previously shown to be a metastable 2D material. It begins to alter its structure and properties slowly by *e.g.* elevated temperatures, which was not considered in their original experimental setup since they used no external refrigeration to keep the dispersion temperature at low temperatures.[7, 76b, 76c, 81] Thus, we conducted two detailed studies focusing on the investigation of the particle size reduction by ultrasonication and ball milling using analytical ultracentrifugation (AUC).

In our first study (Carbon **2016**), we used oxo-G with a low density of vacancy defects (0.8 %) and compared the size reduction rates during processing by ball milling and ultrasonication at different processing powers. The structural stability of oxo-G during processing was monitored by statistical Raman spectroscopy (SRS), absorption spectroscopy (UV-vis), atomic force microscopy (AFM) and thermogravimetric analysis coupled to a mass spectrometer (TGA-MS). The initial oxo-G had a particle size of about 1.55 µm at a concentration of 0.1 mg/mL, and we used external refrigeration to keep the temperature below 10 °C throughout our experiments. After specific processing times, small samples were removed and analysed by AFM, SRS and UV-vis. After ball milling and ultrasonication we observed *via* AFM and AUC that both methods lead to smaller particles sizes. Herby, the comminution process follows a power law function since the size reduction rates scale linearly as a function of the introduced energy in a doubly-logarithmic space. After ultrasonication at 40 Watts, particle sizes of about 70 nm could be obtained after 24 hours. In the case of ball milling using polystyrene beads, the same dispersion lead to average particle sizes of about 275 nm after 3 hours of processing. Interestingly, comminution by ultrasonication leads to a narrowing of the particle size distribution over the processing time, whereas the distribution strongly broadens during ball milling as this type of external stress is less size-selective with respect to the diameter of oxo-G sheets. Using SRS, we demonstrated that application of additional external refrigeration avoids thermally induced formation of additional vacancy defects in the carbon lattice. All recorded UV-vis spectra indicated, that the chemical composition of oxo-G did not change during processing. This aspect is important, because a precise particle size determination by AUC is easily sophisticated if the hydrodynamic sheet

thickness of oxo-G particles change during processing. In contrast to these observations, TGA-MS and UV-vis spectra varied strongly if no external refrigeration was used, indicating a decomposition of our material during processing. Thus, the earlier proposed *confined hot spot fragmentation and reduction mechanism* was found to be a combination of two individual effects: size reduction on one hand and degradation of the oxidised graphene flakes on the other hand.

In a second study (Carbon **2017**) we investigated the influence of functional groups and vacancy defects on the comminution rate of oxo-G during tip sonication. Therefore, different derivatives of oxo-G had been synthesised, with varying degree of functionalisation, composition of moieties and number of vacancy defects as analysed by elemental analysis (EA), TGA-MS, SRS and UV-vis. Comminution experiments were performed for all samples with external refrigeration analogous to our first study, and AUC was again used to determine size reduction rates of the prepared oxo-G derivatives. Our results indicate that the total degree of functionalisation, as well as the presence of organosulphates, mainly influenced the size reduction rate. We revealed that oxo-G bearing a high degree of functionalisation and decorated with many heavy organosulphates (-OSO_3H: 97 Da, -OH: 17 Da) had a faster comminution rate than similar oxo-G without organosulphates or other oxo-G derivatives with a lower degree of functionalisation. The number of vacancy defects was expected to have a larger influence on the size reduction since they may act as a predetermined breaking point in the hexagonal lattice. However, no trend could be observed as the total number of functional groups were orders of magnitude higher than the number of vacancy defects, and consequently overshadows their influence.

6.3. Bio-Compatibility of oxo-G

H. Pieper, S. Chercheja, S. Eigler, C. E. Halbig, M. Fillipović, A. Mokhir; *Endoperoxides revealed as origin of toxicity of graphene oxide.* Angew. Chem. Int. E. **2016**, 55 (51), 405-407	**8.2**
H. Pieper, C. E. Halbig, L. Kovbasyuk, M. R. Filipovic, S. Eigler, A. Mokhir; *Oxo-functionalized graphene as cell membrane carrier of nucleic acid probes controlled by aging.* Chem. Eur. J. **2016**, 22 (43), 15389-15395	**7.4**

It was previously shown that biomolecules like *e.g.* nucleic acids and other biologically-active molecules can reversibly bind to oxo-G.[113] Resulting compounds are able to penetrate cell membranes and release their cargo into the cell, which make them interesting for biological and medical application.[113b, 113c, 114] Hereby, differences in the physical and chemical properties of oxo-G affect its performance to act as a drug carrier in cells and determine as wells as its mutagenicity and cytotoxicity.[19c, 73]

a. Toxicity of oxo-G

In an initial study conducted by the group of Prof. Dr. A Mokhir, they elucidated the toxicity of oxo-G synthesised in our laboratory with a focus on the generation of harmful active oxygen species in cells (*Angew. Chem. Int. Ed.* **2016**). In general, active oxygen species like $^1O_2$ can be generated by thermolysis of endoperoxide-containing compounds. The existence of those moieties on oxo-G was already predicted in theory, and indirect evidence was already published in the literature. To clearly prove the existence of endoperoxides on oxo-G, we probed our material with two well-known $^1O_2$ trapping agents, namely 4,4'-(isoben-zofuran-1,3-diyl)dibenzoic acid and 9,10-di(3-hydroxypropyloxy)-anthracene. Interestingly, probing endoperoxides on oxo-G with both reagents lead to negative results, as their sensitivity was too low. To enhance the experimental sensitivity, a novel ON-AN-FL probe was developed in the group of Prof. A. Mokhir. It was built from an oligonucleotide chain (ON), which acts as an anchoring group and binds strongly to the surface of oxo-G *via* stacking between nucleobases and sp^2 domains or salt-mediated bridges with functional groups. Fluorescein (FL) acts as the reporting unit as its fluorescence is quenched as long as it is bound to the anchor group and thus in presences aromatic domains within the inhomogeneous functionalised graphene lattice. An $^1O_2$-sensitive anthracene linker (AN) was introduced to release FL if endoperoxides are present on the surface of oxo-G, which can be subsequently quantified by its emission spectrum.

We used this probe to detect endoperoxides on oxo-G. After the addition of freshly prepared oxo-G to a solution of ON-AN-FL, a strong decrease in the fluorescence of the solution could be detected. Within minutes, the fluorescence began to increase again due to the endoperoxide induced cleavage of the AN-FL bond and accompanied release of free FL. A concentration of one endoperoxide group per $2*10^4$ carbon atoms was derived from the recorded data for as-produced oxo-G. However, the increase of the fluorescence after oxo-G addition to ON-AN-FL was substantially lower if oxo-G was stored for up to three weeks or exposed to UV light, hinting towards a partial loss of this moiety.

Cell toxicity, or more precisely the ability to form reactive oxygen species (ROS), of prepared oxo-G derivatives was then probed by flow cytometry in combination with 2,7-dichlorofluoreceine diacetate. This molecule is non-fluorescent and intracellularly hydrolysed after cell uptake. Further oxidisation by intracellular ROS leads to fluorescein, which can be easily detected by its emission spectrum. With this toolkit it was demonstrated that base-treated oxo-G without any endoperoxides had a negligible influence on the concentration of ROS as no increase in the fluorescence could be detected. However, freshly prepared oxo-G with endoperoxides increased the amount of ROS in cells significantly. An influence of manganese traces, which are often present in freshly prepared oxo-G, could be excluded by control experiments and hence, we attribute the toxicity of oxo-G mainly to the presence of endoperoxides bound on oxo-G.

b. Oxo-G as a Cell Membrane Carrier Controlled by Aging

In a second study, we focused more on the effect of aging on the structure and properties of three different oxo-G samples stored for up to four weeks at different conditions with above-mentioned ON-AN-FL probes to fully control the cell toxicity and the properties as a cell membrane carrier (*Chem Eur. J.* **2016**). It was predicted by Zhou and Bongiorno that oxo-functional groups of oxo-G should be homogeneously distributed on the carbon lattice directly after synthesis and rearrange over time to form highly oxo-functionalised sp^3 domains and graphene-like patches. Presently, no clear experimental evidence has been given to probe these structural changes during aging of oxo-G. To elucidate this, we used our established fluorescence-marked probes (ON-FL and ON-AN-FL) and screened our differently-stored oxo-G samples every week.

Initially, we prepared a fresh oxo-G dispersion and stored it in a refrigerator at 4 °C and at room temperature (21°C) with and without exposure to light. Variations in the binding strength were investigated by non-covalent interactions between oxo-G and ON-FL from the day of synthesis up to four weeks later. Interestingly, freshly prepared oxo-G reduced the fluorescence of the ON-FL probe by only 2.1-fold, whereas the factor was increased to 29-fold after 28 days of dark storage at 4 °C. The aging effect was more pronounced if oxo-G was stored at room temperature, but already after 7 days, both materials behaved approximately similar. These data indicate that oxo-G increases its affinity towards the chosen ON-FL probe over time. However, analysis of the probed materials by statistical Raman spectroscopy (SRS), absorption spectroscopy (UV-vis) and thermogravimetric analysis coupled with a mass spectrometer (TGA-MS) could not reveal changes in the density of moieties or vacancies in the carbon lattice of cold-stored oxo-G. In contrast, samples stored at 21 °C degree and exposed to light bear a slight, but significantly lower degree of functionalisation and slightly increased density of vacancy defects. A detailed look at our recorded infrared spectra (FT-IR) and fluorescence spectra revealed slight changes between freshly-prepared oxo-G and corresponding cold aged materials. We observed a continually increase of a band at 1575 cm^{-1} (conjugated C=C) over storage time, which is almost absent in freshly-prepared oxo-G, and a slight increase of the total fluorescence emission. Both of these aspects combined with the above-outlined alteration of the binding strength between oxo-G and ON-FL give experimental evidence for a rearrangement of functional groups bound to graphene lattice.

We further assume that the above-mentioned rearrangement reactions may influence the stability of endoperoxides on the carbon lattice of oxo-G, which are present in minor traces. To investigate this aspect, we applied the $^1O_2$-sensitive ON-AN-FL probe on oxo-G after specific time steps beginning from the day of synthesis up to 28 days later. We observed that freshly-prepared oxo-G contained more endoperoxides than aged samples as probed by ON-AN-Fl. Interestingly, the loss of endoperoxides proceeds slower (14 days at 4 °C) than the rearrangement of functional groups on the carbon lattice (7 days at 4 °C). Based on our data, we assume a thermodynamically-driven mechanism for both processes since they depend on the storage temperature.

Since aging influences the structure and properties of oxo-G, we also assumed that the performance to act as a cell membrane carrier for oligonucleotides (ON) may change over time. Therefore, two types of toehold-type double strand probes targeting 28S rRNA and *β*-Actin mRNA were developed (FL-ON*/DNA). They consist of two partially-complementary strands, whereby one binds weakly to oxo-G and contains the fluorophore FL, and the other binds tightly to oxo-G. In the presence of the complementary DNA (reference) and cellular RNA strands (28S rRNA or *β*-Actin mRNA), F-ON*/RNA is released and was quantified by fluorescence spectroscopy.

For *in-vitro* experiments with HL-60 cells, the originally-used fluorescence-labelled DNA sequences were exchanged by similar nuclease resistant 2'-OMe RNAs to avoid decomposition inside human promyelocytic leukaemia cells (HL-60). We prepared aggregates of oxo-G and one toehold RNA-probe targeting 28S rRNA every week, starting from the day of synthesis up to four weeks. The obtained compounds were subsequently incubated with HL-60 cells for 1 hour while the fluorescence of the cells was recorded *via* flow cytometry. The results indicate, that the carrier properties of oxo-G improved over time. Using as-prepared oxo-G for our experiments, we detected a slight increase of the initial fluorescence by a factor of 1.4±1.2, whereas it increased by a factor of 28.8±1.6 when using oxo-G that was stored for 28 days.

Basing on this result, we used oxo-G aged for 28 days and investigated its properties when acting as an *in-vitro* cell membrane carrier for oligonucleotides into HL-60 cells. First, we performed a reference experiment with three different toehold-type double strand probes. Two target of them 28S rRNA and *β*-actin mRNA, whereas a third acts as a negative control without any specific intracellular target. After incubation of HL-60 cells with all three fluorescence probes in the absence oxo-G, a minor increase of the fluorescence by a factor between 1.8 and 4.3 could be observed. Thus, we conclude a negligible uptake of these compounds into the cytoplasm. However, the same experiment performed in presence of oxo-G increased the fluorescence by a factor of 21.3±2.2 (*β*-actin mRNA) and 28.2±1.7 (28S rRNA). Since a weaker increase in fluorescence was induced by the negative control (15.5±4), we presume an unspecific release of the fluorophore.

6.4. Controlled Functionalization of oxo-G and Graphene

a. Towards the Synthesis of Graphene Azide from Graphene Oxide

C. E. Halbig, P. Rietsch, S. Eigler; *Towards the synthesis of graphene azide from graphene oxide.* Molecules **2015**, 20 (12), 21050-21057 **7.5**

The synthesis of "pure" graphene derivatives with exclusively one type of moieties with distinct chemical and physical properties, e.g. graphane or fluorographene, is of strong interest in material science, but is still challenge for synthesis. Previously it was shown in literature that azide moieties can be bound onto oxo-G *via* substitution of sulfuric acid esters and ring-opening of epoxides to yield oxo-G-N_3. As azides are known to be useful compounds for 1,3-dipolar cycloadditions, *e.g.* the well-known copper catalysed Huisgen reaction, we synthesised azide-functionalised oxo-G and post-treated the obtained materials at elevated temperatures and chemically with sodium borohydride and hydrochloric acid in different concentrations with the aim to obtain "pure" graphene azide.

First, we synthesised oxo-G and introduced azide moieties next to hydroxyl groups *via* a solid state reaction with NaN_3 according to the literature. We performed analysis of the prepared material by elemental analysis (EA), Fourier-transform infrared spectroscopy (FT-IR), absorption spectroscopy (UV-vis), thermogravimetric analysis coupled to a mass spectrometer (TGA-MS) and statistical Raman spectroscopy (SRS). After functionalisation with sodium azide, we were able to detect an additional vibrational mode at 2121 cm^{-1} in our recorded FT-IR spectra. Since thermally induced decomposition of azide moieties during TGA-MS analysis results in the formation of $^{14}N_2$ with *m/z* 28, and can thus be confound with carbon monoxide, we functionalised oxo-G using ^{15}N-labelled sodium azide ($^{15}N^{14}N$: *m/z* 29). The occurrence of a new signal with *m/z* 29 provided further evidence for a successful functionalisation. The amount of azide moieties was determined by EA to be 3.3 w%, which implies a degree of functionalisation of about 2%.

With a focus on preparing graphene azide, we applied different chemical post-treatment conditions as well as thermal treatment on the obtained material and conducted a full characterisation. We found that the strongly-reducing sodium borohydride as well as thermal treatment at a temperature of 140 °C lead to the unspecific cleavage of functional groups on oxo-G-N_3. In all cases, the characteristic vibration of N_3-groups completely disappeared in FT-IR spectra. As an alternative to those techniques, we chose hydrogen chloride in several concentrations as it is a less powerful reducing agent in comparison to hydrogen iodide for the selective reduction oxo-G-N_3. Treatment of oxo-G with 0.5 M HCl or higher slightly altered the recorded FT-IR spectra dependent on the chosen concentration and reaction time. An increase of the band at 1575 cm^{-1} (C=C) and a decrease of a band at 1630 cm^{-1} (physisorbed H_2O) was witnessed indicating the formation of enlarged sp^2 domains and a partial cleavage of oxo-moieties, which are responsible for the physisorption of water molecules. However, the vibrational mode of azide moieties at 2121 cm^{-1} was still present after acid treatment. Using 2

M HCl, the nitrogen content of purified and freeze-dried oxo-G-N_3 was increased from 3.3 w% to 4.5 w%. Long-term treatment with 1 M HCl solution or shorter contact at higher concentrations of HCl (12 M) lead to a partial reduction of oxo-G-N_3 and an almost complete cleavage of any bound azide moiety as analysed by Raman and UV-vis spectroscopy. Structural changes of oxo-G-N_3 by HCl treatment were detected, but with the presented techniques it was not possible to obtain "pure" graphene azide. However, the presented work can be seen as one step forward towards the synthesis of graphene azide.

b. Oxo-Functionalized Graphene - A Versatile Precursor for Alkylated Graphene Sheets by Reductive Functionalization

---

C. E. Halbig, O. Martin, F. Hauke, S. Eigler, A. Hirsch; *Oxo-Functionalized Graphene - A Versatile precursor for alkylated graphene sheets by reductive functionalization.* Chem. Eur. J. **2018**, *24,* 13348-13354 **7.6**

Recently, reductive functionalisation was shown to be the only method to functionalise graphene sheets with alkyl moieties. To achieve this, graphite, mechanically exfoliated graphene or graphene obtained by CVD processes must be charged by strong reducing agents like sodium-potassium alloy (NaK) in 1,2-dimethoxyethan to increase the reactivity towards electrophilic alkyl iodides. However, the yield of functionalised single layered graphene sheets is strongly limited as CVD and mechanically exfoliated graphene can only be produced on surfaces, and functionalisation of bulk graphite leads to products dominated by multi-layered flakes.

To overcome this hurdle, we transferred the technique of reductive functionalisation to graphene derived from oxo-G as an alternative precursor. This material can be produced in large quantities and consists of exclusively single-layered sheets, but contains about 0.7 % vacancy defects due to the applied oxidative exfoliation. It can be easily deposited on surfaces to obtain graphene on substrates after quantitative reduction with hydrogen iodine and trifluoro acetic acid ($G_1^{0.7\%}$). Additionally, it can be directly reduced in the presence of sodium cholate as a surfactant in aqueous media. After lyophilisation, a black powder of graphene sheets separated by sodium cholate (G/SCH) was obtained. Deposited graphene and bulk G/SCH were activated by NaK in DME and further functionalised using hexyl iodide. After functionalisation, results of statistical Raman spectroscopy (SRS), temperature dependent Raman spectroscopy (dT-SRS) and thermogravimetric analysis coupled to mass spectroscopy with or without an intermediary gas chromatograph (TGA-MS; TGA-GC/MS) were compared to results using CVD-graphene and bulk graphite as precursors. For functionalised CVD graphene, we determined a degree of functionalisation of about 0.03 % with respect to the total number of carbon atoms in the graphene lattice by SRS. The same is true for functionalised bulk graphite, but with a lower degree of functionalisation. We expect a similar degree of functionalisation for $G_1^{0.7\%}$, since these materials differ only in their vacancy defect density. However, SRS becomes less sensitive with an increasing number of defects. We observed that the Raman spectra of pristine $G_1^{0.7\%}$ and the corresponding functionalised hexyl-$G_1^{0.7\%}$, which had an additional 0.03 % functional defects, did not differ significantly. Nevertheless, a successful functionalisation with hexyl moieties

was demonstrated by TGA-MS as typical mass fragments for the decomposition of alkyl groups could be identified for functionalised G/SCH and functionalised graphite in a similar range of temperature. TGA-GC/MS was used to avoid misinterpretation of the detected mass fragments, since simple TGA-MS cannot differ between physisorbed hexyl iodide and covalently bound hexyl moieties. It previously shown that thermal cleavage of covalently bound hexyl groups form the dimerisation product dodecane, which has a different retention factor than physisorbed hexyl iodide and can thus be separated by gas chromatography. We identified the assumed temperature at which hexyl groups detach from the carbon lattice for all samples, and we subsequently injected a gaseous sample of the fragmentation products at the assumed temperature into the GC column. By the analysis of the separated decomposition fragments using mass spectroscopy, we were able to identify the obligatory dimerisation product (dodecane) for both hexylated graphite and hexylated G/SCH. Thus we conclude that functionalisation of graphene derived from oxo-G with hexyl moieties is possible. As we witnessed by optical and atomic force microscopy, we were able to increase the yield of functionalized single layer graphene sheets using G/SCH instead of bulk graphite.

c. Selective functionalization of graphene at defect activated sites by arylazocarboxylic tert-butylesters

C. E. Halbig, R. Lasch, J. Krüll, A. Pirzer, Z. P. Wang, M. R. Heinrich, S. Eigler; **7.7**
Selective functionalization of graphene at defect activated sites by arylazocarboxylic tert-butylesters
submitted to Angewandte Chemie **09/2018**

Functionalisation of oxo-G and graphene leads to derivatives with tuned properties for biological and technical application. However, controlled functionalisation on surfaces or bulk material is still a hurdle for synthetic chemists. However, techniques and useful agents to successfully covalently functionalise graphene by C-C bond formation are still limited due to the high stability of the graphene and require highly reactive compounds. Previously, the group of Prof. Dr. M. R. Heinrich successfully demonstrated the arylation of unsaturated molecules by arylazocarboxylic *tert*-butylesters. Similar to diazonium compounds, these molecules can release aryl radicals in the presence of oxygen and trifluoroacetic acid, but without a single electron transfer, and thus bear a higher stability. In this work, we investigated the functionalisation of different types of graphene using four differently arylazocarboxylic *tert*-butylesters, substituted in *ortho*-position (4-R-ArN2Boc with R = -Br, -CN, -NO_2 or -OC_7H_{15}).

We synthesised a set of different graphene derivatives and used them for monotopic functionalisation on substrates and bitopic bulk functionalisation in dispersion. At first, we used graphene on a 300 nm SiO_2/Si-wafer with 0.5 % of vacancy defects (θ_{VD}). This type of graphene was obtained from oxo-G after quantitative reduction by a hot vapour of hydrogen iodine and trifluoroacetic acid (^{S}G, I_D/I_G = 3.38) and can be easily prepared in high yields. We immersed several wafer into a solution of 2 mM 4-R-ArN_2Boc in 50:50 acetonitrile:water, and subsequently activated 4-R-ArN_2Boc using a small amount of trifluoroacetic acid to induce the decomposition of ArN_2Boc and generate the corresponding aryl radicals. The functionalisation of graphene was performed at 60°C and 80°C to facilitate the aryl radical generation and to elucidate the influence of temperature with respect to the achieved degree of functionalisation over time. After specific reaction times up to 5 hours, one wafer was removed, thoroughly rinsed with several pure solvents of different polarity and analysed by statistical Raman spectroscopy (SRS). We observed, that the I_D/I_G ratio of ^{S}G decreases over a reaction time from 3.38 to ~ 1.5 due to the formation of sp³ defects. The final saturation point for all four 4-R-ArN_2Boc derivatives was reached after 120 minutes for the reaction performed at 60 °C or 30 minutes at 80 °C. According to Lucchese *et al.* we calculated a decrease of the distance between defects (L_D) from 2.3 nm to 1.6 nm and a corresponding degree of functionalisation of about 0.6 %.

Next, we applied the same protocol on other types of graphene, namely CVD-graphene (^{CVD}G, I_D/I_G = 0.1, L_D = 34.8 nm) and graphene derived from oxo-*G, which we prepared by wet-chemical exfoliation of graphite sulfate (*G, I_D/I_G = 1.10, L_D = 10.8 nm). These materials bear significantly less vacancy defects than ^{S}G. However, after functionalisation we detected a negligible evolution of the D-mode using ^{CVD}G even after 5 hours at 80 °C (I_D/I_G = 0.2), and a minor change of the I_D/I_G ratio from 1.10 to 1.45 using *G. Assuming a homogeneous functionalisation of the π-system with a degree of functionalisation similar to ^{S}G, one would expect more

prominent variations in the corresponding I_D/I_G ratios for ^{CVD}G and *G. Since all used materials are 99 % similar and differ just in their density of vacancy defects, it seems that most areas of the π-system are unreactive and functionalisation is favoured next to defect sites. Thus, we also used *^{T}G in addition to ^{S}G, *G and ^{CVD}G, which was derived from *G, but possesses a density of vacancy defects comparable to ^{S}G. Analysis of this material by SRS before (I_D/I_G = 2.7, L_D = 2.0 nm) and after (I_D/I_G = 1.6, L_D = 1.4 nm) functionalisation confirms our conjecture as the reactivity of *^{T}G is comparable to ^{S}G.

We considered the model on Raman spectroscopy of graphene introduced by Lucchese *et al.* and Cançado *et al.*, which support our experimental results: an in-plane vacancy defect acts as a scattering point in the Raman process and activates the surrounding area up to a certain distance, which contributes to the D-mode evolution. Further functionalisation close to the initial defect would now induces Raman scattering in the already-activated area. Consequently, Raman spectra should not vary in a significant way, since this assumption results in a slightly reduced distance between two defects although many moieties were introduced. We attached six moieties to the graphene lattice next to initial point defects at a distance of 2.0 nm and 10 nm. In the first case, L_D decreases from 2.0 nm to 1.4 nm after functionalisation and thus, a change of the I_D/I_G from 2.8 to 1.3 can be expected. In the latter case, the decrease of the L_D from 10 nm to 9.4 nm would change the I_D/I_G ratio from 1.2 to 1.3 (*cf.* **figure 9B**, Ch. 5.2). This consideration is almost congruent with our experimental observations for the functionalisation of ^{S}G and *G. We conclude, that only activated sites in proximity to defects are functionalised by ArN_2Boc. Thus, the final degree of functionalization can be controlled *via* the reaction time, reaction temperature and strongly limited by the density of vacancy defects.

7. Publications: Major Contributions

7.1. Effect of friction on oxidative graphite intercalation and high-quality graphene formation

Authors	S. Seiler, C. E. Halbig, F. Grote, P. Rietsch, F. Börnert, U. Kaiser, B. Meyer, S. Eigler
Journal	Nat. Commun.**2018**, *9* (1), 836
DOI	10.1038/s41467-018-03211-1
Links	https://doi.org/10.1038/s41467-018-03211-1 https://www.nature.com/articles/s41467-018-03211-1
Detailed scientific contribution	The concept of this manuscript was elaborated by S. Seiler, C. E. Halbig, Prof. Dr. B. Meyer and Prof. Dr. S. Eigler. Synthesis of the graphite intercalation compounds and thereout derived oxo-G was conducted mainly by C. E. Halbig. F. Grote and P. Rietsch assisted during the preparation. Obtained GICs were examined by optical microscopy and SRS by C. E. Halbig. UV-vis was measured by C. E. Halbig and F. Grote. F. Grote prepared LB films of oxo-G and analysed the film by AFM. HR-TEM images were recorded by Dr. F. Börnert. All theoretical calculations were implemented by S. Seiler. Prof. Dr. B. Meyer, Prof. Dr. S. Eigler and Prof. Dr. U. Kaiser supervised the authors. The manuscript was mainly written by S. Seiler, C. E. Halbig with assistance from Prof. Dr. S. Eigler and Prof. Dr. B. Meyer.
Estimated own contribution	~ 40 %

7.2. Quantitative Investigation of the Fragmentation Process and Defect Density Evolution of Oxo-functionalized Graphene Due to Ultrasonication and Milling

Authors	C. E. Halbig, T. J. Nacken, J. Walter, C. Damm, S. Eigler, W. Peukert
Journal	Carbon **2016**, *96* (14), 897-903
DOI	10.1016/j.carbon.2015.10.021
Links	https://doi.org/10.1016/j.carbon.2015.10.021 https://www.sciencedirect.com/science/article/pii/S000862231530347X?via%3Dihub
Detailed scientific contribution	The concept of this manuscript was elaborated by T. J. Nacken, C. E. Halbig and Prof. Dr. S. Eigler and Prof. Dr. W. Peukert. Synthesis of the initially used oxo-G nanoparticles, exclusively monolayers, and ultrasound fragmentation was conducted by C. E. Halbig, ball milling was conducted by T. J. Nacken. Both analysed their samples individually by UV-vis, Zeta-Potential and SRS. J. Walter and T. J. Nacken determined the obtained particle sizes after fragmentation by AUC, whereas C. E. Halbig recorded AFM images. Dr. C. Damm, Prof. Dr. S. Eigler and Prof. Dr. W. Peukert supervised the authors. The manuscript was mainly written by C. E. Halbig and T. J. Nacken with assistance from the supervisors.
Estimated own contribution	~ 50 %

7.3. Structural Factors Controlling Size Reduction of Graphene Oxide in Liquid Processing

Authors	T. J. Nacken, C. E. Halbig, S. Wawra, C. Damm, S. Romeis, J. Walter, M. J. Tehrani, Y. Ishii, S. Eigler, W. Peukert
Journal	Carbon **2017**, *125*, 360-369
DOI	10.1016/j.carbon.2017.09.066
Links	https://doi.org/10.1016/j.carbon.2017.09.066 https://www.sciencedirect.com/science/article/pii/S0008622317309429?via%3Dihub
Detailed scientific contribution	The concept of this manuscript was elaborated by T. J. Nacken, C. E. Halbig and Prof. Dr. S. Eigler and Prof. Dr. W. Peukert. Oxo-G nanoparticles and thereout derived derivatives were synthesised by C. E. Halbig. Fragmentation experiments, UV-vis spectroscopy, Zeta-Potential and SRS were conducted by T. J. Nacken and S. Wawra. Particle sizes were analysed with AUC by S. Wawra and J. Walter. ^{13}C-SSNMR spectra were recorded by M. J. Tehrani and Y. Hu. Characterisation by TGA and TGA-MS was performed by C. E. Halbig. Dr. C. Damm, S. Romeis, Prof. Dr. Y. Ishii, Prof. Dr. S. Eigler and Prof. Dr. W. Peukert supervised the authors. The manuscript was mainly written by T. J. Nacken, C. E. Halbig and S. Wawra with assistance from their supervisors.
Estimated own contribution	~ 35 %

7.4. Oxo-Functionalized Graphene as Cell Membrane Carrier of Nucleic Acid Probes Controlled by Aging

Authors	H. Pieper, C. E. Halbig, L. Kovbasyuk, M. R. Filipovic, S. Eigler, A. Mokhir
Journal	Chem. Eur. J. **2016**, *22* (43), 15389-15395
DOI	10.1002/chem.201603063
Links	https://doi.org/10.1002/chem.201802500 https://onlinelibrary.wiley.com/doi/full/10.1002/chem.201802500
Detailed scientific contribution	The concept of this manuscript was elaborated by C. E. Halbig, H. Pieper, Prof. Dr. S. Eigler and Prof. Dr. A. Mokhir. Oxo-G nanoparticles were synthesised and characterised by FT-IR, TGA-MS, statistical Raman spectroscopy and UV-vis by C. E. Halbig. H. Pieper synthesised and characterised the functional oligonucleotides and recorded cell images as well as all fluorescence spectra. Prof. Dr. S. Eigler and Prof. Dr. A. Mokhir supervised the authors. The manuscript was written by C. E. Halbig, Prof. Dr. S. Eigler and Prof. Dr. A. Mokhir.
Estimated own contribution	~ 40 %

7.5. Towards the Synthesis of Graphene Azide from Graphene Oxide

Authors	C. E. Halbig, P. Rietsch, S. Eigler
Journal	Molecules **2015**, *20* (12), 21050-21057
DOI	10.3390/molecules201219747
Links	https://doi.org/10.3390/molecules201219747 https://www.mdpi.com/1420-3049/20/12/19747
Detailed scientific contribution	The concept of this manuscript was elaborated by C. E. Halbig and Prof. Dr. S. Eigler Oxo-G and azide functionalised oxo-G nanoparticles were synthesised by C. E. Halbig. All experimental data were collected by C. E. Halbig. P. Rietsch assisted the experimental work. The manuscript was written by C. E. Halbig and Prof. D. S. Eigler.
Estimated own contribution	~ 90 %

7.6. Oxo-Functionalized Graphene - A Versatile Precursor for Alkylated Graphene Sheets by Reductive Functionalization

Authors	C. E. Halbig, O. Martin, F. Hauke, S. EIgler, A. Hirsch
Journal	Chem. Eur. J. **2018,** *24,* 13348-13354
DOI	10.1002/chem.201802500
Links	https://doi.org/10.1002/chem.201802500 https://onlinelibrary.wiley.com/doi/full/10.1002/chem.201802500
Detailed scientific contribution	The concept of this manuscript was elaborated by C. E. Halbig, O. Martin, Dr. F. Hauke and Prof. Dr. S. Eigler. Oxo-G nanoparticles and thereout chemically exfoliated and stabilised graphene (G/SCH) was synthesised by C. E. Halbig. Reductive functionalisation of graphene was performed by O. Martin and C. E. Halbig. AFM, and UV-vis was performed by C. E. Halbig. SRS and TGA-MS was performed by C. E. Halbig and O. Martin, temperature dependent Raman spectroscopy and TGA-GC/MS by O. Martin. Both evaluated the recorded data equally. Dr. F. Hauke, Prof. Dr. A. Hirsch and Prof. Dr. S. Eigler supervised theoretical and experimental work. The manuscript was mainly written by C. E. Halbig, Prof. Dr. S. Eigler and O. Martin.
Estimated own contribution	~ 50 %

7.7 Selective functionalization of graphene at defect activated sites by arylazocarboxylic *tert*-butyl esters

Authors	C. E. Halbig, R. Lasch, J. Krüll, A. Pirzer, M. R. Heinrich, S. Eigler
Journal	submitted to Angewandte Chemie, **09/2018**
DOI	n/a
Detailed scientific contribution	The concept of this manuscript was elaborated by C. E. Halbig, Prof. Dr. S. Eigler and Prof. Dr. M. R. Heinrich. Four arylazocarboxylic *tert*-butyl ester derivatives (ArN_2Boc) with different substituents were synthesised and characterised by J. Krüll, A. Pirzer and R. Lasch. C. E. Halbig synthesised and fully characterised all derivatives of oxo-G. C. E. Halbig functionalised the obtained materials using ArN2Boc and evaluated the obtained data (SRS and TGA-MS). Prof. Dr. S. Eigler and Prof. Dr. M. Heinrich supervised the authors. The manuscript was mainly written by C. E. Halbig and Prof. Dr. S. Eigler.
Estimated own contribution	~ 80 %

Selective functionalization of graphene at defect activated sites by arylazocarboxylic *tert*-butylesters

Christian E. Halbig,[a] Roman Lasch,[b] Jasmin Krüll,[b] Anna Pirzer,[b] Zhenping Wang,[a] Jan N. Kirchhof,[c] Kirill I. Bolotin,[c] Markus R. Heinrich*[b] and Siegfried Eigler*[a]

[a] Christian Eberhard Halbig, Zhenping Wang and Siegfried Eigler
Institut für Chemie und Biochemie, Freie Universität Berlin
Takustraße 3, 14195 Berlin, Germany
E-mail: siegfried.eigler@fu-berlin.de

[b] Roman Lasch, Jasmin Krüll, Anna Pirzer and Markus R. Heinrich Department Chemie und Pharmazie,
Friedrich-Alexander Universität Erlangen-Nürnberg
Nikolaus-Fiebiger-Straße 10, 91058 Erlangen, Germany
E-Mail: markus.heinrich@fau.de

[c] Jan Niklas Kirchhof, Kirill I. Bolotin,
Institut für Experimentalphysik, Freie Universität Berlin
Arnimallee 14, 14195 Berlin, Germany

Abstract: The development of versatile functionalization concepts for graphene are currently in the focus of research. With oxo-functionalization of graphite the full surface of graphene becomes accessible for C-C bond formation to introduce out-of-plane functionality. Here we present the arylation of graphene by arylazocarboxylic *tert*-butylesters, which generates aryl radicals after activation by acids. Surprisingly, the degree of functionalization is related to the concentration of lattice vacancy defects of graphene. Consequently, graphene, which is free from lattice defects is not reactive. The reaction can be applied to graphene dispersed in solvents and leads to bitopic functionalization, as well as monotopic functionalization if graphene is deposited on surfaces. Since the arylazocarboxylic *tert*-butylester moiety can be attached to various molecules, the presented method paves the way to functional graphene derivatives with the density of defects determining the degree of functionalization.

Introduction

Graphene (G) is a nanomaterial that allows chemical functionalization of its surface, either monotopic on surfaces or bitopic in solution.[1] The surface area of ~2600 m^2/g,[2] and mechanical strength[3] combined with high charge carrier mobility[4] make graphene an attractive material for applications, such as printed devices, solar cells, molecular carrier systems, membranes, or composites.[5] Chemical functionalization of graphene expands the functionality and it was demonstrated that selective sensing becomes possible.[6] Our previous discovery of the controlled oxidative functionalization of graphite and delamination of oxo-functionalized graphene (oxo-G) gave access to wet-chemically prepared graphene and established a dispersible source for studying the chemistry of graphene.[7] Our method, which avoids extended over-oxidation, overcomes the hurdles accompanied with the protocol introduced by Hummers' and Offenman's, which is widely used in literature (**figure S1**). The lattice defect concentration of oxo-G can thereby be adjusted between 0.02% and about 1% and probed by statistical Raman spectroscopy and transmission electron microscopy at atomic resolution.[7c, 8]

Graphene placed on substrates allows monotopic wet-chemical functionalization, whereas suspended graphene allows bitopic functionalization.[1c, 9] Up to now, stable C-C bond formation is reported by charging graphite or graphene negatively followed by functionalization by electrophiles or by neutral routes.[1e, 10] Moreover, the arylation of graphene is highly efficient using diazonium salts. The reaction proceeds *via* electron transfer from graphene to the diazonium salt to generate radicals prior to the formation of C-C bonds. However, the few-layer

contamination remains problematic for this approach. Up to now the research mainly focused on finding highly efficient reactions towards graphene. However, it can be assumed that in-plane lattice defects activate the surrounding carbon bonds in a way that selective functionalization of those becomes possible.[11]

Here we present a novel and universal functionalization strategy for monotopic and bitopic functionalization of graphene directed by defect-sites. Radical species are generated from the decomposition of arylazocarboxylic acid *tert*-butylesters (ArN_2Boc, **scheme 1**).[12] The radicals react in defect-activated areas of graphene forming C-C bonds. Such a selective functionalization directed by defects is unique. A further advantage of ArN_2Boc over common diazonium salts is the enhanced chemical stability and the formation of the desired aryl radical does not require a single electron transfer from graphene but activation by acids.[12c, 13]

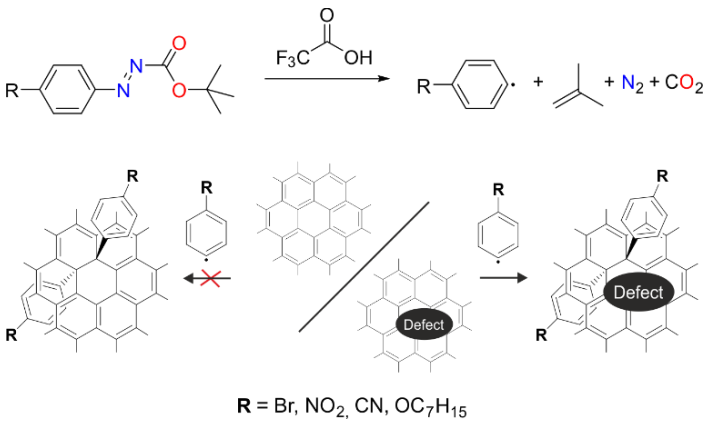

Scheme 1: Chemical sketch of generation of aryl radicals from arylazocarboxylic *tert*-butylesters in the presence of trifluoroacetic acid (top), and the subsequent functionalization of the carbon lattice of graphene next to defect sites (bottom). Graphene stabilized in solution or deposited on SiO_2-substrate can be used.

Results and Discussion

For investigating the reactivity of graphene directed by in-plane lattice defects, we prepared a series of graphene derivatives, first to investigate the monotopic functionalization on a SiO_2 surface. Based on our previous research, we used two types of oxo-functionalized graphene as precursors for this study, the standard oxo-G, which possesses 0.5% of in-plane lattice defects (oxo-^{S}G) and oxo-G with 0.02% of in-plane lattice defects (oxo-*G).[7a, 7c, 14] Both samples were deposited onto Si/300 nm SiO_2 wafers and subsequently chemically reduced to graphene with densities of defects of 0.5% (^{S}G) and 0.02% (*G), respectively.[15] In addition, graphene prepared by chemical vapor deposition with approximately 0.002% of lattice defects was used. Moreover, oxo-*G was thermally processed at 200 °C to generate additional in-plane lattice defect of about 0.7%.[14] The details for the synthetic protocols and the characterization are given in the supplementary information.

Subsequently, ^{S}G was reacted with four derivatives of ArN_2Boc and the successful reaction could be monitored by Raman spectroscopy (**figure 1, S2-5**). The reaction can be monitored by following the change of the intensity ratio of the D- and G-mode (I_D/I_G) using statistical Raman spectroscopy, a method, which we described before.[16] The spectroscopic changes saturate after about 120 min, indicating the end of the reaction. While we find significant changes of the I_D/I_G ratio for ^{S}G, which possesses 0.5% of defects, the change of the I_D/I_G ratio for *G with only 0.02% of lattice defects is less pronounced and differs from that found for ^{S}G. For ^{CVD}G with 0.002% of defects we saw almost no changes in the spectra (**figure 1D**). Thus, in addition to ^{S}G *G and ^{CVD}G we also used ^{*T}G, which was derived from *G but possesses a comparable density of defects as ^{S}G. Indeed, the reactivity of ^{*T}G is similar to that found for ^{S}G (**figure 1D, S8C**). Those results indicate that the reaction of aryl radicals generated from ArN_2Boc is directed by defects and intact graphene is not reactive.

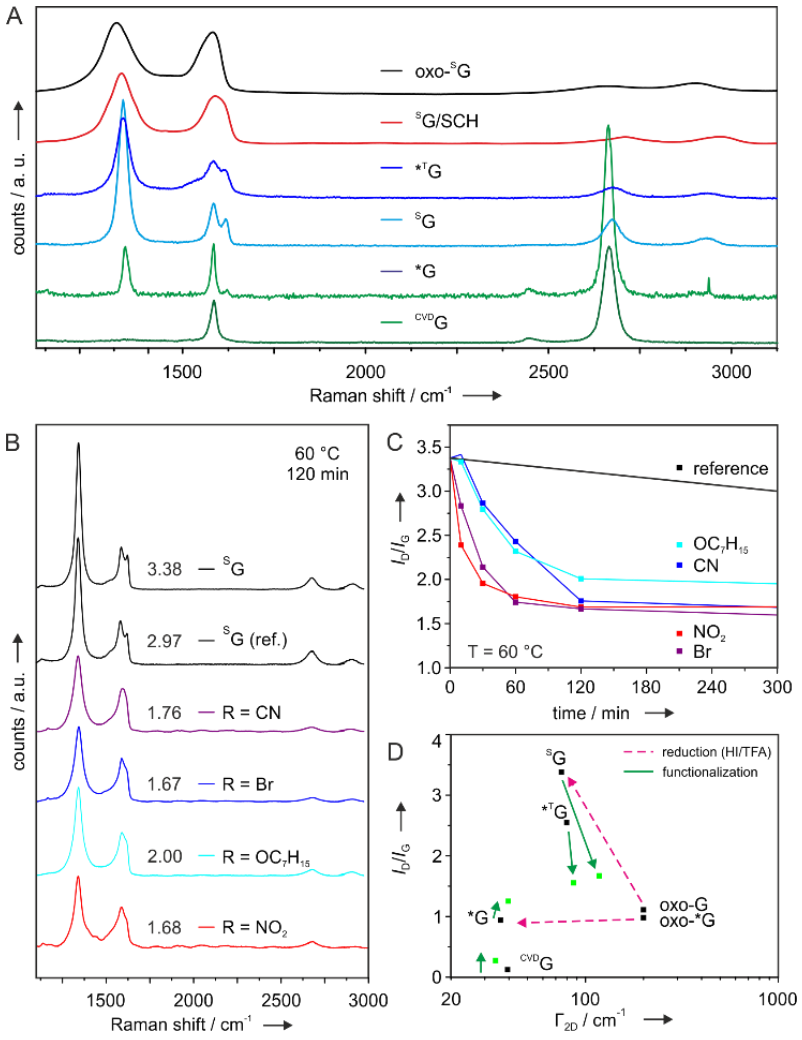

Figure 15. (A) Raman spectra of all prepared graphene samples used in our experiments. (B) Average spectra of initial ^{S}G before and after functionalization for 120 minutes at 60°C. A reference for the reaction under similar conditions but without any ArN_2Boc is indicated by "ref." in brackets. (C) Plot of the evolution of the I_D/I_G ratio over the reaction time for ^{S}G functionalized by all four used ArN_2Boc samples at 60 °C. (D) Changes in the mean Raman spectra before and after functionalization of all used graphene samples for the reaction with 4-Br-ArN_2Boc at 60°C. A dotted arrow indicates the reduction of oxo-G and oxo-*G, respectively, by hot HI/TFA, whereas a green arrows indicates changes due to the functionalization process.

compound	I_D/I_G (initial)	L_D (nm)	Θ (%)	* I_D/I_G (120 min,60 °C)	* L_D (nm)
oxo-^{S}G	1.11±0.04	<< 1	> 50	-	-
oxo-*G	0.98	<< 1	~ 4	-	-
^{S}G/SCH	1.98	1.7	0.9	-	-
*^{T}G	2.70	2.0	0.7	1.56	1.4
^{S}G	3.38±0.45	2.3	0.5	1.67	1.6
*G (average)	1.10	10.8	0.02	1.49	9.1
^{CVD}G	0.12	34.8	0.002	0.20	26.8

Table 4: Overview of the evaluated spectra obtained by (statistical) Raman spectroscopy (I_D/I_G and L_D) for all synthesized graphene-based compounds on 300 nm SiO_2/Si surfaces before (left) and after functionalization for 120 minutes at 60 °C (right, indicated with asterisk).

Considerations about the model on Raman spectroscopy of graphene support the experimental results. The relation of the I_D/I_G ratio and full-width at half-maximum of the main Raman modes to the distance of defects (L_D), and consequently density of defects ϑ, is based on the model introduced by Lucchese *et al.* and Cançado *et al.* and found experimental plausible in various studies.[7b, 16b, 17] As illustrated in **figure 2A** an in-plane vacancy defect acts as a scattering point in the Raman process and activates a certain area next to the defect. A subsequent reaction, such as C-C bond formation in the activated area will consequently further disturb the Raman process and induce scattering already close to the initial defects (**figure 2B**). This assumption results in a reduced L_D distance between defects, as illustrated in **figure 2C**. Accordingly, it can be derived that an initial L_D of 2.0 nm would lead to a reduced L_D of 1.4 nm. Such a change of L_D can significantly be monitored by statistical Raman microscopy since the I_D/I_G ratio is expected to change from about 2.8 to 1.3. Experimentally, we observe this trend and the I_D/I_G ratio changes from 3.4 to 1.7 for ^{S}G and 2.7 to 1.6 for ^{T*}G, respectively. Since Raman spectroscopy is most sensitive for densities at around 0.5%, those results are in good agreement with the model. Assuming the C-C bond reaction for graphene with L_D of 10 nm, it is expected that L_D is reduced to about 9.4 nm, as illustrated in **figure 2C**. This change of L_D is related to the change of the I_D/I_G ratio from 1.3 to 1.4. For *G the calculated L_D is about 10.8 nm and we find experimentally that the I_D/I_G ratio changes from 1.1 to 1.5, which indicates a decrease of L_D to 9.1 nm. This experiment clearly demonstrates that most of the graphene surface is not reactive. Finally, the reaction was conducted with ^{CVD}G and almost no change of the Raman spectra was found. The calculated change of the I_D/I_G ratio from 0.12 to 0.20 indicates only little changes in nm-scale. However, since the origin of the D-mode in ^{CVD}G originates largely from grain boundaries the observed change of the I_D/I_G ratio may originate from the reaction close to grain boundaries.[18]

The investigations for the monotopic functionalization activated by lattice defects can best be monitored using graphene with L_D of about 2 nm, which relates to a density of defects of about 0.5%, respectively. ^{S}G, fulfills the requirements and is obtained from aqueous oxo-^{S}G using sodium borohydride as a reducing agent in the presence of sodium cholate acting as a surfactant (^{S}G/SCH). This material bears slightly more lattice defective than ^{S}G on surfaces due to the different method of reduction.[10c, 19] As the preparation of large amounts of functionalized graphene is highly desired in any point of application, we investigated the reactivity of ^{S}G/SCH towards four different 4-R-ArN_2Boc derivatives (R = -Br, -CN, -NO_2 and -OC_7H_{15}) and analyzed the obtained and purified products by TGA-MS. The results were compared to the functionalization with 4-bromobenzene diazonium tetra-fluoroborate (4-Br-ArN_2^+ BF_4^-). After mixing the reaction partners in acetonitrile and water, all dispersions tend to agglomerate due to competitive non-covalent interactions between the arylation agent and sodium cholate with graphene. However, the adsorbed ArN_2Boc derivatives were then activated with 1M trifluoroacetic acid (TFA) and heated to 60 °C to induce the functionalization of ^{S}G/SCH. The reaction protocol is similar to the route for monotopic functionalization outlined above.

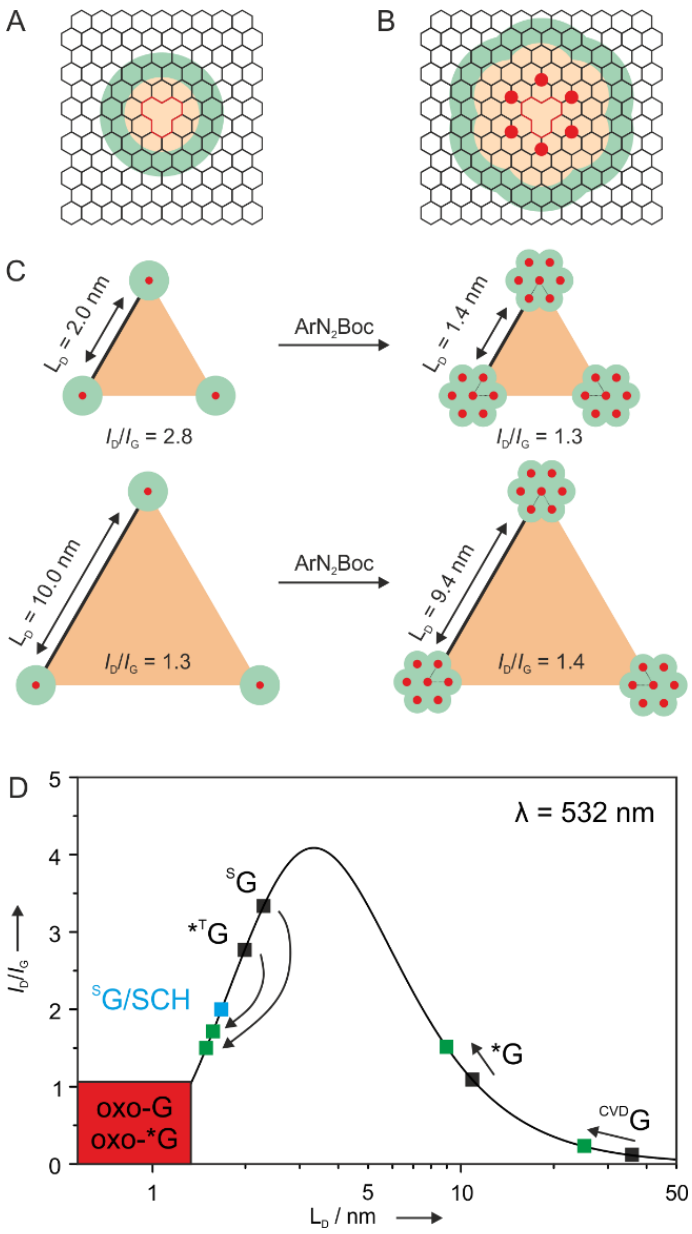

Figure 16. (A) A single vacancy defect in the graphene lattice and (B) the same with five additionally introduced (functional) defects in proximity to the vacancy. A brown circle indicates the structurally disturbed area whereas a green circle highlights the activated region. (C) L_D and estimated I_D/I_G ratio defects for two differently sized triangular defect constellations elucidating the changes of L_D and I_D/I_G ratio after the functionalization using ArN_2Boc. (D) Plot of the I_D/I_G over L_D for our prepared graphene samples before and after functionalization according to the literature.[16b, 17a]

Analysis of the purified and freeze-dried products gave evidence for covalently attached aryl moieties on the surface of ^{S}G/SCH as visible in the TGA-MS data (**figure 3A**)**.** The addends are cleaved in the temperature region between 250 °C and 350 °C and can be identified by the m/z traces 77 ($C_6H_5^+$). For 4-Br-ArN_2Boc m/z of 156 and 158 can be detected corresponding to the fragment $BrC_6H_5^+$ with its two naturally occurring and stable bromine isotopes ^{79}Br and ^{81}Br. Traces in the lower temperature region from 125 °C to 250 °C were assigned to physisorbed species since adsorbed molecules are weaker bound than covalently attached species. The same result could be reproduced after functionalization of ^{S}G/SCH with aqueous 4-Br-ArN_2^+ BF_4 (**figure 3B**). In the case of 4-R-ArN_2Boc, the attendant mass fragments can be detected, two peaks for adsorbed and covalently bound benzonitrile moieties with their similar m/z 103 (NC-$C_6H_5^+$) appear in addition to traces of m/z 77. Additionally, there is an intense signal for m/z 26, which we refer to cleaved C≡N^+ ions from the corresponding phenyl moieties. Similar to this, functionalization with 4-NO_2-ArN_2Boc results in two overlapping signals in the range 125 °C to 350 °C for m/z values of 77 and 123 ($C_6H_5^+$). For the used *n*-heptyloxy-derivative, we find m/z 77 and m/z 65 ($C_5H_5^+$), where the latter is a degradation product of cleaved and ionized phenol like structures. A complete overview of all TGA-MS measurements is given in the supplementary (**figure S9-10).**

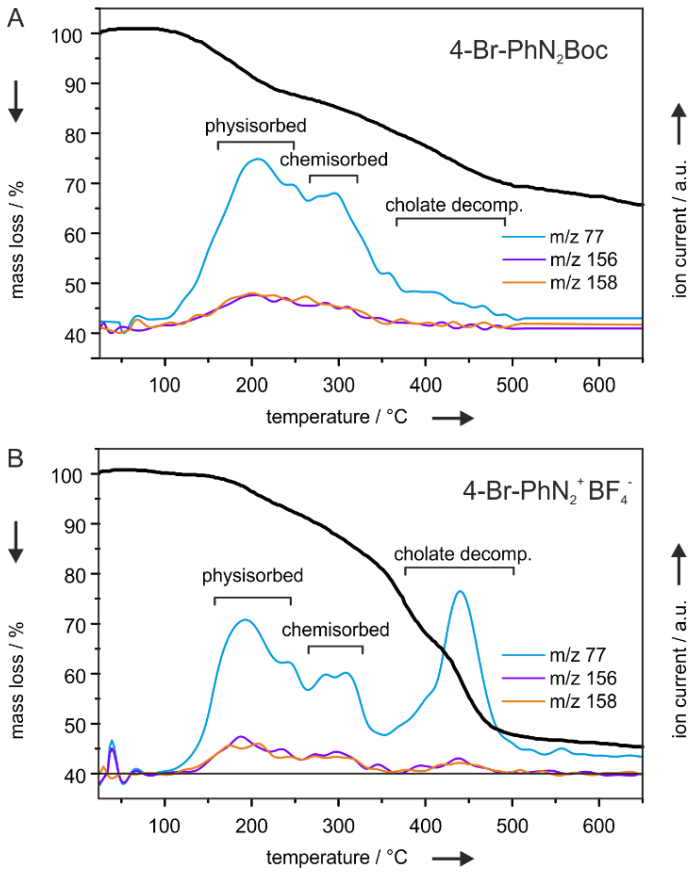

Figure 3. (A) TGA-MS of G/SCH reacted with 4-BrArN_2Boc and (B) 4-bromobenzene diazonium tetrafluoroborate (4-Br-PhN_2^+ BF_4^-) as a reference for the arylation of graphene.

Conclusions

The statistical distributed density of lattice vacancy defects in graphene can be controlled over a wide range from about 0.02% to 1%. Thus, it was appealing to find a functionalization method that is selective for activated π-systems and keeps the non-activated graphene lattice pristine. Arylazocarboxylic *tert*-butylesters are used here to generate aryl radicals. Those radicals are generated slowly that the reactivity of surface deposited graphene reacts within 2 h. Raman spectroscopy is highly sensitive towards the distance between scattering points, such as vacancy defects and vacancy defects extended by functionalization defects, respectively, in particular for L_D between 2–10 nm. Using this methodology allows to conclude on a reduced L_D after aryl-functionalization generated by arylazocarboxylic *tert*-butylesters. Consequently, we can explain why pristine graphene is not reactive. Thus, graphene activated by vacancy defects with L_D of about 2-3 nm leads to functionalized graphene with a regioselectivity close to vacancy defects. This type of graphene could be synthesized from oxo-functionalized graphene by chemical reduction and stabilization by sodium cholate, to be arylated bitopic in dispersion. It was further shown that the functionalization reaction depends on the activity of the derivative of arylazocarboxylic *tert*-butylesters. The successful functionalization could be evaluated by thermogravimetric analysis. The arylazocarboxylic *tert*-butylester group is chemically versatile and can be attached to a broad variety of molecules as a reactive moiety. The here presented method is unique and will pave the way towards novel graphene derivatives to be used e.g. for selective sensing.

Acknowledgements

This research was funded by the Deutsche Forschungs-gemeinschaft (DFG, German Research Foundation, project numbers 392444269 and HE5413/3-3). We thank the SFB 953 at Friedrich-Alexander-University of Erlangen-Nürnberg for the support with TGA-MS equipment.

Keywords: Graphene • Graphene Oxide • oxo-G • Arylation • functionalization • TGA-MS • statistical Raman spectroscopy

References

[1] a) D. R. Dreyer, S. Park, C. W. Bielawski, R. S. Ruoff, *Chem. Soc. Rev.* **2010**, *39*, 228; b) S. Eigler, A. Hirsch, *Angew. Chem. Int. Ed.* **2014**, *53*, 7720; c) J. M. Englert, K. C. Knirsch, C. Dotzer, B. Butz, F. Hauke, E. Spiecker, A. Hirsch, *Chem. Commun.* **2012**, *48*, 5025; d) Y. Si, E. T. Samulski, *Nano Lett.* **2008**, *8*, 1679; e) J. M. Englert, C. Dotzer, G. Yang, M. Schmid, C. Papp, J. M. Gottfried, H. P. Steinruck, E. Spiecker, F. Hauke, A. Hirsch, *Nat. Chem.* **2011**, *3*, 279.

[2] F. Bonaccorso, L. Colombo, G. Yu, M. Stoller, V. Tozzini, A. C. Ferrari, R. S. Ruoff, V. Pellegrini, *Science* **2015**, *347*, 1246501.

[3] a) C. Lee, X. Wei, J. W. Kysar, J. Hone, *Science* **2008**, *321*, 385; b) C. Gomez-Navarro, M. Burghard, K. Kern, *Nano Lett.* **2008**, *8*, 2045.

[4] a) S. V. Morozov, K. S. Novoselov, M. I. Katsnelson, F. Schedin, D. C. Elias, J. A. Jaszczak, A. K. Geim, *Phys. Rev. Lett.* **2008**, *100*, 016602; b) E. V. Castro, K. S. Novoselov, S. V. Morozov, N. M. Peres, J. M. dos Santos, J. Nilsson, F. Guinea, A. K. Geim, A. H. Neto, *Phys. Rev. Lett.* **2007**, *99*, 216802.

[5] a) M. H. Overgaard, M. Kühnel, R. Hvidsten, S. V. Petersen, T. Vosch, K. Nørgaard, B. W. Laursen, *Adv. Mater. Technol.* **2017**, *2*, 1700011; b) H. Chen, Y. Hou, C. E. Halbig, S. Chen, H. Zhang, N. Li, F. Guo, X. Tang, N. Gasparini, I. Levchuk, S. Kahmann, C. O. Ramirez Quiroz, A. Osvet, S. Eigler, C. J. Brabec, *J. Mater. Chem. A* **2016**, *4*, 11604; c) J. Liu, L. Cui, D. Losic, *Acta Biomater.* **2013**, *9*, 9243; d) S. Homaeigohar, M. Elbahri, *Npg Asia Mater.* **2017**, *9*; e) T. Kuilla, S. Bhadra, D. Yao, N. H. Kim, S. Bose, J. H. Lee, *Prog. Polym. Sci.* **2010**, *35*, 1350.

[6] a) B. Alfano, E. Massera, T. Polichetti, M. L. Miglietta, G. Di Francia, *Sensors and Actuators B: Chemical* **2017**, *253*, 1163; b) D. Chen, H. Feng, J. Li, *Chem. Rev.* **2012**, *112*, 6027; c) K. u. Hasan, M. H. Asif, *J. Biosensors & Bioelectronics* **2012**, *03*.

[7] a) S. Eigler, *Chem. Commun.* **2015**, *51*, 3162; b) S. Eigler, M. Enzelberger-Heim, S. Grimm, P. Hofmann, W. Kroener, A. Geworski, C. Dotzer, M. Rockert, J. Xiao, C. Papp, O. Lytken, H. P. Steinruck, P. Muller, A. Hirsch, *Adv. Mater.* **2013**, *25*, 3583; c) B. Butz, C. Dolle, C. E. Halbig, E. Spiecker, S. Eigler, *Angew. Chem. Int. Ed.* **2016**, *55*, 15771.

[8] a) P. Feicht, S. Eigler, *ChemNanoMat* **2018**, *4*, 244; b) S. Seiler, C. E. Halbig, F. Grote, P. Rietsch, F. Borrnert, U. Kaiser, B. Meyer, S. Eigler, *Nat. Commun.* **2018**, *9*, 836.

[9] K. C. Knirsch, R. A. Schafer, F. Hauke, A. Hirsch, *Angew. Chem. Int. Ed.* **2016**, *55*, 5861.

[10] a) G. Abellan, M. Schirowski, K. F. Edelthalhammer, M. Fickert, K. Werbach, H. Peterlik, F. Hauke, A. Hirsch, *J. Am. Chem. Soc.* **2017**, *139*, 5175; b) J. Greenwood, T. H. Phan, Y. Fujita, Z. Li, O. Ivasenko, W. Vanderlinden, H. Van Gorp, W. Frederickx, G. Lu, K. Tahara, Y. Tobe, I. H. Uji, S. F. Mertens, S. De Feyter, *ACS Nano* **2015**, *9*, 5520; c) C. E. Halbig, O. Martin, F. Hauke, S. Eigler, A. Hirsch, *Chem. Eur. J.* **2018**.

[11] J. Holzwarth, K. Y. Amsharov, D. I. Sharapa, D. Reger, K. Roshchyna, D. Lungerich, N. Jux, F. Hauke, T. Clark, A. Hirsch, *Angew. Chem. Int. Ed.* **2017**, *56*, 12184.

[12] a) S. K. Fehler, G. Pratsch, M. R. Heinrich, *Angew. Chem.* **2014**, *126*, 11543; b) S. B. Höfling, A. L. Bartuschat, M. R. Heinrich, *Angew. Chem.* **2010**, *122*, 9963; c) H. Jasch, S. B. Hofling, M. R. Heinrich, *J. Org. Chem.* **2012**, *77*, 1520; d) N. Nebel, B. Strauch, S. Maschauer, R. Lasch, H. Rampp, S. K. Fehler, L. R. Bock, H. Hubner, P. Gmeiner, M. R. Heinrich, O. Prante, *ACS Omega* **2017**, *2*, 8649.

[13] G. L. Paulus, Q. H. Wang, M. S. Strano, *Acc. Chem. Res.* **2013**, *46*, 160.

[14] F. Grote, C. Gruber, F. Borrnert, U. Kaiser, S. Eigler, *Angew. Chem. Int. Ed.* **2017**, *56*, 9222.

[15] S. Eigler, S. Grimm, M. Enzelberger-Heim, P. Muller, A. Hirsch, *Chem. Commun.* **2013**, *49*, 7391.
[16] a) S. Eigler, C. Dotzer, A. Hirsch, *Carbon* **2012**, *50*, 3666; b) M. M. Lucchese, F. Stavale, E. H. M. Ferreira, C. Vilani, M. V. O. Moutinho, R. B. Capaz, C. A. Achete, A. Jorio, *Carbon* **2010**, *48*, 1592.
[17] a) L. G. Cancado, A. Jorio, E. H. Ferreira, F. Stavale, C. A. Achete, R. B. Capaz, M. V. Moutinho, A. Lombardo, T. S. Kulmala, A. C. Ferrari, *Nano Lett.* **2011**, *11*, 3190; b) P. Vecera, S. Eigler, M. Kolesnik-Gray, V. Krstic, A. Vierck, J. Maultzsch, R. A. Schafer, F. Hauke, A. Hirsch, *Sci. Rep.* **2017**, *7*, 45165.
[18] L. Gustavo Cançado, M. Gomes da Silva, E. H. Martins Ferreira, F. Hof, K. Kampioti, K. Huang, A. Pénicaud, C. Alberto Achete, R. B. Capaz, A. Jorio, *2D Mater.* **2017**, *4*, 025039.
[19] a) S. Eigler, S. Grimm, F. Hof, A. Hirsch, *J. Mater. Chem. A* **2013**, *1*, 11559; b) T. J. Nacken, C. E. Halbig, S. E. Wawra, C. Damm, S. Romeis, J. Walter, M. J. Tehrani, Y. C. Hu, Y. Ishii, S. Eigler, W. Peukert, *Carbon* **2017**, *125*, 360.

SUPPORTING INFORMATION

Selective functionalization of graphene at defect activated sites by arylazocarboxylic *tert*-butylesters

Christian E. Halbig,[a] Roman Lasch,[b] Jasmin Krüll,[b] Anna Pirzer,[b] Zhenping Wang,[a] Jan N. Kirchhof,[c] Kirill I. Bolotin,[c] Markus R. Heinrich*[b] and Siegfried Eigler*[a]

[a] Christian Eberhard Halbig, Zhenping Wang and Siegfried Eigler
Institut für Chemie und Biochemie, Freie Universität Berlin
Takustraße 3, 14195 Berlin, Germany
E-mail: siegfried.eigler@fu-berlin.de

[b] Roman Lasch, Jasmin Krüll, Anna Pirzer and Markus R. Heinrich Department Chemie und Pharmazie,
Friedrich-Alexander Universität Erlangen-Nürnberg
Nikolaus-Fiebiger-Straße 10, 91058 Erlangen, Germany
E-Mail: markus.heinrich@fau.de

[c] Jan Niklas Kirchhof, Kirill I. Bolotin,
Institut für Experimentalphysik, Freie Universität Berlin
Arnimallee 14, 14195 Berlin, Germany

Experimental Section

Materials and Methods: Double-distilled water from Carl Roth GmbH. All other chemicals were purchase from sigma Aldrich and used as obtained. For SRS, we used a Horiba LabRAM Aramis spectrometer and equipped with a 532 nm laser for excitation combined with 100x magnification lenses. dT-SRS was measured under nitrogen flow using a Horiba LabRAM Aramis combined with a heating chamber. Maps with a sufficient number of spectra suitable for a convincing statistical analysis had been recorded. TGA-MS was performed on a Netzsch STA 409 CD-QMS 403/5 SKIMMER. AFM images were recorded on an NT-MDT Solver Pro equipped with NSG10/Au probes and intermittent contact mode was chosen. For purification of oxo-G we used a Sigma 4K-15 (rotor: 6x200 mL PP beakers).

Synthesis of oxo-^{S}G and ^{S}G: Oxo-functionalized Graphene with a degree of functionalization of about 66% was prepared by stirring 1g of graphite in sulphuric acid (25 mL; 97%) and the addition of 2g $KMnO_4$ over 4 hours as reported in other literature.[1] Then, 20 mL of cold diluted sulphuric acid (over 4 hour) and 100 mL col water (over 16 hour) was added over 4 hour. Finally, the reaction was stopped by the dropwise addition of cold 3% H_2O_2 (over 40 min) and the oxidized crystals were centrifuged for six times until the pH was neutral. After delamination with the help of pulsed tip sonication (20 W; 4 min; 2s on, 2s off), non-monolayer particles were removed by repetitive centrifugation at low RCF and smallest particles by centrifugation at high RPM. The concentration was determined by lyophilisation. The dispersion was stored at 4°C. The concentration of the dispersion was 0.75 mg/mL determined by freeze drying. EA: C: 48.4% H: 3.8% N: 0.0% S: 4.6% O*: 43.2%. G was obtained after reduction of oxo-G by hot hydrogen iodine and trifluoro acetic acid (more details below).

Synthesis of oxo-*G and *G: Oxo-functionalized Graphene with an almost intact carbon lattice and a degree of functionalization of about 4% was prepared as following: 20 g graphite was stirred in sulphuric acid (500 mL; 97%) and 3 mass equivalent $(NH_4)_2S_2O_8$ were added over a period of three days in small portions. After few hours, the graphite changed his color from grey to deep-blue. The reactive mixture was stored for several 4 weeks at ambient conditions. An arbitrary amount of the so formed GIC (approx. 1 g) was taken from the bottle and centrifuged to remove excess of sulfuric acid. Then, the precipitated GIC was frozen at - 24 °C, overlaid with cold water (50 mL, 4 °C) and stored in fridge overnight. The deep-blue color disappeared due to the formation of graphite oxide. The dispersion was centrifuged with water using 50 mL falcon tubes at 14.000 RCF until the pH was neutral. Thus purified graphite oxide was then transferred into a mixture of 50:50 water/methanol and exfoliated by ultrasound for 10 minutes in an ultrasonication bath and finally stored for 16 hours at room temperature. Large particles were removed from the supernatant with following parameters: 4 times, 700 RCF, 5 minutes; 8 times, 1500 RCF, 5 minutes; 4 times 1500 RCF, 7.5 minutes. Smallest fragments were removed from the dispersion by applying 9.000 RCF for 40 minutes for three times, whereas the supernatant was removed. A dark greenish to grey dispersion was obtained containing single layer oxo-G with diameter of about 5 µm next to few-layer oxo-G. *G was obtained after reduction of oxo-*G by hot hydrogen iodine and trifluoro acetic acid (more details below).

Synthesis of ^{S}G/Surfactant: Solid surfactant (sodium dodecylsulfat, sodium dodecylbenzenesulfonat, or sodiumcholate) was added to the obtained and diluted oxo-$G^{50\%}$ dispersion (c = 0.75 mg/mL). The final concentration of the surfactant in the oxo-G dispersion was 4 mg/mL. Then, an excess of 10 mg of sodium borohydride per milligram oxo-G was added to the cold oxo-G dispersion and further stored in refrigerator overnight (4 °C). We obtained a deep black, strongly basic and stable dispersion. At least, the mixture was washed with the corresponding aqueous surfactant (2 mg/mL) by repetitive centrifugation for three times and finally redispersed with pure water.

Deposition and reduction of oxo-G derivatives on SiO_2/Si wafer: Oxo-G^0 or its derivatives were deposited a 300 nm SiO_2/Si wafer by Langmuir-Blodgett technique. First our oxo-G dispersion was diluted with water (~1:10) and then furthermore diluted with 1:1 with of pure methanol. The mixture was dropped on the water-interface in a Langmuir-Blodgett trough and the barriers were compressed until a surface tension of 3 mN/m was reached. After deposition, wafers were placed in 20 mL glass vials filled with glass wool and were reduced by the vapor of HI and TFA for 20 min at 80 °C. Subsequently they were extensively washed with pure water.

Thermal defect introduction into oxo-*G: Oxo-*G was deposited on 300 nm SiO_2/Si wafer (5x5 mm) by drop casting (2.5 µL). After the solvent was evaporated, the wafer was placed in a 50 mL glass vial and filled with argon and annealed for 90 minutes at 200 °C on a heating plate.

Surface assisted functionalization: To achieve functionalization of the graphene derivatives, we prepared solutions of 4-bromophenyldiazonium tetrafluoroborate and all arylazocarboxylate derivatives in 50:50 H2O/MeCN with a concentration of 2 mM. Subsequently, the wafer coated with one of the graphene derivatives was placed in a 5 mL glas vial and 3 mL of the corresponding solution was added in a way, that the complete wafer was covered by the arylation agent. The mixture was activated by the addition of 300 µl trifluoroacetic acid (1 mol/L) and the wafers were incubated for 21°C, 60°C and 80°C for specific reaction times and thereafter carefully rinsed with H_2O/MeCN, THF, H_2O/MeCN and finally pure water. The same procedure was applied for *G.

Bulk functionalization of ^{S}G/Surfactant: 20 mL of aqueous ^{S}G/SCH dispersion was mixed with solid 4 bromobenzenediazonium tetrafluoroborate (100 mg) and stirred overnight. Additionally, 20 mL of the same aqueous ^{S}G/SCH dispersion was mixed with 0.4 mM Arylazocarboxylate dissolved in 8 mL acetonitrile. After 1.5 mL of 1 M trifluoroacetic acid was added, the mixture was heated up to 60 °C for 3 hours while it was vigorously stirred and bubbled with oxygen. All dispersions were centrifuged repeatedly for purification and then freeze-dried overnight. The purification was performed in the following manner: 50:50 H_2O/MeCN (2x), acetonitrile (2x), 50:50 H_2O/MeCN (2x) and finally one time with pure water. Between every step, the samples were placed in an ultrasound bath for 10 minutes.

Bromophenyl Tetrafluoroborates: These compounds were prepared as described in literature.[2] 4-Bromoaniline (0.25 mol) was dissolved in 110 mL of tetrafluoroboric acid solution under stirring and being cooled in an ice bath an. A cold solution of sodium nitrite (17g, 0.25 mol) in 34 mL water is added dropwise and stirred for 30 minutes. Then, the precipitation was filtered off and washed once with cold fluoroboric acid (≈ 30 mL), for two times with 95% ethanol and for further two times with ether. Yield: 73%.

***tert*-Butyl 2-(4-cyanophenyl)azocarboxylate**: (4-cyano)-hydrazine (11.8 mmol, 2.0 g) is dissolved in dry acetonitrile (20 mL) and treated with di-*tert*-butyl dicarbonate (13.0 mmol, 2.84 g) under argon atmosphere. After complete consumption of the reactants, as monitored by

TLC, the solvent is removed under reduced pressure. The residue is subjected to column chromatography (silica gel, 1:0→100:1→50:1→25:1 dichloromethane/methanol) to give *tert*-butyl 2-(4-cyanophenyl)hydrazine-1-carboxylate (10.6 mmol, 2.46 g, 89%) as a yellow solid. R_f = 0.3 in 100:1 dichloromethane/methanol. ^{1}H NMR (400 MHz, $CDCl_3$, 25°C, TMS): *δ*=7.5 – 7.5 (m, 2H), 6.9 – 6.8 (m, 2H), 6.4 (s, 1H), 1.5 ppm (s, 9H).

To a stirred solution of 2-(4-cyanophenyl)hydrazine-1-azocarboxylate (9.26 mmol, 2.16 g) in dry dichloromethane (20 mL), manganese dioxide (46.5 mmol, 4.04 g) is subsequently added under nitrogen atmosphere. After complete consumption of the reactants, as monitored by TLC, the mixture is filtered over Celite. Removal of the solvent under reduced pressure and column chromatography (silica gel, 20:1→10:1→8:1→5:1 hexane/ethyl acetate) give *tert*-butyl 2-(4-cyanophenylazocarboxylate (6.88 mmol, 1.59 g, 74%) as an yellow solid. R_f=0.4 (10:1 hexane/ethylacetate). ^{1}H NMR (400 MHz, $CDCl_3$, 25°C, TMS): *δ*=8.0 – 7.9 (m, 2H), 7.8 – 7.8 (m, 2H), 1.7 ppm (s, 9H).^{13}C NMR (101 MHz, $CDCl_3$, 25°C, TMS): *δ*=160.7 (C_q), 153.4 (C_q), 133.5 (2 × CH), 124.0 (2 × CH), 118.0 (C_q), 116.4 (C_q), 86.1 (C_q), 28.0 (3 × CH_3).; HR-MS (ESI) calculated for $C_{12}H_{13}N_3O_2$ [M^+ + Na^+]: 251.0900 u, found: 251.0896 u.

***tert*-Butyl 2-(4-bromophenyl)azocarboxylate**: A solution of 4-bromoaniline (28.0 mmol, 4.82 g) in glacial acetic acid (15 mL) is treated with concentrated hydrochloric acid (60 mL) and cooled to 0 °C. A solution of sodium nitrite (28.0 mmol, 1.93 g) in water (6.5 mL) is added over a period of 20 minutes and the reaction is stirred for one hour at 0° C. A solution of tin chloride dihydrate (62.0 mmol, 14.0 g) in concentrated hydrochloric acid (15 mL) is added dropwise over a period of 45 minutes. After stirring for one hour at 0 °C, the precipitate is collected by filtration and dissolved in a saturated aqueous solution of potassium carbonate (200 mL). The composite is extracted with diethyl ether (4 × 50 mL). The combined organic phases are washed with a saturated aqueous solution of sodium chloride and dried over sodium sulfate. The crude product is used without further purification. The crude product is dissolved in dry acetonitrile (30 mL) and treated with di-*tert*-butyl dicarbonate (27.1 mmol, 5.92 g) under argon atmosphere. After complete consumption of the reactants, as monitored by TLC, the solvent is removed under reduced pressure. The residue is subjected to column chromatography (silica gel, hexane/ethyl acetate = 6:1) to give *tert*-butyl 2-(4-bromophenyl)hydrazine carboxylate (16.4 mmol, 4.70 g, 59%) as a white solid. R_f=0.3 in 6:1 hexane/ethyl acetate. ^{1}H NMR (600 MHz, $CDCl_3$, 25°C, TMS): *δ*=7.3 (d, *J*=8.8 Hz, 2 H), 6.7 (d, *J*=8.8 Hz, 2 H), 6.4 (bs, 1 H), 1.46 ppm (s, 9 H).

To a stirred solution of *tert*-butyl 2-(4-bromophenyl)hydrazine carboxylate (16.5 mmol, 4.70 g) in dry dichloromethane (30 mL), manganese dioxide (82.5 mmol, 7.17 g) is subsequently added under nitrogen atmosphere. After complete consumption of the reactants, as monitored by TLC, the mixture is filtered over Celite. Removal of the solvent under reduced pressure and column chromatography (silica gel, 20:1 hexane/ethyl acetate) give *tert*-butyl 2-(4-bromophenyl)azocarboxylate (14.7 mmol, 4.18 g, 89%) as an orange solid. R_f=0.7 (15:1 hexane/ethyl acetate). ^{1}H NMR (600 MHz, $CDCl_3$, 25°C, TMS): *δ*=7.77 (d, *J*=8.9 Hz, 2 H), 7.65 (d, *J*=8.9 Hz, 2 H),1.65 (s, 9 H). ^{13}C NMR (91 MHz, $CDCl_3$, 25°C, TMS): *δ*=160.9 (Cq), 150.3 (Cq), 132.6 (2 × CH), 128.2 (Cq), 124.9 (2 × CH), 85.3 (Cq), 27.8 ppm (3 × CH3). HR-MS (ESI) calculated for $C_{11}H_{13}BrN_2O_2$ [M^+ + Na^+]: 307.0053 u, found: 307.0058 u.

***tert*-Butyl 2-(4-(heptyloxy)phenyl)azocarboxylate**: A solution of 4-nitrophenol (28.8 mmol, 4.0 g) and anhydrous potassium carbonate (57.5 mmol, 7.95 g) in dry acetonitrile (60 mL) is treated with 1-iodoheptane (57.5 mmol, 9.43 mL) under argon atmosphere. The reaction mixture is stirred for 24 h under reflux. After the reaction is completed, the hot reaction mixture is filtered and the solvent is removed under reduced pressure. The crude product, 1-(heptyloxy)-4-nitrobenzene, is washed with dichloromethane (40 mL) and filtrated.1-(heptyloxy)-4-nitrobenzene (21.1 mmol, 5.02 g, 73%) is received as a yellow oil. R_f = 0.3 in 20:1 hexane/ethyl acetate. ^{1}H NMR (400 MHz, $CDCl_3$, 25°C, TMS): *δ*=8.2 – 8.2 (m, 2H), 7.0 – 6.9 (m, 2H), 4.1 (t, *J*(H,H)=7 Hz, 2H), 1.9 – 1.8 (m, 2H), 1.5 – 1.4 (m, 2H), 1.4 – 1.3 (m, 6H), 0.9 ppm (t, *J*(H,H)=7 Hz, 3H).

1-(heptyloxy)-4-nitrobenzene (21.2 mmol, 5.02 g) and tin(II) chloride dihydrate (84.6 mmol, 19.1 g) are dissolved in concentrated hydrochloric acid (14.9 mL) and absolute ethanol (30 mL). The reaction mixture is stirred at room temperature. After complete consumption of the reactants, as monitored by TLC, the solvent is removed under reduced pressure. The crude product is diluted with water and treated with saturated sodium carbonate until a pH value of 9.5 is reached. The crude product is extracted with ethyl acetate (3 x 50 mL) and purified by column chromatography (silica gel, 2:1→1:1 hexane / ethyl acetate) to give *tert*-butyl 4-(heptyloxy)aniline (12.7 mmol, 2.64 g, 60%) as a brown oil. R_f=0.3 in 1:1 hexane/ethyl acetate. ^{1}H NMR (400 MHz, $CDCl_3$, 25°C, TMS): *δ*=6.8 – 6.7 (m, 2H), 6.7 – 6.6 (m, 2H), 3.9 (t, *J*(H,H)=7 Hz, 2H), 3.3 (s, 1H), 1.8 – 1.7 (m, 2H), 1.5 – 1.4 (m, 2H), 1.4 – 1.2 (m, 6H), 0.9 ppm (t, *J*(H,H)=7 Hz, 3H).

A solution of 4-(heptyloxy)aniline (6.51 mmol, 1.35 g) in glacial acetic acid (5.0 mL) is treated with concentrated hydrochloric acid (14.7 mL) and cooled to 0 °C. A solution of sodium nitrite (6.51 mmol, 0.45 g) in water (1.5 mL) is added over a period of 10 minutes and the reaction is stirred for one hour at 0° C. A solution of tin (II) chloride dihydrate (14.3 mmol, 3.23 g) in concentrated hydrochloric acid (3.5 mL) is added dropwise over a period of 15 minutes. After stirring for three hours at 0 °C, the precipitate is collected by filtration and dissolved in a saturated aqueous solution of potassium carbonate (200 mL). The composite is extracted with dichloromethane (4 × 50 mL). The combined organic phases are washed with a saturated aqueous solution of sodium chloride and dried over sodium sulfate. The crude product is used without further purification. The crude product (5.58 mmol, 1.30 g) is dissolved in dry acetonitrile (10 mL) and treated with di-*tert*-butyl dicarbonate (6.44 mmol, 1.40 g) under argon atmosphere. After complete consumption of the reactants, as monitored by TLC, the solvent is removed under reduced pressure. The residue is subjected to column chromatography (silica gel, 20:1→10:1→5:1 hexane/ethyl acetate) to give *tert*-butyl 2-(4-(heptyloxy)phenyl)hydrazine-1-carboxylate (2.86 mmol, 0.92 g, 44%) as a yellow oil. R_f=0.3 in 8:1 hexane/ethyl acetate. ^{1}H NMR (400 MHz, $CDCl_3$, 25°C, TMS): *δ*=6.8 – 6.8 (m, 4H), 6.4 (s, 1H), 3.9 (t, *J*(H,H)=7 Hz, 2H), 1.8 – 1.7 (m, 2H), 1.5 – 1.3 (m, 17H), 0.9 ppm (t, *J*(H,H)= 7 Hz, 3H).

To a stirred solution of 2-(4-(heptyloxy)phenyl)hydrazine-1-carboxylate (1.97 mmol, 0.63 g) in dry dichloromethane (12 mL), manganese dioxide (9.83 mmol, 0.86 g) is subsequently added under nitrogen atmosphere. After complete consumption of the reactants, as monitored by TLC, the mixture is filtered over Celite. Removal of the solvent under reduced pressure and column chromatography (silica gel, 30:1→20:1 hexane/ethyl acetate) give *tert*-butyl 2-(4-(heptyloxy)phenyl)azocarboxylate (1.50 mmol, 0.48 g 76%) as an orange oil. R_f=0.5 (20:1 hexane/ethylacetate). ^{1}H NMR (400 MHz, $CDCl_3$, 25°C, TMS): *δ*=8.0 – 7.9 (m, 2H), 7.0 – 6.9 (m, 2H), 4.0 (t, *J*(H,H)=7 Hz, 2H), 1.9 – 1.8 (m, 2H), 1.7 (s, 9H), 1.5 – 1.4 (m, 2H), 1.4 – 1.3 (m, 6H), 0.9 ppm (t, *J*(H,H)=7 Hz, 3H). ^{13}C NMR (151 MHz, $CDCl_3$, 25°C, TMS): *δ*=164.1 (C_q), 161.3 (C_q), 146.0 (C_q), 126.4 (2 × CH), 114.9 (2 × CH), 84.5 (C_q), 68.7 (CH_2), 31.9 (CH_2), 29.2 (CH_2), 29.2 (CH_2), 28.0 (3 × CH_3), 26.1 (CH_2), 22.7 (CH_2), 14.2 ppm (CH_3); HR-MS (ESI) calculated for $C_{18}H_{28}N_2O_3$ [M^+ + Na^+]: 343.1992 u, found: 343.1987 u.

***tert*-Butyl 2-(4-nitrophenyl)carboxylate**: (4-nitrophenyl)-hydrazine (70% in water, 6.85 mmol, 1.50 g) is dissolved in dry acetonitrile (5 mL) and treated with di-*tert*-butyl dicarbonate (8.22 mmol, 1.75 g) under nitrogen atmosphere. After complete consumption of the reactants, as monitored by TLC, the solvent is removed under reduced pressure. The residue is dissolved in ethyl acetate (20 mL). After addition of saturated aqueous sodium bicarbonate solution (40 mL), the crude product was extracted with ethyl acetate (3 x 50 mL) and then purified by column chromatography (silica gel, 25:1 dichloromehtane/methanol) to give *tert*-butyl 2-(4-nitrophenyl)hydrazine-1-carboxylate (5.68 mmol, 1.43 g, 83%) as a yellow solid. R_f=0.3 (25:1 dichloromethane/methanol). ^{1}H NMR (400 MHz, $CDCl_3$, 25°C, TMS): δ=8.2 – 8.1 (m, 2H), 6.9 – 6.8 (m, 2H), 6.4 (s, 1H), 1.5 ppm (s, 9).

To a stirred solution of *tert*-butyl 2-(4-nitrophenyl)hydrazine-1-carboxylate (3.71 mmol, 0.94 g) in dry dichloromethane (15 mL), manganese dioxide (18.5 mmol, 1.61 g) is subsequently added under nitrogen atmosphere. After complete consumption of the reactants, as monitored by TLC, the mixture is filtered over Celite. Removal of the solvent under reduced pressure and column chromatography (silica gel 20:1 → 10:1 hexane/ethyl acetate) give *tert*-butyl 2-(4-nitrophenyl)azocarboxylate (3.69 mmol, 0.93 g, 96%) as an orange solid. R_f=0.4 in 10:1 hexane/ethyl acetate. ^{1}H NMR (400 MHz, $CDCl_3$, 25°C, TMS): δ=8.4 – 8.3 (m, 2H), 8.1 – 8.0 (m, 2H), 1.7 ppm (s, 9H).^{13}C NMR (101 MHz, $CDCl_3$, 25°C, TMS): δ=160.7 (C_q), 154.6 (C_q), 150.3 (C_q), 124.9 (2 × CH), 124.3 (2 × CH), 86.3 (C_q), 28.0 (3 × CH_3); HR-MS (ESI) calculated for $C_{11}H_{13}N_3O_4$ [M^+ + Na^+]: 274.0798 u, found: 274.0792 u.

4-Bromobenzenediazonium tetrafluoroborate*:* The diazonium compound was synthesized according to the literature.[3] 100 mmol of 4-bromoaniline was dissolved in 100 mL of 25 % tetrafluoro bonornic acid and added to a solution of 100 mmol $NaNO_2$ in 10 ml water at 0 °C. After mixing both solutions for approximately 30 minutes the precipitation was filtered off and re-dissolved in 50 mL acetone. The final product was precipitated again by the addition of 50 mL of diethyl ether, filtered and vacuum dried.

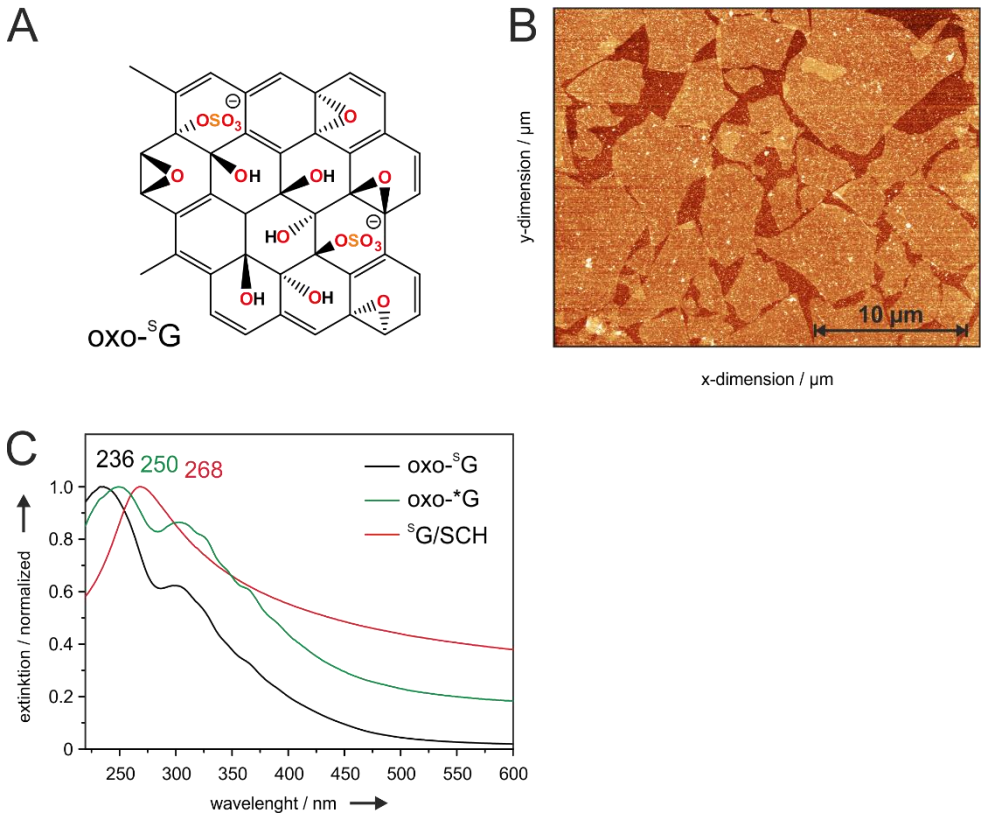

Figure S1: (A) Structure of oxo-^{S}G. (B) AFM image of oxo-G deposited on 300 nm SiO_2/Si wafer by Langmuir-Blodgett technique. (C) Normalized UV-vis spectra of aqueous dispersions of oxo-^{S}G, oxo-*G and ^{S}G/SCH.

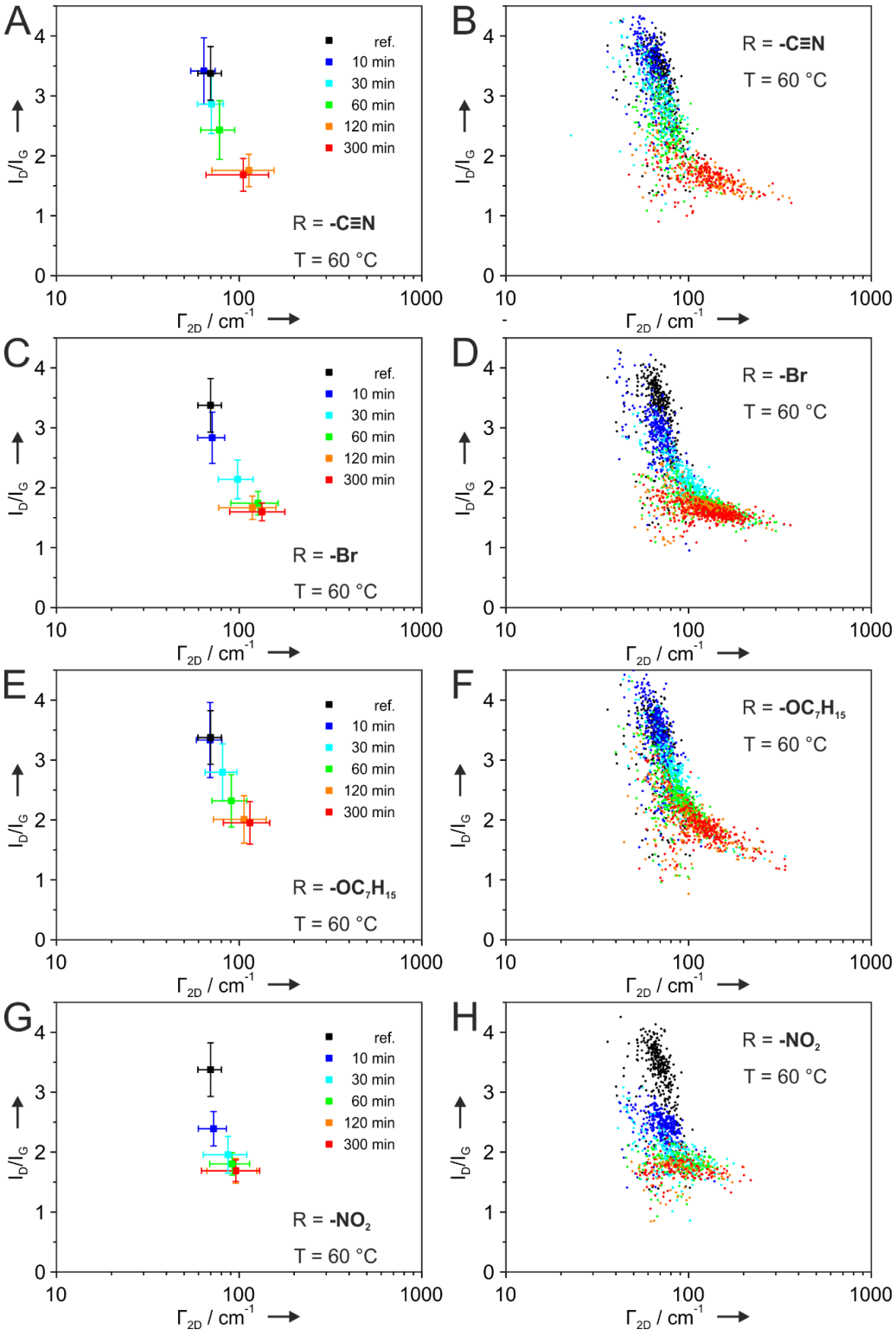

Figure S2: Statistical Raman analysis of functionalized graphene sheets deposited on 300 nm SiO_2/Si wafer. The temperature was 60 °C and the concentration of the 4-phenylazocarboxylic ester was set to 2 mM.

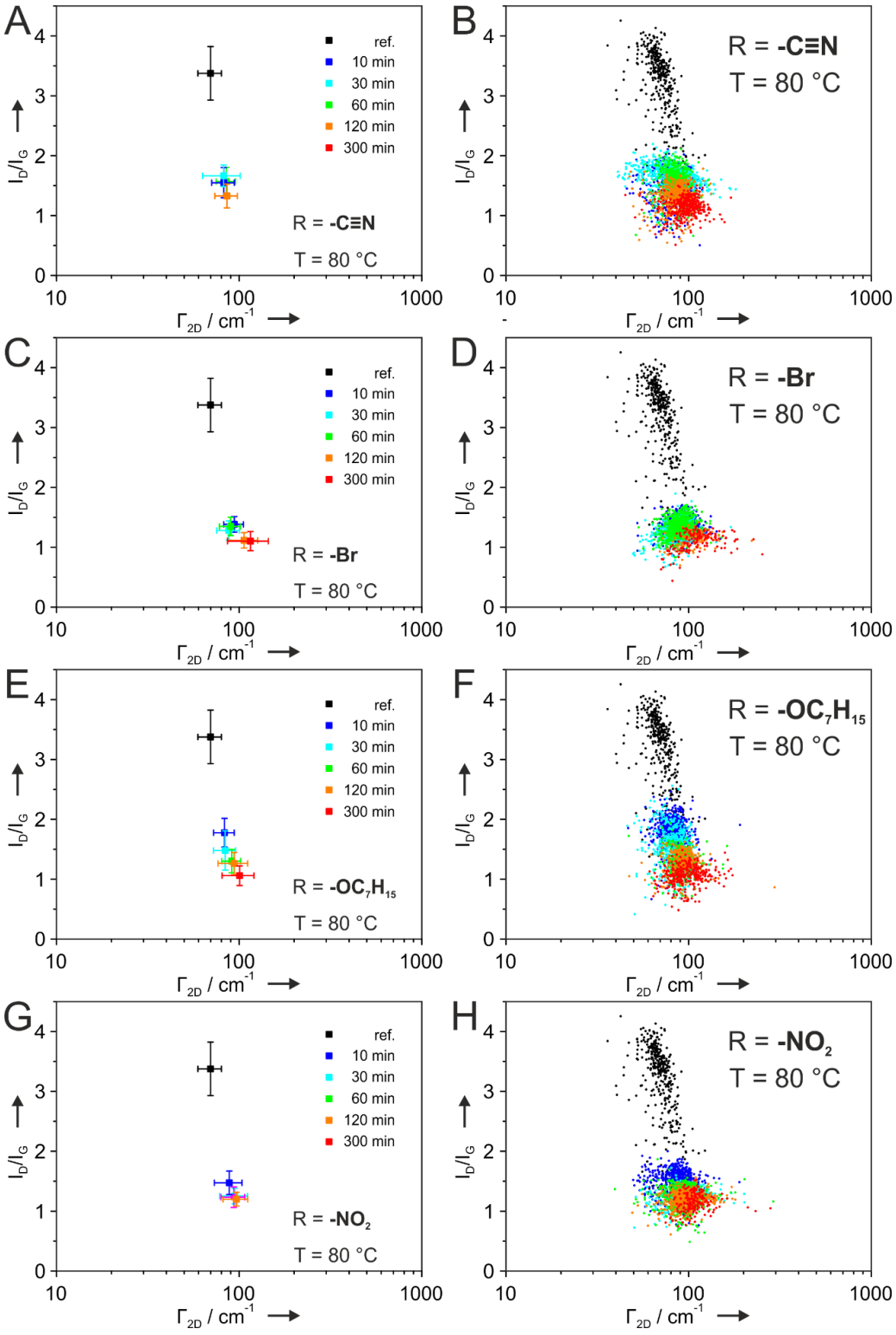

Figure S3: Statistical Raman analysis of functionalized graphene sheets deposited on 300 nm SiO_2/Si wafer. The temperature was 80 °C and the concentration of the 4-phenylazocarboxylic was set to 2 mM.

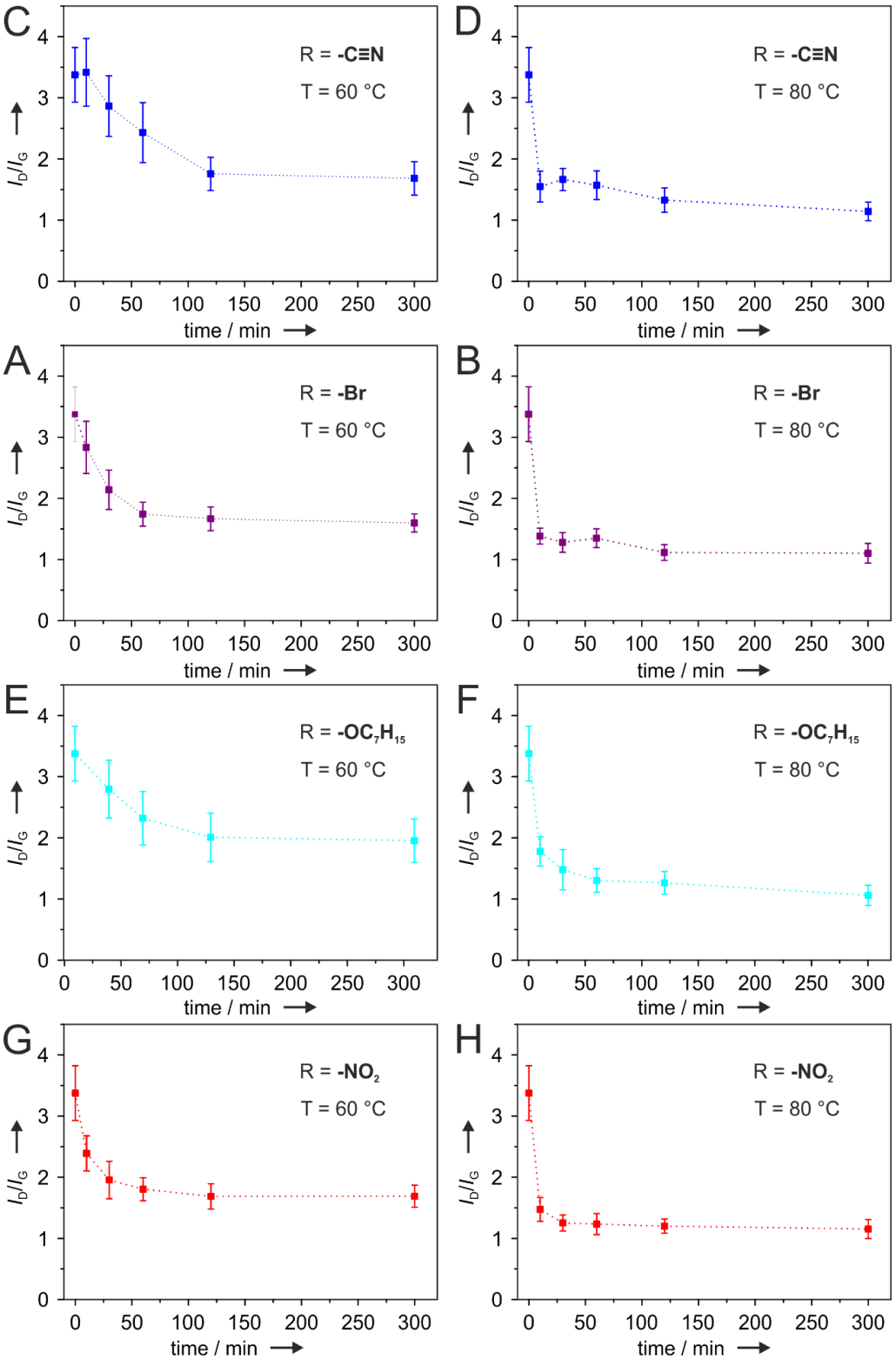

Figure S4: Statistical Raman analysis of functionalized graphene sheets deposited on 300 nm SiO_2/Si wafer after each time step. The temperature was 60 °C (left) and 80 °C (right). The concentration of the 4-phenylazocarboxylic was set to 2 mM.

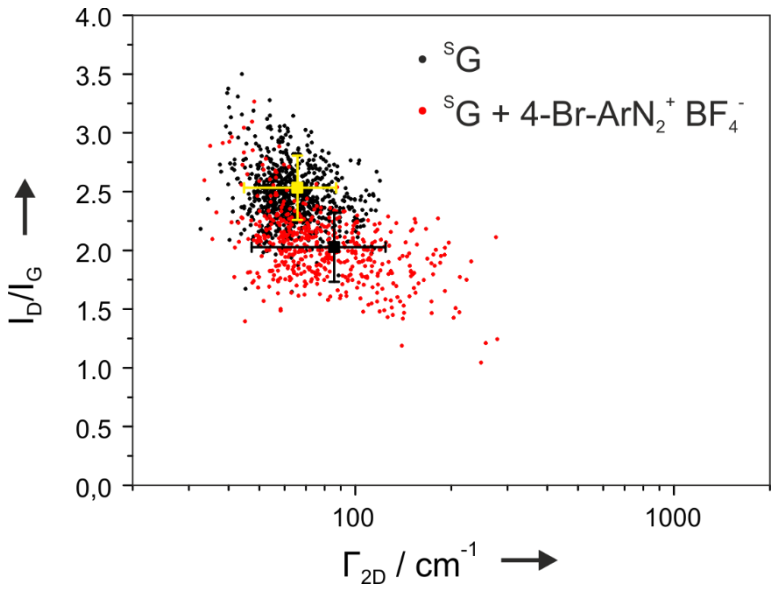

Figure S5: Statistical Raman analysis of functionalized graphene before and after functionalization by 4-Bromobenzenediazonium tetrafluoroborate.

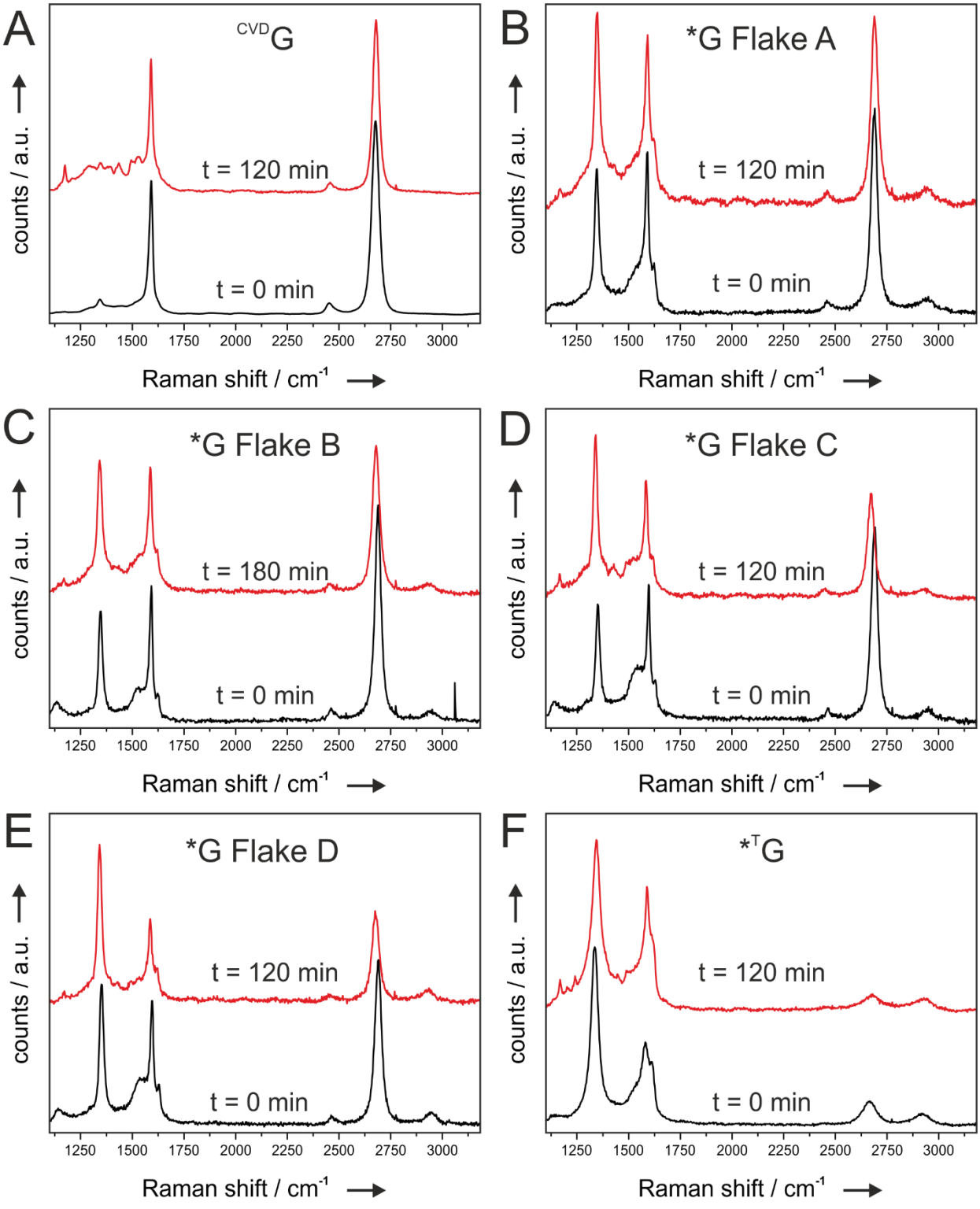

Figure S6: Representative spectra of all recorded flakes of *G and *^{T}G before and after functionalization at 60°C. The reaction times are given in the diagram.

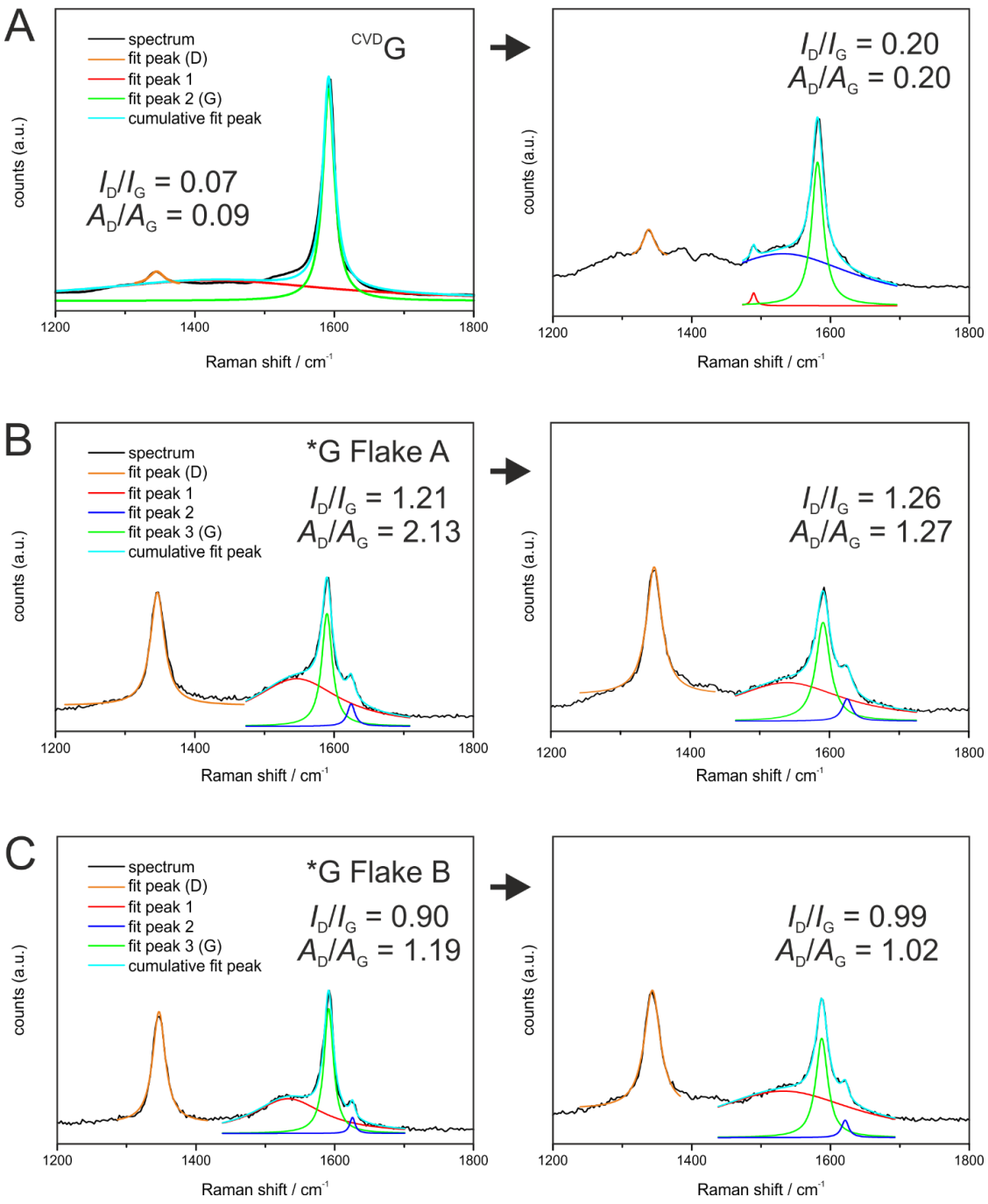

Figure S7: Magnification into the region of the D and G mode of the spectra shown in figure S7. The left spectrum corresponds to the initial flake of *G or *TG, respectively, and the right to the functionalized material. Coloured curves represent fits of the individual Raman modes. Corresponding I_D/I_G and A_D/A_G ratios are given for each spectrum.

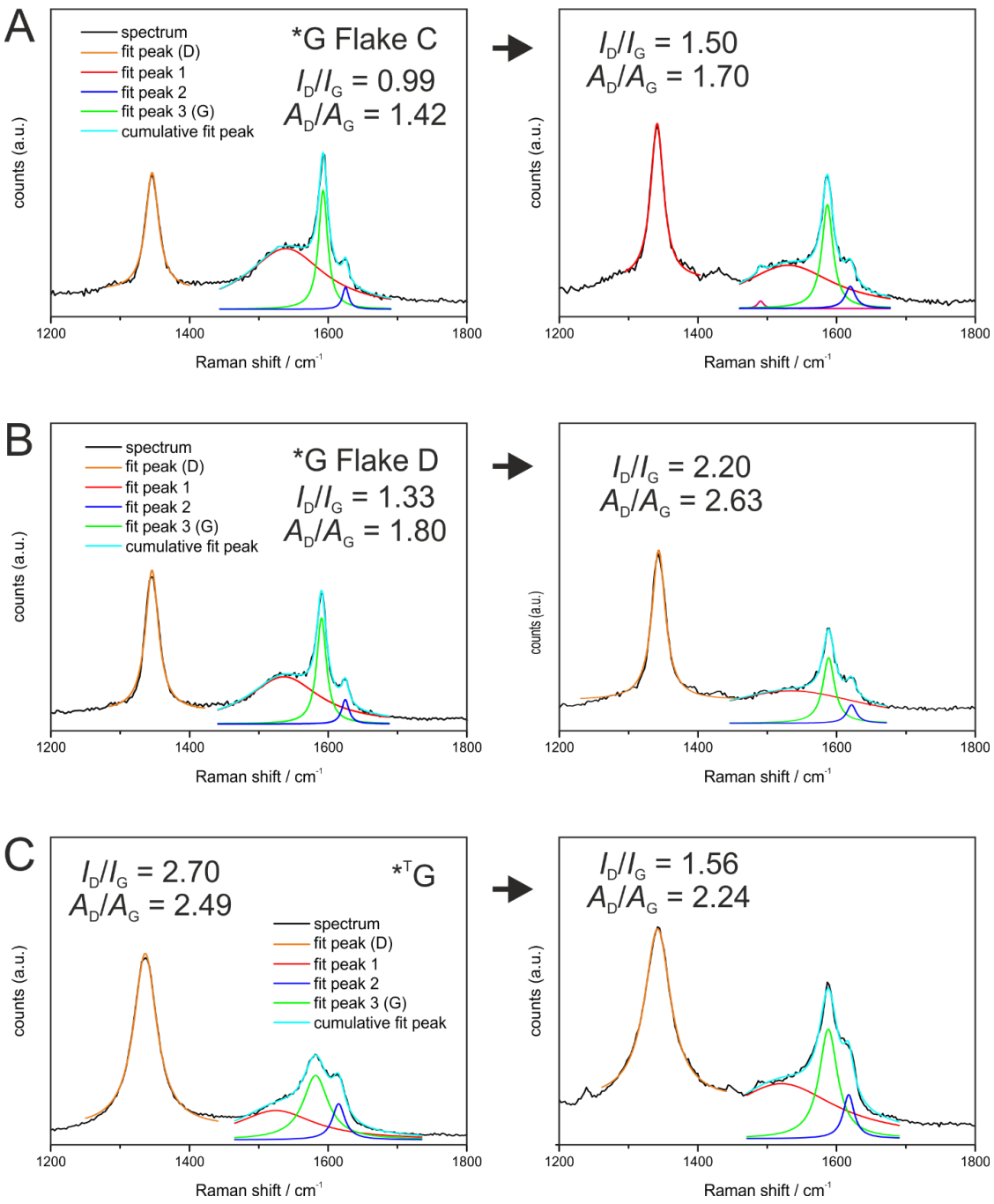

Figure S8: Magnification into the region of the D and G mode of the spectra shown in figure S7. The left spectrum corresponds to the initial flake of *G or *TG, respectively, and the right to the functionalized material. Coloured curves represent fits of the individual Raman modes. Corresponding I_D/I_G and A_D/A_G ratios are given for each spectrum.

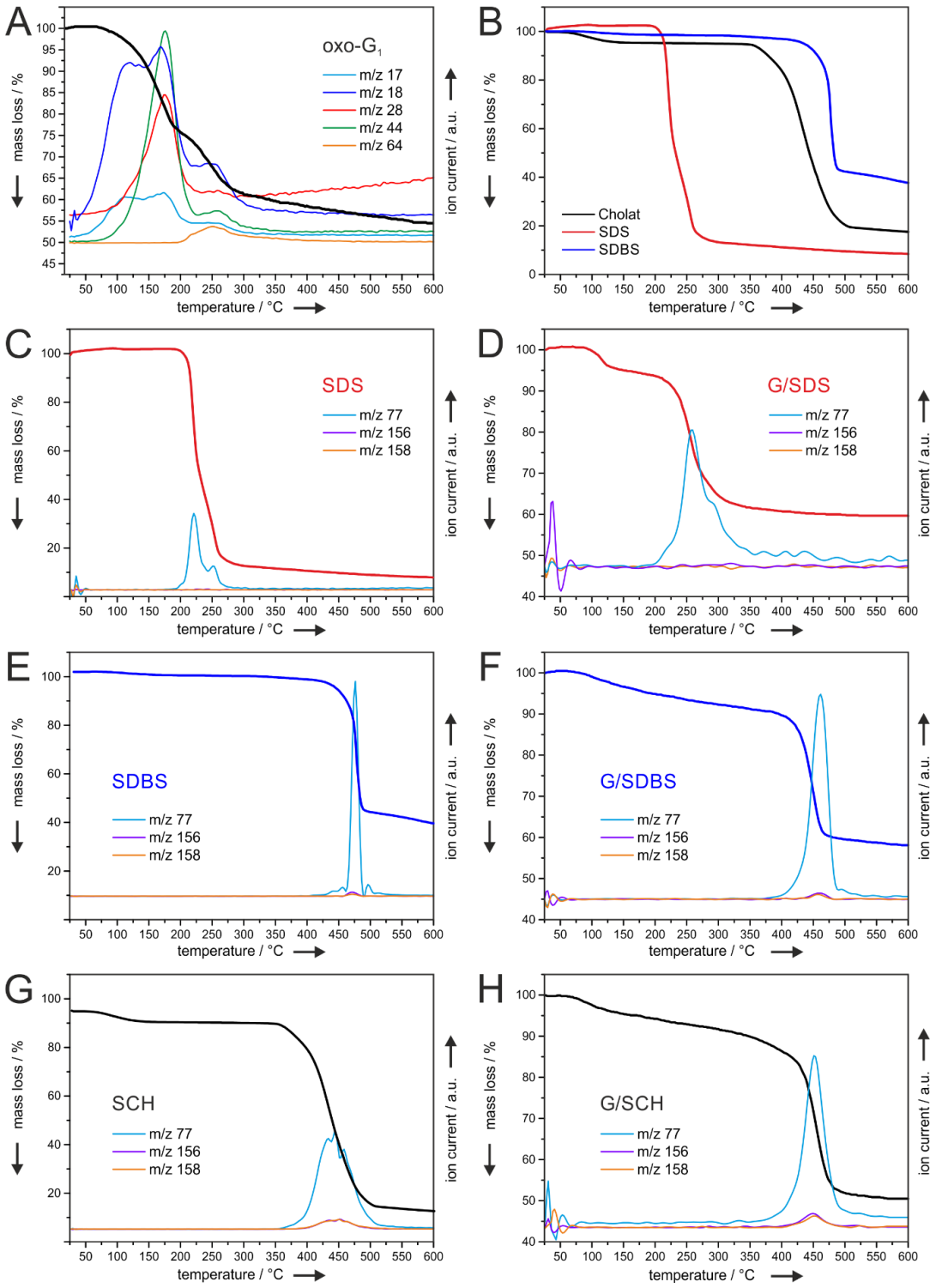

Figure S9: TGA-MS of oxo-G_1, thereout produced G/Surfactant compounds used for functionalization and the pure surfactants as references: **(A)** initial oxo-G: TG-curve (black) and corresponding ion currents (coloured). (B) TGA of SDS, SDBS and SCH. **(C-H)** Pairs of surfactants (SDS, SDBS and SCH) and their corresponding graphene-surfactant-compound. The fragments shown by their m/z values 77/156/158 can either be referred to cleaved aromatic fragments after functionalization and also to decomposition products of the used surfactants and therefore shown in each diagram.

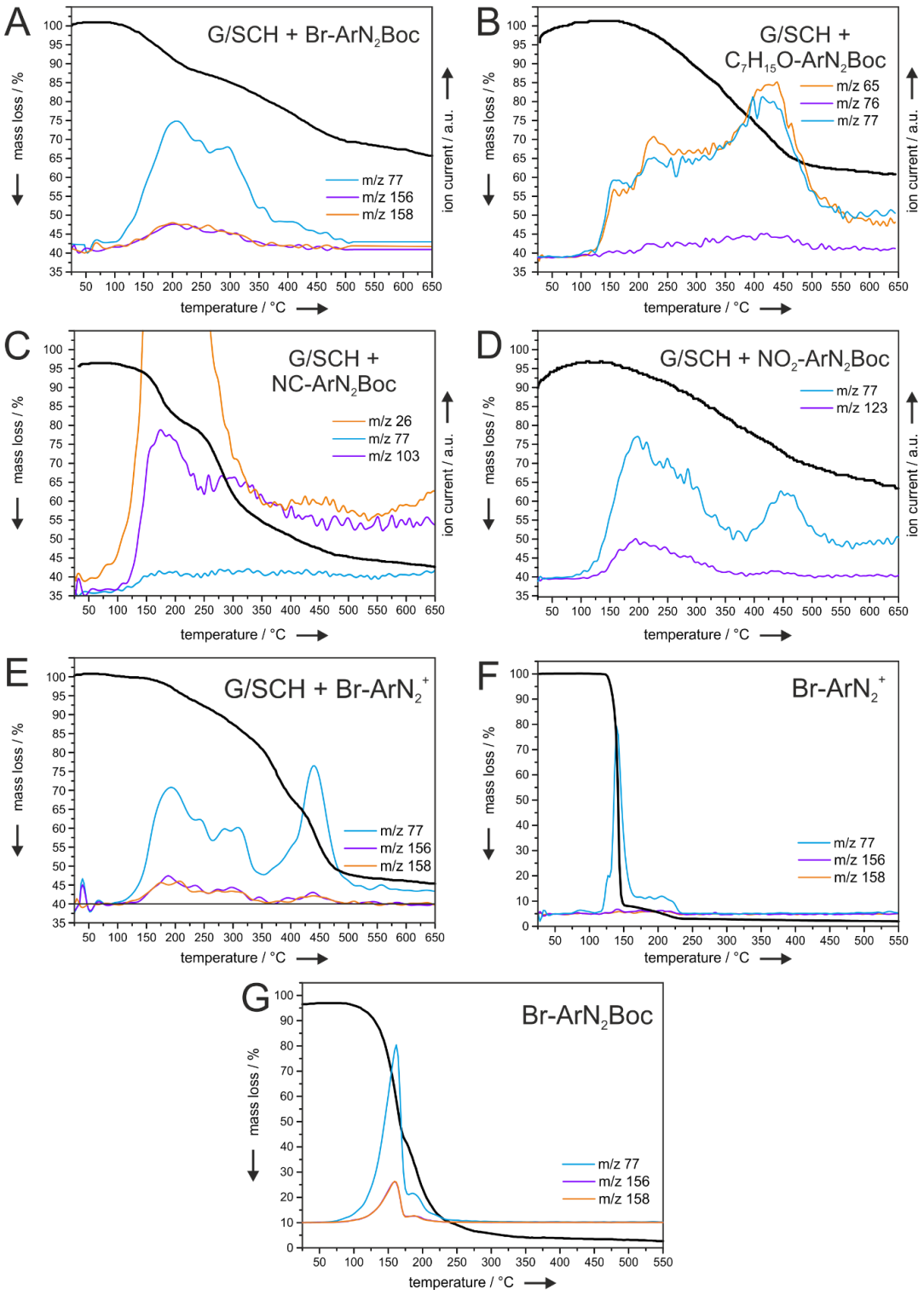

Figure S10: TGA-MS of all arylated graphene-surfactant-compounds in bulk. (A) graphene functionalized with 4-bromophenyl azocarboxylic ester, (B) 4-heptyloxy phenyl azocarboxylic ester, (C) 4-nitrophenyl azocarboxylic ester, (D) 4-nitrophenyl azocarboxylic ester. (E) Graphene functionalized with 4-bromobenzenediazonim tetrafluoroborate as a reference. (F-G) TGA-MS profiles of the initially used 4-bromobenzenediazonium tetrafluoroborate and 4-bromophenylazocarboxylic ester.

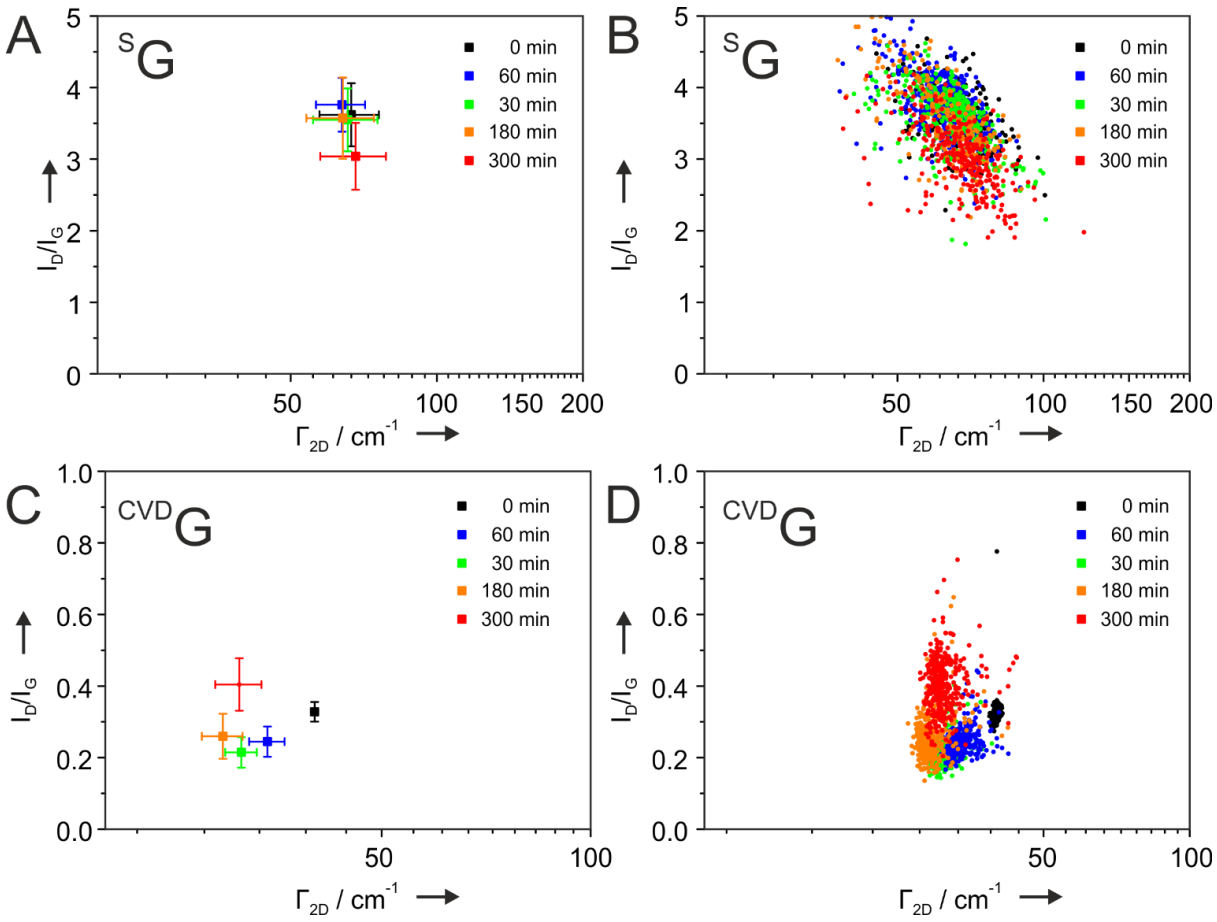

Figure S111: Statistical Raman analysis of ^{CVD}G and ^{S}G, placed in acetonitrile-water mixture (50:50) and trifluoro acetic acid and stored for up to 300 minutes at 60 °C. The reaction conditions are similar to the conditions used to functionalize the graphene derivatives, but without any functionalization agent.

Table S5: Overview of the evaluated spectra obtained by (statistical) Raman spectroscopy for all synthesized and functionalized graphene-based compounds on 300 nm SiO_2/Si surfaces. The reaction conditions are annotated in the superscript and the reaction time was 120 minutes. The substituent in *para*-position of the used ArN_2Boc is named first followed by the reaction temperature (60 °C or 80 °C). The degree of functionalization for oxo-G is estimated from elemental analysis and for and oxo-*G taken from the literature.

compound	I_D/I_G	Γ_{2D} [cm-1]	L_D (nm)	Θ
oxo-^{S}G	1.11±0.04	200±54	<< 1	> 50 %
oxo-*G	0.98	>150	<< 1	~ 4 %
^{S}G/SCH	1.98	>150	1.7	0.93 %
***^{T}G**	2.70	81	2.0	0.7 %
^{S}G	3.38±0.45	70±10	2.3	0.5 %
***G (average)**	1.10	36	10.8	0.02 %
^{CVD}G	0.12	39	34.7	0.002 %
*G^{Br-60}	1.49	40	9.1	0.032 %
*$^{T}G^{Br-60}$	1.56	89	1.4	1.14 %
$^{CVD}G^{Br-60}$	0.20	32	26.8	0.0036 %
$^{S}G^{Br-60}$	1.67±0.19	118±41	1.6	1.09 %
$^{S}G^{Br-80}$	1.12±0.13	106±20	1.4	1.43 %
$^{S}G^{NO2-60}$	1.68±0.21	96±29	1.6	1.08 %
$^{S}G^{NO2-80}$	1.19±0.12	97±15	1.4	1.36 %
$^{S}G^{CN-60}$	1.76±0.27	113±42	1.6	1.05 %
$^{S}G^{CN-80}$	1.33±0.20	86±12	1.4	1.28 %
$^{S}G^{OC7H15-60}$	2.00±0.40	106±34	1.7	0.94 %
$^{S}G^{OC7H15-80}$	1.27±0.18	94±17	1.4	1.31 %

[1] a) C. E. Halbig, T. J. Nacken, J. Walter, C. Damm, S. Eigler, W. Peukert, *Carbon* **2016**, *96*, 897; b) H. Pieper, S. Chercheja, S. Eigler, C. E. Halbig, M. R. Filipovic, A. Mokhir, *Angew. Chem. Int. Ed.* **2016**, *55*, 405; c) C. E. Halbig, P. Rietsch, S. Eigler, *Molecules* **2015**, *20*, 21050.

[2] *Organic Syntheses* **1939**, *19*, 40.

[3] P. S. Gribanov, M. A. Topchiy, Y. D. Golenko, Y. I. Lichtenstein, A. V. Eshtukov, V. E. Terekhov, A. F. Asachenko, M. S. Nechaev, *Green Chemistry* **2016**, *18*, 5984.

***tert*-Butyl 2-(4-cyanophenyl)azocarboxylate (^{1}H and DEPTQ NMR in $CDCl_3$)**

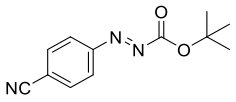

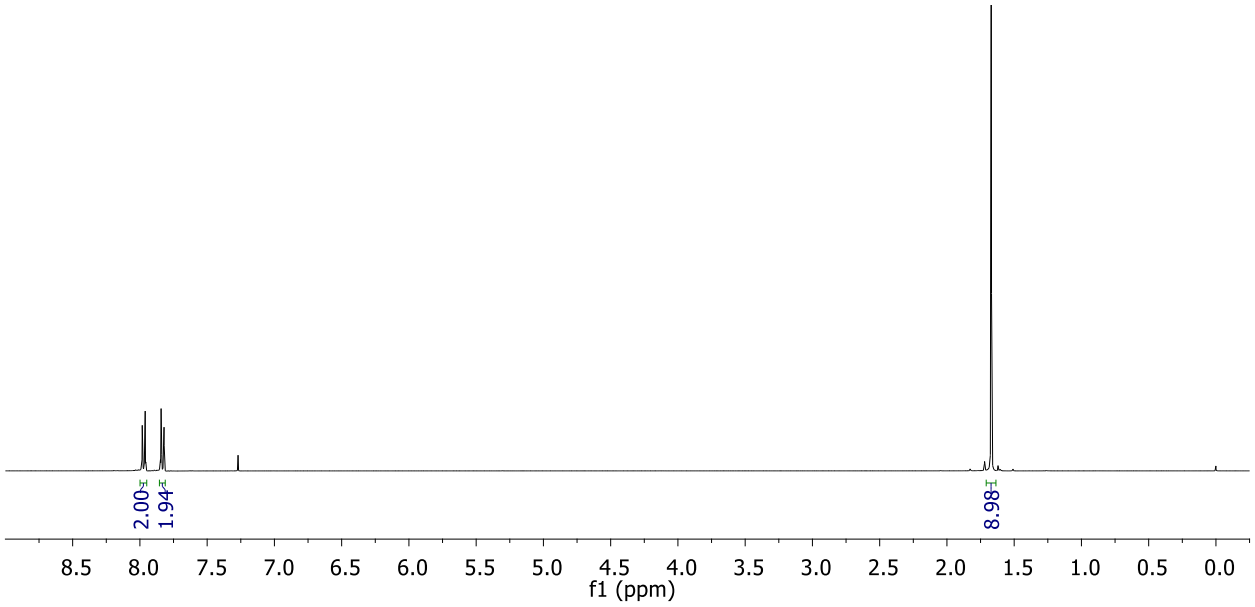

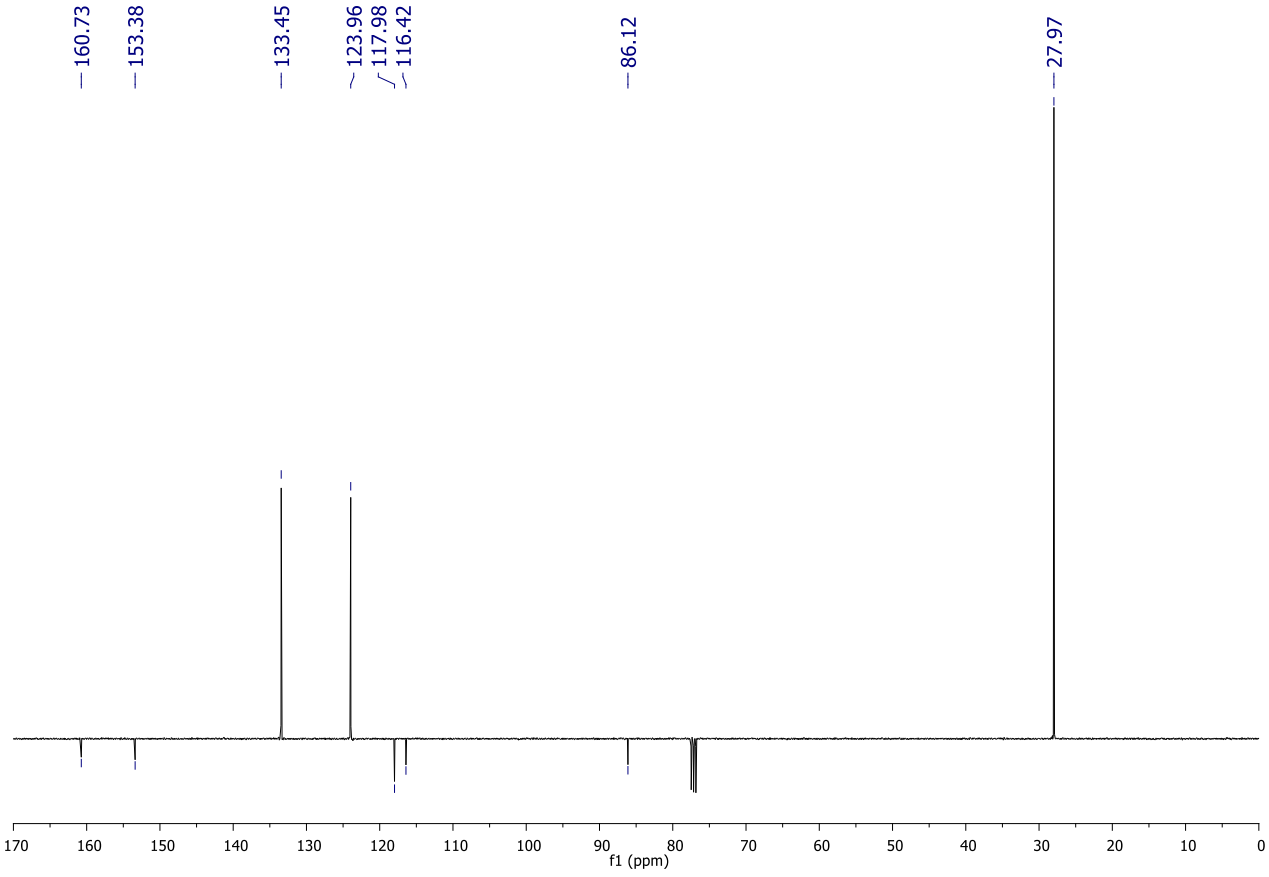

***tert*-Butyl 2-(4-bromophenyl)azocarboxylate (^{1}H and DEPTQ NMR in $CDCl_3$)**

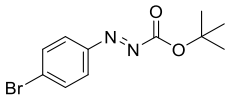

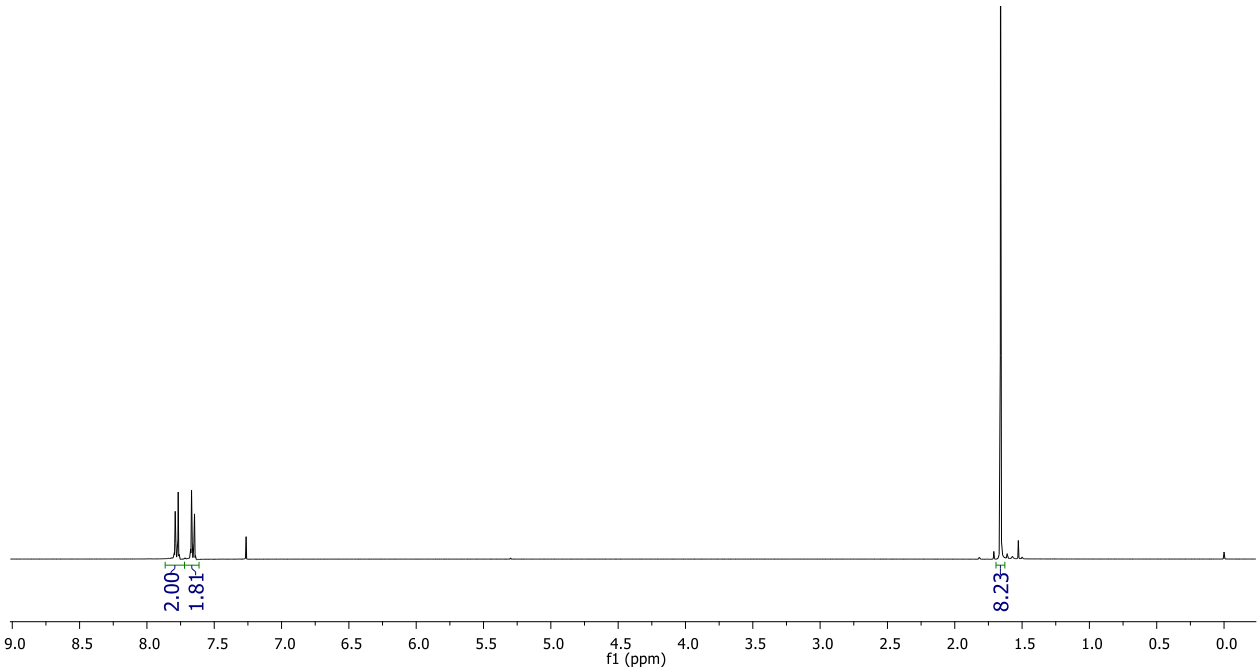

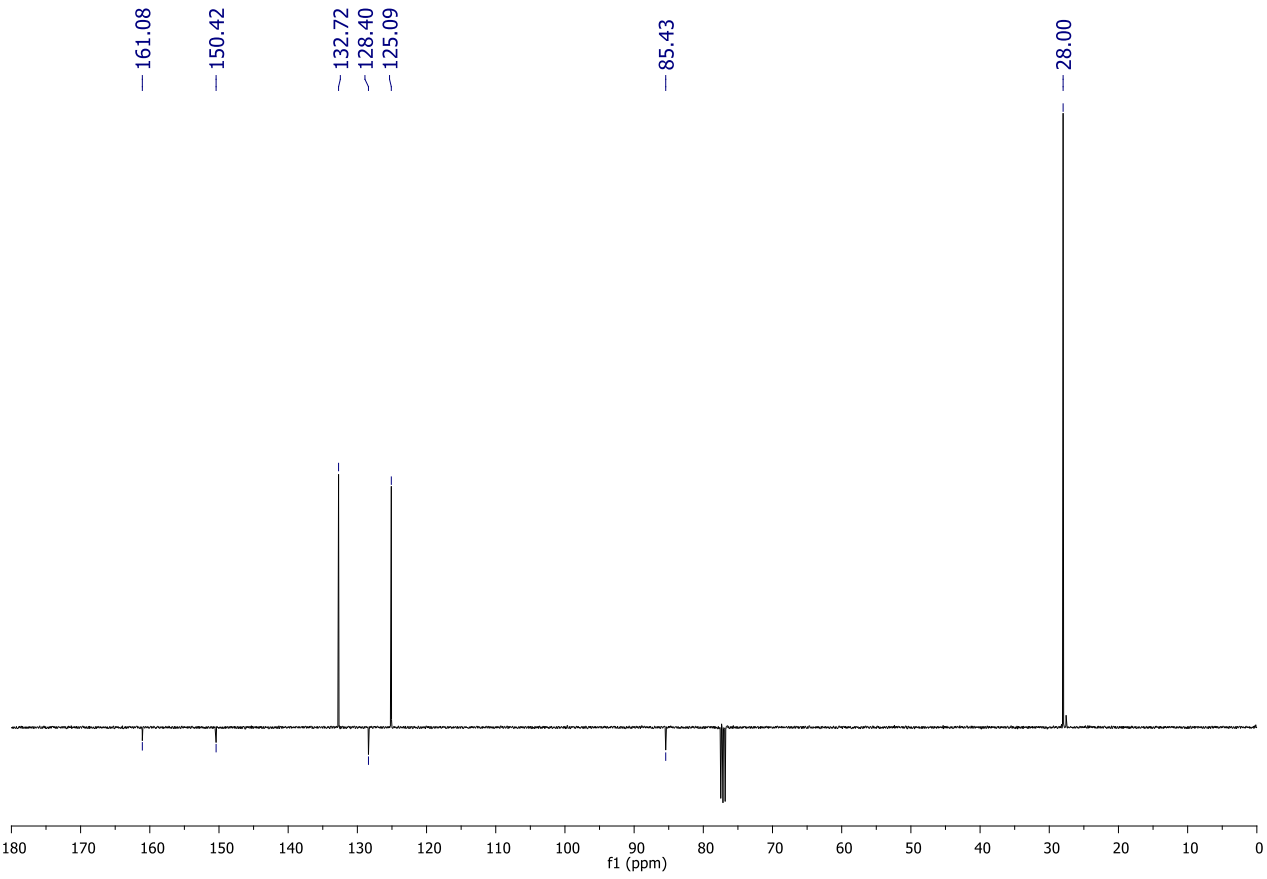

tert-Butyl 2-(4-(heptyloxy)phenyl)azocarboxylate (^{1}H and DEPTQ NMR in $CDCl_3$)

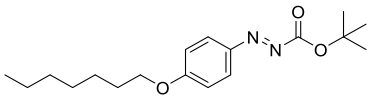

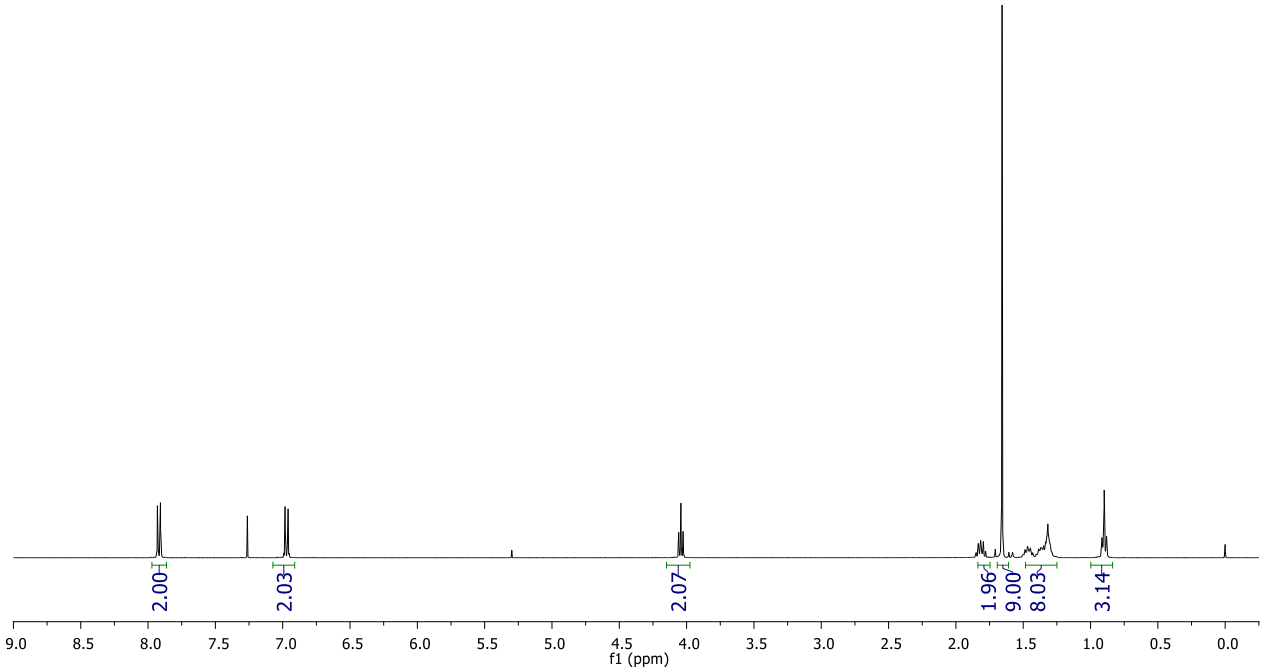

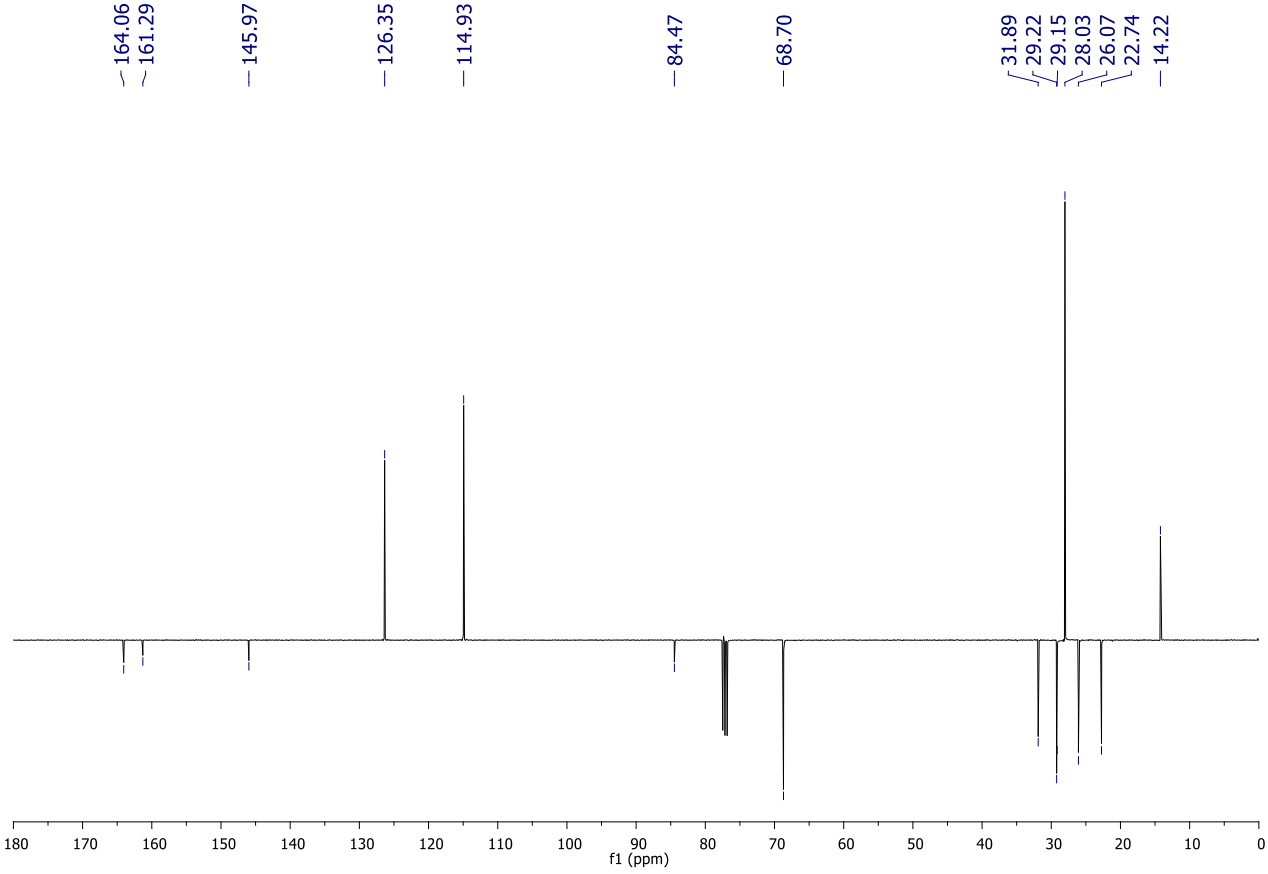

***tert*-Butyl 2-(4-nitrophenyl)azocarboxylate (^{1}H and DEPTQ NMR in $CDCl_3$)**

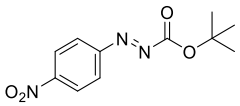

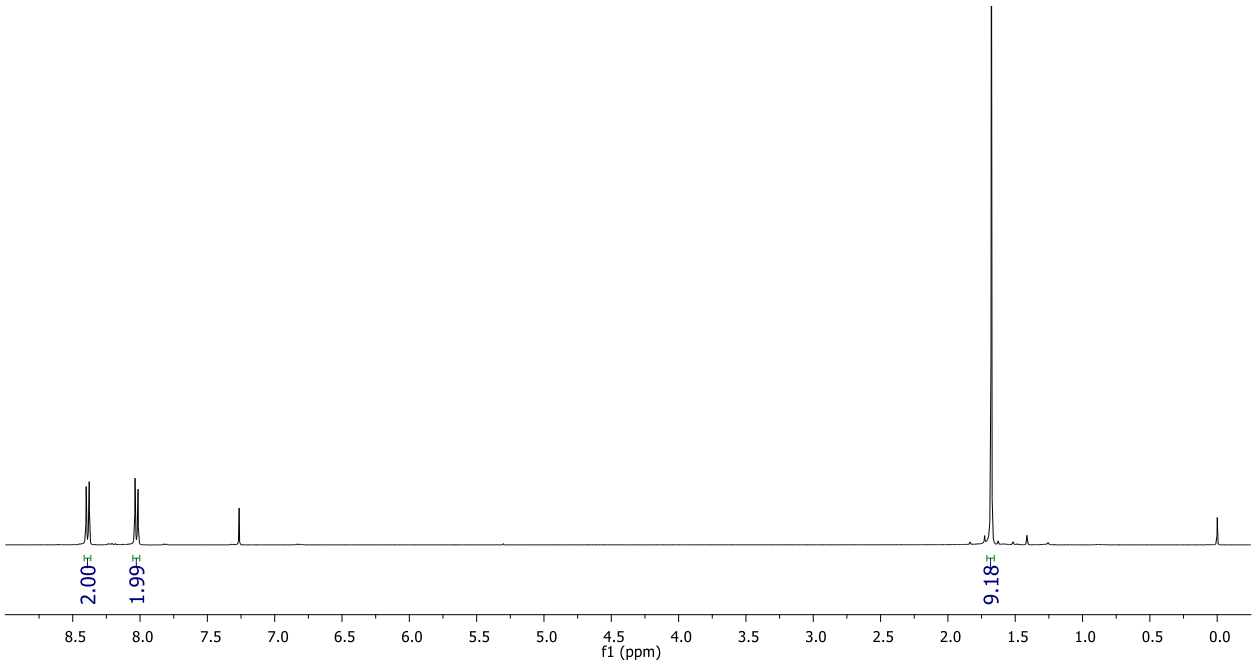

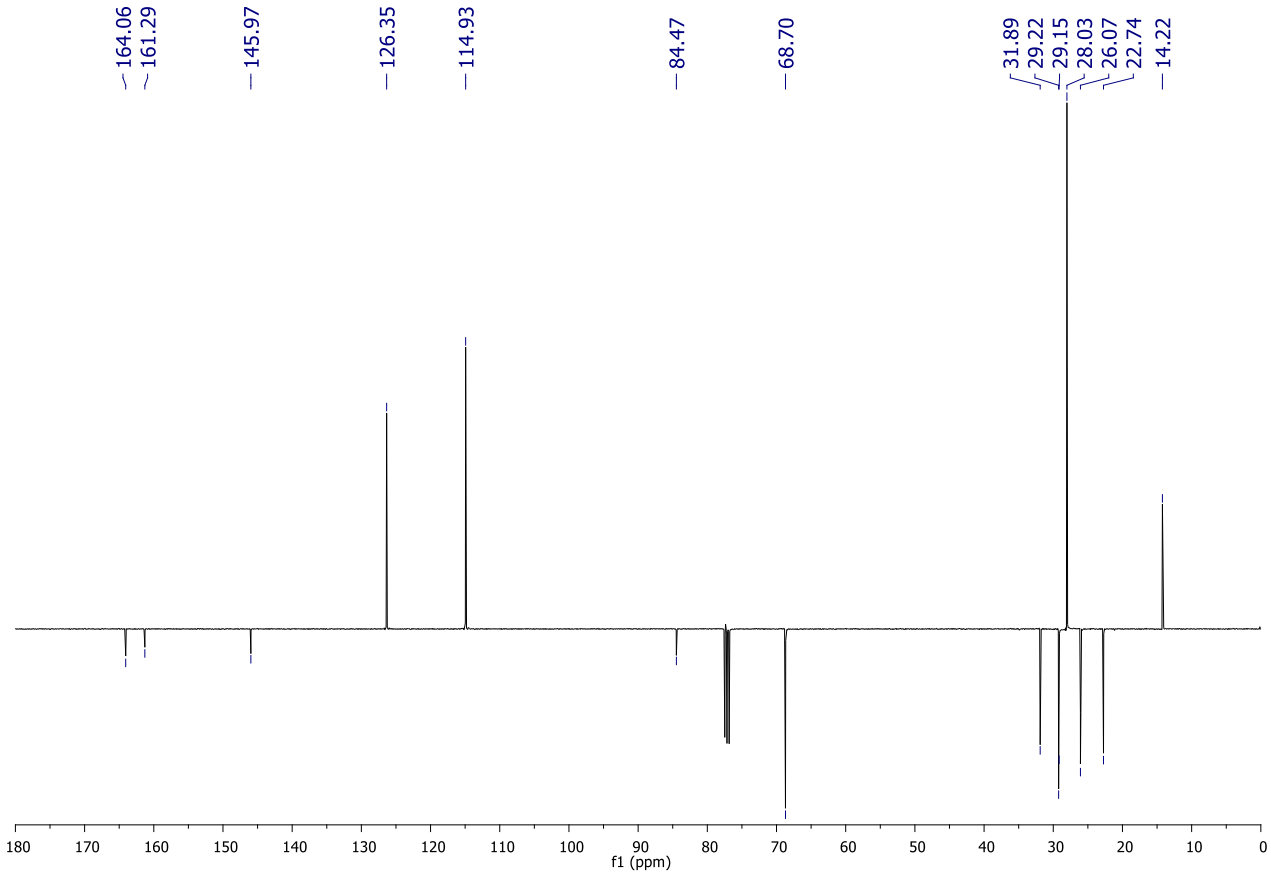

8. Publications: Minor Contributions

8.1. Graphene Oxide: A One- versus Two-Component Material

Authors	Naumov, F. Grote, M. Overgaard, A. Roth, C. E. Halbig, K. Nørgaard, D. M. Guldi, S. Eigler
Journal	J. Am. Chem. Soc., **2016**, 138 (36), 11445-11448
DOI	10.1021/jacs.6b05928
Links	http://dx.doi.org/10.1021/jacs.6b05928 https://pubs.acs.org/doi/10.1021/jacs.6b05928
Detailed scientific contribution	The concept of this manuscript was elaborated by Prof. Dr. A. Naumov and Prof. Dr. S. Eigler F. Grote, M. Overgaard and C. E. Halbig each prepared a different type of oxo-G. Isolation of OD were performed by M. Overgaard and C. E. Halbig. All prepared compounds were spectroscopically analysed by Prof. Dr. A. Naumov. Lifetime measurements were conducted by A. Roth. Samples for MS analysis were prepared by C. E. Halbig. Prof. Dr. S. Eigler, Prof. Dr. A. Naumov, Prof. Dr. K. Nørgaard and Prof. Dr. D. Guldi supervised the authors. The manuscript was mainly written by Prof. Dr. A. Naumov and Prof. Dr. S. Eigler.
Estimated own contribution	~ 15 %

8.2. Endoperoxides Revealed as Origin of the Toxicity of Graphene Oxide

Authors	H. Pieper, S. Chercheja, S. Eigler, C. E. Halbig, M. R. Filipovic, A. Mokhir
Journal	Angew. Chem. **2016**, 128 (1), 413-416 Angew. Chem. Int. Ed. **2016**, 55 (51), 405-407
DOI	10.1002/ange.201507070 10.1002/anie.201507070
Links	http://doi.org/10.1002/ange.201507070 http://doi.org/10.1002/anie.201507070 https://onlinelibrary.wiley.com/doi/full/10.1002/ange.201507070 https://onlinelibrary.wiley.com/doi/full/10.1002/anie.201507070
Contribution	The concept of this manuscript was elaborated by H. Pieper, Prof. Dr. A. Mokhir and Prof. Dr. S. Eigler. Oxo-G was synthesised and fully characterised by C. E. Halbig by SRS, TGA-MS, UV-vis, FT-IR and AFM. The synthesis of oxo-G to yield oxo-G in a highly reproducible way was optimised by C. E. Halbig.
Estimated own contribution	~ 15 %

8.3. High Quality Reduced Graphene Oxide Flakes by Fast Kinetically Controlled and Clean Indirect UV-Induced Radical Reduction

Authors	R. Flynt, W. Knolle, A. Kahnt, C. E. Halbig, S. Eigler, A. Lotnyk, T. Häuptl, A. Prager, B. Abel
Journal	Nanoscale **2016**, 8, 7572-7579
DOI	10.1039/C6NR00156D
Links	http://doi.org/10.1039/c6nr00156d https://pubs.rsc.org/en/content/articlelanding/2016/nr/c6nr00156d#!divAbstract
Contribution	The concept of this manuscript was elaborated by R. Flyunt and Prof. Dr. B. Abel. In the manuscript used oxo-G was synthesised and fully characterised by C. E. Halbig. The reduction was invented and conducted with commercial graphene oxide by the R. Flyunt. C. E. Halbig synthesised oxo-G with an almost intact carbon lattice and applied the novel protocol of reduction. C. E. Halbig analysed the obtained materials using SRS.
Contribution	~ 15 %

8.4. Extending the environmental lifetime of unpacked provskite solar cells through interfacial design

Authors	H. Chen, Y. Hou, C. E. Halbig, S. Chen, H. Zhang, N. Li, F. Guo, X. Tang, N. Gasparini, I. Levchuck, S. Kahmann, C. O. R. Quiroz, A. Osvet, S. Eigler, C. J. Brabec
Journal	J. Mater. Chem A, **2016**, 4, 11604-11610
DOI	10.1039/C6TA03755K
Links	http://doi.org/10.1039/c6ta03755k https://pubs.rsc.org/en/Content/ArticleLanding/2016/TA/C6TA03755K#!divAbstract
Contribution	The concept of this manuscript was elaborated by H. Chen and Prof. Dr. J. Brabec. Oxo-G was synthesised, characterised (SRS, FT-IR, UV-vis, AFM) and transferred to several dry organic solvents by C. E. Halbig. Experimental assistance was given by C. E. Halbig.
Contribution	~ 15 %

8.5. Highly Intact and Pure Oxo-Functionalized Graphene: Synthesis and Electron-Beam-Induced Reduction

Authors	B. Butz, C. Dolle, C. E. Halbig, E. Spiecker, S. Eigler
Journal	Angew. Chem. **2016**, 128 (51), 16003-16006 Angew. Chem. Int. Ed. **2016**, 55 (51), 15771-15774
DOI	10.1002/ange.201608377 10.1002/anie.201608377
Links	https://dx.doi.org/10.1002/ange.201608377 https://dx.doi.org/10.1002/anie.201608377 https://onlinelibrary.wiley.com/doi/full/10.1002/ange.201608377 https://onlinelibrary.wiley.com/doi/full/10.1002/anie.201608377
Contribution	The concept of this manuscript was elaborated by Prof. Dr. B. Butz, Prof. Dr. E. Spiecker and Prof. Dr. S. Eigler. Oxo-G was synthesised by C. E. Halbig using novel reactor design with a novel degree of purity. Particle sizes were analysed by the use of AFM by C. E. Halbig.
Contribution	~ 10 %

8.6. Focused Electron Beam based Direct-Write Fabrication of Graphene and Amorphous Carbon from Oxo-Functionalized Graphene on Silicon Dioxide

Authors	S. Schindler, F. Vollnhals, C. E. Halbig, H. Marbach, H.-P. Steinrück, C. Papp, S. Eigler
Journal	Phys. Chem. Chem. Phys. **2017**, 19, 2683-2686
DOI	10.1039/C6CP08070G
Links	https://doi.org/10.1039/C6CP08070G https://pubs.rsc.org/en/Content/ArticleLanding/2017/CP/C6CP08070G#!divAbstract
Contribution	The concept of this manuscript was elaborated by Prof. Dr. S. Eigler, PD Dr. C. Papp and H.-P. Steinrück. Oxo-G Nanoparticles were synthesised and fully characterised by C. E. Halbig using FT-IR, UV-vis, SRS and TGA-MS.
Contribution	~ 10 %

8.7. Poly(vinylferrocene)-Reduced Graphene Oxide as a High Power / High Capacity Cathodic Battery Material

Authors	S. M. Belade-Mousavi, S. Sadaf, L. Walder, M. Gallei, C. Rüttiger, S. Eigler, C. E. Halbig
Journal	Adv. Energy Mater. **2016**, 6, 1600108
DOI	10.1002/aenm.201600108
Links	https://doi.org/10.1002/aenm.201600108 https://onlinelibrary.wiley.com/doi/full/10.1002/aenm.201600108
Contribution	The concept of this manuscript was elaborated by S. M. Belade-Mousavi. Oxo-G was synthesized and fully characterized by C. E. Halbig and provided for the experiments. C. E. Halbig assisted in Raman analysis.

8.8. Systematic evaluation of different types of graphene oxide in respect to variations in their in-plane modulus

Authors	P. Feicht, R. Siegel, H. Thurm, J. W. Neubauer, M. Seuss, T. Szabo, A. V. Talyzin, C. E. Halbig, S. Eigler, D. A. Kunz, A. Fery, G. Papastavrou, J. Senker, J. Breu
Journal	Carbon **2017**, 114, 700-705
DOI	10.1016/j.carbon.2016.12.065
Links	http://dx.doi.org/10.1016/j.carbon.2016.12.065 https://www.sciencedirect.com/science/article/pii/S0008622316311423?via%3Dihub
Contribution	The concept of this manuscript was elaborated by P. Feicht and Prof. Dr. J. Breu. Oxo-G was synthesized and characterized by FT-IR, UV-vis, SRS and TGA-MS by C. E. Halbig. C. E. Halbig assisted in the evaluation of the recorded Raman data.

List of Abbreviations

2H	hexagonal crystal structure, two layers per unit cell
3R	rhombohedral crystal structure, three layers per unit cell
Å	Ångström
A	area
ac	armchair edge
AFM	atomic force microscopy
*ai*MD	*ab-initio* molecular dynamics
AN	anthracene
ATR	attenuated total reflection
a.u.	arbitrary units
AUC	analytical ultracentrifuge
CNT	carbon nanotubes
CVD	chemical vapour deposition
D_{50}	median value of a particle size distribution
D_F	functional defect
D_V	vacancy defect
DMSO	dimethyl sulfoxide
EA	elemental analysis
eV	electron volt
Fl	fluorescein
FT-IR	fourier-Transformed Infrared Spectroscopy
FWHM	full width at half maximum (cf. Γ)
Γ	full width at half maximum (*cf.* FWHM)
G_1	single layer graphene
GIC	graphite intercalation compound
GIV	Graphit-Interkalationsverbindung
GO	graphene oxide (*cf.* oxo-G)

GrO	graphite oxide
HR-TEM	High-resolution transmission electron microscopy (*cf*. TEM)
I	intensity
I_D/I_G	Intensity ratio of the D and G mode
J	Joule
K	Kelvin
LB	Langmuir-Blodgett (technique)
L_D	mean distance between two defects
m	stacking index
µm	micrometer
MW-CNTs	multi-wall-CNTs
m/z	mass-over-charge ratio
NG	natural Graphite
NMR	nuclear magnetic resonance
ns	nanosecond
Ω	Ohm
OD	oxidative debris
ON	oligonucleotide
oxo-G	oxo-functionalized Graphene (*cf.* GO)
oxo-G-N_3	oxo-functionalized Graphene with additional azide moieties
RCF	relative centrifugation force
recZZ	reconstructed zigzag edge
RPM	revolutions per minute
S (Sv)	Svedberg
SCH	sodium cholate
SDBS	sodium dodecyl benzene sulfonate
SDS	sodium dodecylsulfate

SRS	statistical Raman spectroscopy
SW-CNTs	single-wall CNTs
TEM	transmission electron microscope (*cf.* HR-TEM)
TG	turbostratic Graphite
TGA-MS	thermogravimetric analysis coupled to mass spectrometry
TGA-GC/MS	thermogravimetric analysis coupled to gas chromatography and mass spectrometry
THF	tetrahydrofuran
θ_D	density of defects
θ_{FD}	density of functional defects
θ_{VD}	density of vacancy defects
UV-vis	ultraviolet-visible
W	Watt
x_c	position of the maximum at the x-axis
XPS	X-ray photoelectron spectroscopy
XRPD	X-ray powder diffraction
ZZ	zigzag edge

List of Publications

1. C. E. Halbig, P. Rietsch, S. Eigler
Towards the Synthesis of Graphene Azide from Graphene Oxide
Molecules **2015**, 20 (12), 21050-21057

2. H. Pieper, S. Chercheja, S. Eigler, C. E. Halbig, M. Fillipović, A. Mokhir
Endoperoxides revealed as origin of toxicity of graphene oxide
Toxizität von Graphenoxid: Endoperoxide als Ursache
Angew. Chem. Int. Ed. **2016**, 128 (1), 413-416
Angew. Chem. **2016**, 55 (51), 405-407

3. R. Flynt, W. Knolle, A. Kahnt, C. E. Halbig, S. Eigler, A. Lotnyk, T. Häuptl, A. Prager, B. Abel *High quality reduced graphene oxide flakes by fast kinetically controlled and clean indirect UV-induced radical reduction*
Nanoscale **2016**, 8 (14), 7572-7579

4. H. Chen, Y. Hou, C. E. Halbig, S. Chen, H. Zhang, N. Li, F. Guo, X. Tang, N. Gasparini, I. Levchuk, S. Kahmann, C. O. R. Quiroz, A. Osvet, S. Eigler, C. J. Brabec
Extending the environmental lifetime of unpackaged perovskite solar cells through interfacial design
J. Mater. Chem. A **2016**, 4 (30), 11604-11610

5. S. Schindler, F. Vollnhals, C. E. Halbig, H. Marbach, H.-P. Steinrück, C. Papp, S. Eigler
Focused Electron Beam based Direct-Write Fabrication of Graphene and Amorphous Carbon from Oxo-Functionalized Graphene on Silicon Dioxide
Phys. Chem. Chem. Phys. **2017**, 19 (4), 2683-2686

6. C. E. Halbig, T. J. Nacken, J. Walter, C. Damm, S. Eigler, W. Peukert
Quantitative investigation of the fragmentation process and defect density evolution of oxo-functionalized graphene due to ultrasonication and milling
Carbon **2016**, 96 (14), 897-903

7. S. M. Belade-Mousavi, S. Sadaf, L. Walder, M. Gallei, C. Rüttiger, S. Eigler, C. E. Halbig
Poly(vinylferrocene) - Reduced Graphene Oxide as a High Power / High Capacity Cathodic Battery Material
Adv. Energy Mater. **2016**, 6 (12), 1600108

8. A. Naumov, F. Grote, M. Overgaard, A. Roth, C. E. Halbig, K. Nørgaard, D. M. Guldi, S. Eigler
Graphene Oxide: A One- versus Two-Component Material
J. Am. Chem. Soc. **2016**, 138 (36), 11445–11448

9. H. Pieper, C. E. Halbig, L. Kovbasyuk, S. Eigler, A. Mokhir
Oxo-functionalized graphene as cell membrane carrier of nucleic acid probes controlled by aging
Chem. Eur. J. **2016**, 22 (42), 15389-15395

10. B. Butz, C. Dolle, C. E. Halbig, E. Spiecker, S. Eigler
Highly Intact and Pure Oxo-Functionalized Graphene: Synthesis and Electron-Beam-Induced Reduction
Nahezu vollständig intaktes und sauberes oxo-functionalisiertes Graphen – Synthese und elektronenstrahlinduzierte Reduktion
Angew. Chem. **2016**, 128 (51), 16003-16006
Angew. Chem. Int. E. **2016**, 55 (51), 15771-15774

11. P. Feicht, R. Siegel, H. Thurm, J. W. Neubauer, M. Seuss, T. Szabo, A. V. Talyzin, C. E. Halbig, S. Eigler, D. A. Kunz, A. Fery, G. Papastavrou, J. Senker, J. Breu
Systematic evaluation of different types of graphene oxide in respect to variations in their in-plane modulus
Carbon **2017**, 114, 700-705

12. T. J. Nacken, C. E. Halbig, S. Wawra, C. Damm, S. Romeis, J. Walter, M. J. Tehrani, Y. Ishii, S. Eigler, W. Peukert
Structural factors controlling size reduction of graphene oxide in liquid processing
Carbon ***2017****, 125, 360-369*

13. S. Seiler, C. E. Halbig, F. Grote, P. Rietsch, F. Börrnert, U. Kaiser, B. Meyer,* and S. Eigler*
Effect of friction on oxidative graphite intercalation and high-quality graphene formation
Nat. Commun. ***2018****, 9 (1), 836*

14. C. E. Halbig, O. Martin, F. Hauke, S. S. Eigler, A. Hirsch
Oxo-Functionalized Graphene - A Versatile Precursor for Alkylated Graphene Sheets by Reductive Functionalization.
Chem. Eur. J. ***2018****, 24,* 13348-13354

15. C. E. Halbig, R. Lasch, J. Krüll, A. Pirzer, Z.P. Wang, M. R. Heinrich, S. Eigler
Selective functionalization of graphene at defect activated sites by arylazocarboxylic tert-butyl esters
Angew. Chem., submitted **09/2018**

References

[1] S. Seiler, C. E. Halbig, F. Grote, P. Rietsch, F. Börrnert, U. Kaiser, B. Meyer, S. Eigler, *Nature Communications* **2018**, *9*.

[2] J. P. Rourke, P. A. Pandey, J. J. Moore, M. Bates, I. A. Kinloch, R. J. Young, N. R. Wilson, *Angew. Chem. Int. Ed.* **2011**, *50*, 3173-3177.

[3] A. M. Dimiev, T. A. Polson, *Carbon* **2015**, *93*, 544-554.

[4] A. Naumov, F. Grote, M. Overgaard, A. Roth, C. E. Halbig, K. Norgaard, D. M. Guldi, S. Eigler, *J. Am. Chem. Soc.* **2016**, *138*, 11445-11448.

[5] aC. E. Halbig, T. J. Nacken, J. Walter, C. Damm, S. Eigler, W. Peukert, *Carbon* **2016**, *96*, 897-903; bT. J. Nacken, C. E. Halbig, S. E. Wawra, C. Damm, S. Romeis, J. Walter, M. J. Tehrani, Y. C. Hu, Y. Ishii, S. Eigler, W. Peukert, *Carbon* **2017**, *125*, 360-369.

[6] H. Pieper, S. Chercheja, S. Eigler, C. E. Halbig, M. R. Filipovic, A. Mokhir, *Angew. Chem. Int. Ed.* **2016**, *55*, 405-407.

[7] H. Pieper, C. E. Halbig, L. Kovbasyuk, M. R. Filipovic, S. Eigler, A. Mokhir, *Chem. Eur. J.* **2016**, *22*, 15389-15395.

[8] C. E. Halbig, P. Rietsch, S. Eigler, *Molecules* **2015**, *20*, 21050-21057.

[9] C. E. Halbig, O. Martin, F. Hauke, S. Eigler, A. Hirsch, *Chem. Eur. J.* **2018**.

[10] S. Seiler, C. E. Halbig, F. Grote, P. Rietsch, F. Borrnert, U. Kaiser, B. Meyer, S. Eigler, *Nat. Commun.* **2018**, *9*, 836.

[11] aF. Bonaccorso, L. Colombo, G. Yu, M. Stoller, V. Tozzini, A. C. Ferrari, R. S. Ruoff, V. Pellegrini, *Science* **2015**, *347*, 1246501; bH. Chen, Y. Hou, C. E. Halbig, S. Chen, H. Zhang, N. Li, F. Guo, X. Tang, N. Gasparini, I. Levchuk, S. Kahmann, C. O. Ramirez Quiroz, A. Osvet, S. Eigler, C. J. Brabec, *J. Mater. Chem. A* **2016**, *4*, 11604-11610; cD. Singh, S. K. Gupta, Y. Sonvane, I. Lukačević, *Journal of Materials Chemistry C* **2016**, *4*, 6386-6390; dZ. Wang, S. Eigler, Y. Ishii, Y. Hu, C. Papp, O. Lytken, H.-P. Steinrück, M. Halik, *Journal of Materials Chemistry C* **2015**, *3*, 8595-8604; eM. H. Overgaard, M. Kühnel, R. Hvidsten, S. V. Petersen, T. Vosch, K. Nørgaard, B. W. Laursen, *Adv. Mater. Technol.* **2017**, *2*, 1700011.

[12] aA. K. Geim, K. S. Novoselov, *Nat Mater* **2007**, *6*, 183-191; bK. S. Novoselov, A. K. Geim, S. V. Morozov, D. Jiang, Y. Zhang, S. V. Dubonos, I. V. Grigorieva, A. A. Firsov, *Science* **2004**, *306*, 666-669.

[13] L. Mohapatra, K. Parida, *J. Mater. Chem. A* **2016**, *4*, 10744-10766.

[14] Y. P. Venkata Subbaiah, K. J. Saji, A. Tiwari, *Adv. Funct. Mater.* **2016**, *26*, 2046-2069.

[15] Y. Zhao, Y. Chen, Y.-H. Zhang, S.-F. Liu, *Mater. Chem. Phys.* **2017**, *189*, 215-229.

[16] M. Pumera, Z. Sofer, *Adv. Mater.* **2017**, *29*.

[17] I. Khan, K. Saeed, *Carbon letters* **2013**, *14*, 131-144.

[18] S. F. A. Acquah, A. V. Penkova, D. A. Markelov, A. S. Semisalova, B. E. Leonhardt, J. M. Magi, *ECS Journal of Solid State Science and Technology* **2017**, *6*, M3155-M3162.

[19] aC. Tan, X. Cao, X. J. Wu, Q. He, J. Yang, X. Zhang, J. Chen, W. Zhao, S. Han, G. H. Nam, M. Sindoro, H. Zhang, *Chem. Rev.* **2017**, *117*, 6225-6331; bF. Perrozzi, S. Prezioso, L. Ottaviano, *Journal of physics. Condensed matter : an Institute of Physics journal* **2015**, *27*, 013002; cD. R. Dreyer, S. Park, C. W. Bielawski, R. S. Ruoff, *Chem. Soc. Rev.* **2010**, *39*, 228-240.

[20] aQ.-D. Yang‡, J. Li, Y. Cheng, H.-W. Li, Z. Guan, B. Yu, S.-W. Tsang, *J. Mater. Chem. A* **2017**, *5*, 9852-9858; bJ. Liu, L. Cui, D. Losic, *Acta Biomater.* **2013**, *9*, 9243-9257; cS. Homaeigohar, M. Elbahri, *Npg Asia Materials* **2017**, *9*; dX. Y. Yang, Y. S. Wang, X. Huang, Y. F. Ma, Y. Huang, R. C. Yang, H. Q. Duan, Y. S. Chen, *J. Mater. Chem.* **2011**, *21*, 3448-3454; eS. Bak, D. Kim, H. Lee, *Current Applied Physics* **2016**, *16*, 1192-1201; fJ.-S. Yeo, R. Kang, S. Lee, Y.-J. Jeon, N. Myoung, C.-L. Lee, D.-Y. Kim, J.-M. Yun, Y.-H. Seo, S.-S. Kim, S.-I. Na, *Nano Energy* **2015**, *12*, 96-104.

[21] aA. Mnyusiwalla, A. S. Daar, P. A. Singer, *Nanotechnology* **2003**, *14*, R9-R13; bA. Nordmann, A. Rip, *Nat Nanotechnol* **2009**, *4*, 273-274.
[22] aE. Riedel, *Allgemeine und anorganische Chemie*, 8 ed., De Gruyter, Berlin; New York, **2010**; bN. Wiberg, G. Fischer, A. F. Holleman, E. Wiberg, N. Wiberg, *Lehrbuch der Anorganischen Chemie*, 102 ed., de Gruyter, Berlin, New York, **2008**.
[23] G. Audi, O. Bersillon, J. Blachot, A. H. Wapstra, *Nucl. Phys. A* **2003**, *729*, 3-128.
[24] C. E. Mortimer, J. Beck, U. Müller, *Chemie : das Basiswissen der Chemie*, Thieme, Stuttgart [u.a.], **2015**.
[25] J. Fessmann, H. Orth, *Angewandte Chemie und Umwelttechnik für Ingenieure : Handbuch für Studium und betriebliche Praxis*, 2 ed., Ecomed, Landsberg, **2002**.
[26] aA. A. Balandin, *Nat Mater* **2011**, *10*, 569-581; bS. Kidalov, F. Shakhov, *Materials* **2009**, *2*, 2467-2495.
[27] aT. Evans, P. F. James, *Proceedings of the Royal Society A: Mathematical, Physical and Engineering Sciences* **1964**, *277*, 260-269; bP. John, N. Polwart, C. E. Troupe, J. I. B. Wilson, *Diamond Relat. Mater.* **2002**, *11*, 861-866.
[28] A. Ambrosi, C. K. Chua, B. Khezri, Z. Sofer, R. D. Webster, M. Pumera, *Proc. Nat. Acad. Sci. USA* **2012**, *109*, 12899-12904.
[29] A. R. Golkarian, M. Jabbarzadeh, *Computational Materials Science* **2013**, *74*, 138-142.
[30] G. E. Bacon, *Acta Crystallographica* **1951**, *4*, 558-561.
[31] aA. C. Ferrari, D. M. Basko, *Nat Nanotechnol* **2013**, *8*, 235-246; bD. D. L. Chung, *J. Mater. Sci.* **2002**, *37*, 1475-1489; cN. V. Kozhemyakina, S. Eigler, R. E. Dinnebier, A. Inayat, W. Schwieger, A. Hirsch, *Fuller. Nanotub. Car. N.* **2013**, *21*, 804-823.
[32] J. K. Lee, S. C. Lee, J. P. Ahn, S. C. Kim, J. I. Wilson, P. John, *The Journal of chemical physics* **2008**, *129*, 234709.
[33] aA. A. Balandin, S. Ghosh, W. Bao, I. Calizo, D. Teweldebrhan, F. Miao, C. N. Lau, *Nano Lett.* **2008**, *8*, 902-907; bG. Fugallo, A. Cepellotti, L. Paulatto, M. Lazzeri, N. Marzari, F. Mauri, *Nano Lett.* **2014**, *14*, 6109-6114; cM. Li, H. Zhou, Y. Zhang, Y. Liao, H. Zhou, *Carbon* **2018**, *130*, 295-303; dF. Banhart, J. Kotakoski, A. V. Krasheninnikov, *ACS Nano* **2011**, *5*, 26-41.
[34] C. P. Ewels, R. H. Telling, A. A. El-Barbary, M. I. Heggie, P. R. Briddon, *Phys. Rev. Lett.* **2003**, *91*, 025505.
[35] R. Wakeford, *J Radiol Prot* **2007**, *27*, 211-215.
[36] aK. S. Novoselov, D. Jiang, F. Schedin, T. J. Booth, V. V. Khotkevich, S. V. Morozov, A. K. Geim, *Proc. Nat. Acad. Sci. USA* **2005**, *102*, 10451-10453; bR. R. Nair, P. Blake, A. N. Grigorenko, K. S. Novoselov, T. J. Booth, T. Stauber, N. M. Peres, A. K. Geim, *Science* **2008**, *320*, 1308.
[37] P. Y. Huang, C. S. Ruiz-Vargas, A. M. v. d. Zande, W. S. Whitney, M. P. Levendorf, J. W. Kevek, S. Garg, J. S. Alden, C. J. Hustedt, Y. Zhu, J. Park, P. L. McEuen, D. A. Muller, *Nature* **2011**, *469*, 389-393.
[38] J. Kotakoski, A. V. Krasheninnikov, U. Kaiser, J. C. Meyer, *Phys. Rev. Lett.* **2011**, *106*, 105505.
[39] aP. Koskinen, S. Malola, H. Häkkinen, *Phys. Rev. B* **2009**, *80*; bK. He, A. W. Robertson, Y. Fan, C. S. Allen, Y. C. Lin, K. Suenaga, A. I. Kirkland, J. H. Warner, *ACS Nano* **2015**, *9*, 4786-4795.
[40] aM. M. A. Rafique, J. Iqbal, *Journal of Encapsulation and Adsorption Sciences* **2011**, *01*, 29-34; bJ. R. Sanchez-Valencia, T. Dienel, O. Groning, I. Shorubalko, A. Mueller, M. Jansen, K. Amsharov, P. Ruffieux, R. Fasel, *Nature* **2014**, *512*, 61-64.
[41] B. Liu, H. Jiang, A. V. Krasheninnikov, A. G. Nasibulin, W. Ren, C. Liu, E. I. Kauppinen, H. M. Cheng, *Small* **2013**, *9*, 1379-1386.
[42] aM. L. Avramescu, P. E. Rasmussen, M. Chenier, *J Anal Methods Chem* **2016**, *2016*, 3834292; bJ.-H. Lim, V. G. Bairi, A. Fong, *Mater. Chem. Phys.* **2017**, *198*, 324-330.
[43] aH. Z. Geng, X. B. Zhang, S. H. Mao, A. Kleinhammes, H. Shimoda, Y. Wu, O. Zhou, *Chem. Phys. Lett.* **2004**, *399*, 109-113; bL. Jiao, L. Zhang, X. Wang, G. Diankov, H. Dai, *Nature* **2009**, *458*, 877-880.

[44] aC. Mattevi, H. Kim, M. Chhowalla, *J. Mater. Chem.* **2011**, *21*, 3324-3334; bJ. N. Coleman, *Acc. Chem. Res.* **2013**, *46*, 14-22; cK. R. Paton, E. Varrla, C. Backes, R. J. Smith, U. Khan, A. O'Neill, C. Boland, M. Lotya, O. M. Istrate, P. King, T. Higgins, S. Barwich, P. May, P. Puczkarski, I. Ahmed, M. Moebius, H. Pettersson, E. Long, J. Coelho, S. E. O'Brien, E. K. McGuire, B. M. Sanchez, G. S. Duesberg, N. McEvoy, T. J. Pennycook, C. Downing, A. Crossley, V. Nicolosi, J. N. Coleman, *Nat Mater* **2014**, *13*, 624-630; dS. Eigler, *Chem. Eur. J.* **2016**, *22*, 7012-7027.

[45] K. S. Novoselov, A. K. Geim, S. V. Morozov, D. Jiang, Y. Zhang, S. V. Bubonos, I. V. Grigorieva, A. A. Firsov, *Science* **2004**, *306*, 666-669.

[46] aL. Huang, Q. H. Chang, G. L. Guo, Y. Liu, Y. Q. Xie, T. Wang, B. Ling, H. F. Yang, *Carbon* **2012**, *50*, 551-556; bZ. Chen, W. Ren, B. Liu, L. Gao, S. Pei, Z.-S. Wu, J. Zhao, H.-M. Cheng, *Carbon* **2010**, *48*, 3543-3550; cK. Yan, L. Fu, H. Peng, Z. Liu, *Acc. Chem. Res.* **2013**, *46*, 2263-2274; dW. A. de Heer, C. Berger, X. Wu, P. N. First, E. H. Conrad, X. Li, T. Li, M. Sprinkle, J. Hass, M. L. Sadowski, M. Potemski, G. Martinez, *Solid State Commun.* **2007**, *143*, 92-100.

[47] J. H. Lee, E. K. Lee, W. J. Joo, Y. Jang, B. S. Kim, J. Y. Lim, S. H. Choi, S. J. Ahn, J. R. Ahn, M. H. Park, C. W. Yang, B. L. Choi, S. W. Hwang, D. Whang, *Science* **2014**, *344*, 286-289.

[48] aM. Lotya, P. J. King, U. Khan, S. De, J. N. Coleman, *ACS Nano* **2010**, *4*, 3155-3162; bU. Khan, A. O'Neill, M. Lotya, S. De, J. N. Coleman, *Small* **2010**, *6*, 864-871; cJ. M. Englert, J. Röhrl, C. D. Schmidt, R. Graupner, M. Hundhausen, F. Hauke, A. Hirsch, *Adv. Mater.* **2009**, *21*, 4265-4269.

[49] C. Knieke, A. Berger, M. Voigt, R. N. K. Taylor, J. Rohrl, W. Peukert, *Carbon* **2010**, *48*, 3196-3204.

[50] Z. Shen, J. Li, M. Yi, X. Zhang, S. Ma, *Nanotechnology* **2011**, *22*, 365306.

[51] aW. S. Hummers, *Pereparation of graphitic acid*, US2798878, **1957**; bP. Vecera, J. Holzwarth, K. F. Edelthalhammer, U. Mundloch, H. Peterlik, F. Hauke, A. Hirsch, *Nat. Commun.* **2016**, *7*, 12411; cS. Eigler, M. Enzelberger-Heim, S. Grimm, P. Hofmann, W. Kroener, A. Geworski, C. Dotzer, M. Rockert, J. Xiao, C. Papp, O. Lytken, H. P. Steinruck, P. Muller, A. Hirsch, *Adv. Mater.* **2013**, *25*, 3583-3587; dS. Eigler, A. Hirsch, *Angew. Chem. Int. Ed.* **2014**, *53*, 7720-7738; eG. Ruess, F. Vogt, *Monatshefte f[illegible]r Chemie* **1948**, *78*, 222-242; fH. P. Boehm, A. Clauss, G. O. Fischer, U. Hofmann, *Z. Naturforsch.* **1962**, *17b*, 150-153; gH. P. Boehm, A. Clauss, G. O. Fischer, U. Hofmann, *Z. Anorg. Allg. Chem.* **1962**, *316*, 119-127.

[52] aL. M. Viculis, J. J. Mack, O. M. Mayer, H. T. Hahn, R. B. Kaner, *J. Mater. Chem.* **2005**, *15*, 974-978; bM. S. Dresselhaus, G. Dresselhaus, *Adv. Phys.* **2006**, *30*, 139-326; cP. Feicht, J. Breu, *Z. Anorg. Allg. Chem.* **2015**, *641*, 1093-1098; dW. Rüdorff, H. Schulz, *Z. Anorg. Allg. Chem.* **1940**, *245*, 121-156.

[53] H. Moriwake, A. Kuwabara, C. A. J. Fisher, Y. Ikuhara, *RSC Adv.* **2017**, *7*, 36550-36554.

[54] I. Krossing, Y. Steudel, R. Steudel, *Chemistry of Non-metals*, **2008**.

[55] aS. Eigler, *Chem. Commun.* **2015**, *51*, 3162-3165; bN. I. Kovtyukhova, P. J. Ollivier, B. R. Martin, T. E. Mallouk, S. A. Chizhik, E. V. Buzaneva, A. D. Gorchinskiy, *Chem. Mater.* **1999**, *11*, 771-778.

[56] W. Rüdorff, U. Hofmann, *Z. Anorg. Allg. Chem.* **1938**, *238*, 1-50.

[57] H. P. Boehm, R. Setton, E. Stumpp, *Pure Appl. Chem.* **1994**, *66*, 1893-1901.

[58] aJ. Sun, N. Yang, Z. Sun, M. Zeng, L. Fu, C. Hu, S. Hu, *ACS Appl. Mater. Interfaces* **2015**, *7*, 21356-21363; bD. C. Marcano, D. V. Kosynkin, J. M. Berlin, A. Sinitskii, Z. Sun, A. Slesarev, L. B. Alemany, W. Lu, J. M. Tour, *ACS Nano* **2010**, *4*, 4806-4814; cJ. G. Hooley, *Carbon* **1972**, *10*, 155-163.

[59] aL. Staudenmaier, *Ber. Dtsch. Chem. Ges.* **1898**, *31*, 1481-1487; bH. Moissan, *Compte-Rendu des Séances de l'Académie des Sciences* **1895**, *121*, 538-540.

[60] F. Lévy, *Intercalated Layered Materials*, Springer Netherlands, Dordrecht, **1979**.

[61] aA. Lerf, H. Y. He, M. Forster, J. Klinowski, *J. Phys. Chem. B* **1998**, *102*, 4477-4482; bW. S. Hummers, R. E. Offeman, *J. Am. Chem. Soc.* **1958**, *80*, 1339-1339.

[62] aJ. M. Englert, C. Dotzer, G. Yang, M. Schmid, C. Papp, J. M. Gottfried, H.-P. Steinrück, E. Spiecker, F. Hauke, A. Hirsch, *Nature Chem.* **2011**, *3*, 279-286; bP. Vecera, K. Edelthalhammer, F. Hauke, A. Hirsch, *Phys. Status Solidi B* **2014**, *251*, 2536-2540; cG. Abellan, M. Schirowski, K. F. Edelthalhammer, M. Fickert, K. Werbach, H. Peterlik, F. Hauke, A. Hirsch, *J. Am. Chem. Soc.* **2017**,

139, 5175-5182; dR. A. Schäfer, J. M. Englert, P. Wehrfritz, W. Bauer, F. Hauke, T. Seyller, A. Hirsch, *Angew. Chem.* **2013**, *125*, 782-786.
[63] R. A. Schäfer, J. M. Englert, P. Wehrfritz, W. Bauer, F. Hauke, T. Seyller, A. Hirsch, *Angew. Chem. Int. Ed.* **2013**, *52*, 754-757.
[64] B. C. Brodie, *Proceedings Proceedings of the Royal Society of Londonof the Royal Society of London* **1859**, *10*, 11-12.
[65] G. Charpy, *C. R. Hebd. Séances Acad. Sci.* **1909**, *148*, 920-923.
[66] W. Luzi, *Ber. Dtsch. Chem. Ges.* **1891**, *24*, 4085-4095.
[67] A. M. Dimiev, S. M. Bachilo, R. Saito, J. M. Tour, *ACS Nano* **2012**, *6*, 7842-7849.
[68] aS. Eigler, C. Dotzer, F. Hof, W. Bauer, A. Hirsch, *Chem. Eur. J.* **2013**, *19*, 9490-9496; bS. Eigler, C. Dotzer, A. Hirsch, *Carbon* **2012**, *50*, 3666-3673.
[69] aR. Peierls, *Ann. Henri Poincare* **1935**, *5*, 177-222; bL. D. Landau, *Phys. Z . Sowjetunion* **1937**, *11*, 26-35.
[70] J. Chen, Y. Zhang, M. Zhang, B. Yao, Y. Li, L. Huang, C. Li, G. Shi, *Chemical Science* **2016**, *7*, 1874-1881.
[71] aS. Eigler, S. Grimm, A. Hirsch, *Chem. Eur. J.* **2014**, *20*, 984-989; bF. Grote, C. Gruber, F. Borrnert, U. Kaiser, S. Eigler, *Angew. Chem. Int. Ed.* **2017**, *56*, 9222-9225.
[72] P. Feicht, D. A. Kunz, A. Lerf, J. Breu, *Carbon* **2014**, *80*, 229-234.
[73] P. Feicht, R. Siegel, H. Thurn, J. W. Neubauer, M. Seuss, T. Szabo, A. V. Talyzin, C. E. Halbig, S. Eigler, D. A. Kunz, A. Fery, G. Papastavrou, J. Senker, J. Breu, *Carbon* **2017**, *114*, 700-705.
[74] S. Zhou, A. Bongiorno, *Sci. Rep.* **2013**, *3*, 2484.
[75] B. Butz, C. Dolle, C. E. Halbig, E. Spiecker, S. Eigler, *Angew. Chem. Int. Ed.* **2016**, *55*, 15771-15774.
[76] aS. Eigler, S. Grimm, F. Hof, A. Hirsch, *J. Mater. Chem. A* **2013**, *1*, 11559; bS. Eigler, C. Dotzer, A. Hirsch, M. Enzelberger, P. Müller, *Chem. Mater.* **2012**, *24*, 1276-1282; cW. C. Hou, I. Chowdhury, D. G. Goodwin, Jr., W. M. Henderson, D. H. Fairbrother, D. Bouchard, R. G. Zepp, *Environ Sci Technol* **2015**, *49*, 3435-3443.
[77] A. M. Dimiev, L. B. Alemany, J. M. Tour, *ACS Nano* **2013**, *7*, 576-588.
[78] aR. Kurapati, J. Russier, M. A. Squillaci, E. Treossi, C. Menard-Moyon, A. E. Del Rio-Castillo, E. Vazquez, P. Samori, V. Palermo, A. Bianco, *Small* **2015**, *11*, 3985-3994; bR. Kurapati, S. P. Mukherjee, C. Martín, G. Bepete, E. Vázquez, A. Pénicaud, B. Fadeel, A. Bianco, *Angew. Chem.* **2018**.
[79] aS. T. Yang, Y. Chang, H. Wang, G. Liu, S. Chen, Y. Wang, Y. Liu, A. Cao, *J Colloid Interface Sci* **2010**, *351*, 122-127; bW. Peng, H. Li, Y. Liu, S. Song, *J. Mol. Liq.* **2017**, *230*, 496-504.
[80] S. Eigler, Y. Hu, Y. Ishii, A. Hirsch, *Nanoscale* **2013**, *5*, 12136-12139.
[81] S. Eigler, S. Grimm, M. Enzelberger-Heim, P. Muller, A. Hirsch, *Chem. Commun.* **2013**, *49*, 7391-7393.
[82] P. Feicht, S. Eigler, *ChemNanoMat* **2018**, *4*, 244-252.
[83] aS. H. Huh, in *Physics and Applications of Graphene - Experiments* (Ed.: S. Mikhailov), InTech, **2011**, pp. 73-90; bX. Gao, J. Jang, S. Nagase, *J. Phys. Chem. C* **2010**, *114*, 832-842; cW. Chen, L. Yan, P. R. Bangal, *Carbon* **2010**, *48*, 1146-1152; dY. Shao, J. Wang, M. Engelhard, C. Wang, Y. Lin, *J. Mater. Chem.* **2010**, *20*, 743-748; eS. Y. Toh, K. S. Loh, S. K. Kamarudin, W. R. W. Daud, *Chem. Eng. J.* **2014**, *251*, 422-434.
[84] S. Eigler, *Phys. Chem. Chem. Phys.* **2014**, *16*, 19832-19835.
[85] aS. F. Pei, H. M. Cheng, *Carbon* **2012**, *50*, 3210-3228; bJ. Zhang, H. Yang, G. Shen, P. Cheng, J. Zhang, S. Guo, *Chem. Commun.* **2010**, *46*, 1112-1114; cL. G. Guex, B. Sacchi, K. F. Peuvot, R. L. Andersson, A. M. Pourrahimi, V. Strom, S. Farris, R. T. Olsson, *Nanoscale* **2017**, *9*, 9562-9571; dC. K. Chua, M. Pumera, *Chem. Soc. Rev.* **2014**, *43*, 291-312; eS. Thakur, N. Karak, *Carbon* **2015**, *94*, 224-242.
[86] S. Grimm, M. Schweiger, S. Eigler, J. Zaumseil, *J. Phys. Chem. C* **2016**, *120*, 3036-3041.
[87] K. Zhang, L. Mao, L. L. Zhang, H. S. On Chan, X. S. Zhao, J. Wu, *J. Mater. Chem.* **2011**, *21*, 7302.

[88] L. G. Cancado, A. Jorio, E. H. Ferreira, F. Stavale, C. A. Achete, R. B. Capaz, M. V. Moutinho, A. Lombardo, T. S. Kulmala, A. C. Ferrari, *Nano Lett.* **2011**, *11*, 3190-3196.
[89] M. M. Lucchese, F. Stavale, E. H. M. Ferreira, C. Vilani, M. V. O. Moutinho, R. B. Capaz, C. A. Achete, A. Jorio, *Carbon* **2010**, *48*, 1592-1597.
[90] aE. H. Martins Ferreira, M. V. O. Moutinho, F. Stavale, M. M. Lucchese, R. B. Capaz, C. A. Achete, A. Jorio, *Phys. Rev. B* **2010**, *82*, 125429–125437; bL. G. Cançado, K. Takai, T. Enoki, M. Endo, Y. A. Kim, H. Mizusaki, N. L. Speziali, A. Jorio, M. A. Pimenta, *Carbon* **2008**, *46*, 272-275.
[91] aA. Das, S. Pisana, B. Chakraborty, S. Piscanec, S. K. Saha, U. V. Waghmare, K. S. Novoselov, H. R. Krishnamurthy, A. K. Geim, A. C. Ferrari, A. K. Sood, *Nat Nanotechnol* **2008**, *3*, 210-215; bM. Kalbac, A. Reina-Cecco, H. Farhat, J. Kong, L. Kavan, M. S. Dresselhaus, *ACS Nano* **2010**, *4*, 6055-6063.
[92] aM. Huang, H. Yan, T. F. Heinz, J. Hone, *Nano Lett.* **2010**, *10*, 4074-4079; bD. Yoon, Y. W. Son, H. Cheong, *Phys. Rev. Lett.* **2011**, *106*, 155502; cM. Mohr, J. Maultzsch, C. Thomsen, *Phys. Rev. B* **2010**, *82*; dH. Lin, A. Schilo, A. R. Kamoka, N. Severin, I. M. Sokolov, J. P. Rabe, *Phys. Rev. B* **2017**, *95*.
[93] aT. Gokus, R. R. Nair, A. Bonetti, M. Bohmler, A. Lombardo, K. S. Novoselov, A. K. Geim, A. C. Ferrari, A. Hartschuh, *ACS Nano* **2009**, *3*, 3963-3968; bP. Vecera, S. Eigler, M. Kolesnik-Gray, V. Krstic, A. Vierck, J. Maultzsch, R. A. Schafer, F. Hauke, A. Hirsch, *Sci. Rep.* **2017**, *7*, 45165.
[94] P. Vecera, J. C. Chacón-Torres, T. Pichler, S. Reich, H. R. Soni, A. Görling, K. Edelthalhammer, H. Peterlik, F. Hauke, A. Hirsch, *Nature Commun.* **2017**, *8*, 15192.
[95] aA. K. Gupta, T. J. Russin, H. R. G. rrez, P. C. Eklund, *Nano Lett.* **2009**, *3*, 45–52; bC. Casiraghi, A. Hartschuh, H. Qian, S. Piscanec, C. Georgi, A. Fasoli, K. S. Novoselov, D. M. Basko, A. C. Ferrari, *Nano Lett.* **2009**, *9*, 1433-1441.
[96] L. M. Malard, M. A. Pimenta, G. Dresselhaus, M. S. Dresselhaus, *Physics Reports* **2009**, *473*, 51-87.
[97] A. C. Ferrari, J. C. Meyer, V. Scardaci, C. Casiraghi, M. Lazzeri, F. Mauri, S. Piscanec, D. Jiang, K. S. Novoselov, S. Roth, A. K. Geim, *Phys. Rev. Lett.* **2006**, *97*, 187401.
[98] F. Tuinstra, J. L. Koenig, *J. Phys. Chem.* **1970**, *53*, 1126-1130.
[99] R. Mecke, *Z. Phys. Chem.* **1932**, *16B*.
[100] J. Clayden, N. Greeves, S. G. Warren, *Organische Chemie*, 2 ed., Springer, Berlin, **2017**.
[101] C. Zhang, D. M. Dabbs, L.-M. Liu, I. A. Aksay, R. Car, A. Selloni, *J. Phys. Chem. C* **2015**, *119*, 18167-18176.
[102] G. Eda, Y. Y. Lin, C. Mattevi, H. Yamaguchi, H. A. Chen, I. S. Chen, C. W. Chen, M. Chhowalla, *Adv. Mater.* **2010**, *22*, 505-509.
[103] Z. Çiplak, N. Yildiz, A. Çalimli, *Fuller. Nanotub. Car. N.* **2014**, *23*, 361-370.
[104] aU. Hofmann, A. Frenzel, *Ber. Dtsch. Chem. Ges.* **1930**, *63*, 1248-1262; bW. Scholz, H. P. Boehm, *Z. Anorg. Allg. Chem.* **1969**, *369*, 327-340; cB. Westenfelder, J. C. Meyer, J. Biskupek, S. Kurasch, F. Scholz, C. E. Krill, 3rd, U. Kaiser, *Nano Lett.* **2011**, *11*, 5123-5127.
[105] aJ. Walter, T. J. Nacken, C. Damm, T. Thajudeen, S. Eigler, W. Peukert, *Small* **2015**, *11*, 814-825; bJ. L. Cole, J. W. Lary, P. M. T, T. M. Laue, *Methods Cell Biol* **2008**, *84*, 143-179.
[106] T. J. Nacken, C. Damm, J. Walter, A. Rüger, W. Peukert, *RSC Adv.* **2015**, *5*, 57328-57338.
[107] aA. Detrich, A. Deak, E. Hild, A. L. Kovacs, Z. Horvolgyi, *Langmuir* **2010**, *26*, 2694-2699; bX. Li, G. Zhang, X. Bai, X. Sun, X. Wang, E. Wang, H. Dai, *Nat Nanotechnol* **2008**, *3*, 538-542.
[108] H.-J. Butt, K. Graf, M. Kappl, *Physics and Chemistry of Interfaces*, Wiley-VCH Verlag & Co. KGaA, Weinheim, **2003**.
[109] A. M. Dimiev, G. Ceriotti, N. Behabtu, D. Zakhidov, M. Pasquali, R. Saito, J. M. Tour, *ACS Nano* **2013**, *7*, 2773-2780.
[110] X. Fan, W. Peng, Y. Li, X. Li, S. Wang, G. Zhang, F. Zhang, *Adv. Mater.* **2008**, *20*, 4490-4493.
[111] aX. Zhou, Z. Liu, *Chem. Commun.* **2010**, *46*, 2611-2613; bX. Sun, D. Luo, J. Liu, D. G. Evans, *ACS Nano* **2010**, *4*, 3381-3389; cC.-Y. Su, Y. Xu, W. Zhang, J. Zhao, X. Tang, C.-H. Tsai, L.-J. Li, *Chem.*

Mater. **2009**, *21*, 5674-5680; dV. C. Tung, M. J. Allen, Y. Yang, R. B. Kaner, *Nat Nanotechnol* **2009**, *4*, 25-29.

[112] G. Goncalves, M. Vila, I. Bdikin, A. de Andres, N. Emami, R. A. Ferreira, L. D. Carlos, J. Gracio, P. A. Marques, *Sci. Rep.* **2014**, *4*, 6735.

[113] aZ. Liu, J. T. Robinson, X. Sun, H. Dai, *J. Am. Chem. Soc.* **2008**, *130*, 10876-10877; bX. Sun, Z. Liu, K. Welsher, J. T. Robinson, A. Goodwin, S. Zaric, H. Dai, *Nano Res.* **2008**, *1*, 203-212; cL. Feng, Z. Liu, *Nanomedicine* **2011**, *6*, 317-324.

[114] D. Bitounis, H. Ali-Boucetta, B. H. Hong, D. H. Min, K. Kostarelos, *Adv. Mater.* **2013**, *25*, 2258-2268.

Acknowledgements

Here, I want to thank my parents Rosemarie and Adolf Halbig as well as all my four brothers for supporting me throughout my whole studies to follow my interests in chemistry. They always took care of me and listened to me in both good and in bad times.

A special thanks to my supervisor Prof. Dr. Siegfried Eigler, who believed in my abilities and gave me the opportunity to graduate under his supervision in his workgroup. Also, I want to thank all my colleagues from FAU Erlangen-Nürnberg and FU Berlin, especially Frank Hauke, Thomas Nacken, Oliver Martin, Andreas Meier, Milan Schirowski, Gonzalo Abellán-Sáez and his wife Edurne Nuin-Pla, Patrick Feicht and Philipp Rietsch. They all taught me many useful things and gave me a lot of advice und many good times in our laboratories.

Furthermore, I want to mention my brother Michael and my kind colleague Ben Weintrub for correcting my grammar and typos in this manuscript. Without going into details, I could do all my kind gratitude to my friends, above all Stephan Vitzethum, Andreas Burghart, Caja Sommerfeld, Sebastian Ixmeier, Lucia Merkel, Sonakshi Arora und Andreas Lauk. With those friends you always won in life …

Statement of the Author

I declare on the affidavit that I have written the dissertation independently and have used no sources other than those I have indicated and that there are no facts which make me unworthy of the conduct of a doctoral degree under the provisions of the law governing academic degrees. Further I declare my consent that the electronic version of my dissertation, while maintaining my copyrights and data protection, may be subjected to a separate review regarding the independent preparation of the dissertation. I have not submitted the dissertation anywhere else to obtain an academic degree and have not already passed this or a similar doctoral exam without success.

Berlin, 28.09.2018

_____

Christian Eberhard Halbig